PSF Characterisation and Optimisation of a CCD for the ESA Euclid Mission

Thesis

The Open University

Doctoral Thesis

PSF Characterisation and Optimisation of a CCD for the ESA Euclid Mission

Author:
Edgar Allanwood
MEng (hons)

Supervisors:
Prof. Andrew Holland
Dr. Neil Murray
Dr. Matthew Soman
Dr. David Hall

A thesis submitted in fulfilment of the requirements for the degree of Doctor of Philosophy

in the

Centre for Electronic Imaging
School of Physical Sciences

September 2017

THE OPEN UNIVERSITY

Abstract

Faculty of Science Technology Engineering and Maths
School of Physical Sciences

Doctor of Philosophy

PSF Characterisation and Optimisation of a CCD for the ESA Euclid Mission

by Edgar Allanwood
MEng (hons)

As part of qualifying the Teledyne-e2v CCD273 for the visible imager (VIS) on the ESA Euclid mision, a front-illuminated CCD273 is tested in order to observe the Point Spread Function (PSF) response with respect to signal and voltage parameters. In order to achieve this an optical characterisation system with the ability to project flat-fields and precisely positioned and focused spot images is constructed and characterised. The Single-Pixel Photon Transfer Curve (SP-PTC) is devised in order to provide an analytical method for characterising the system PSF and the Brigher-Fatter Effect (BFE), a systematic spot-widening with signal, is observed. A technique for confirming the mechanism of the BFE via use of separate spot and flat-field illuminations in a single frame is devised in addition to parallel image clock electrode parametrisation. Device-specific optimisations are also presented regarding bright spot response and elimination of persistence following bright illuminations or charge occupation of the dielectric interface surface states.

Acknowledgements

First of all, thanks to my original Ph.D. supervisors Neil Murray, David Hall and Andrew Holland who have been incredibly patient with me throughout the production of this work.

Thanks to my line manager and now additional Ph.D. supervisor Matthew Soman, who has been instrumental in my continued development from Ph.D. student to experienced characterisation and test engineer.

Thanks to veteran imaging industry figures such as David Burt, Paul Jerram and Doug Jordan of Teledyne-e2v, who have provided me with detailed technical advice with their heritage and wisdom throughout the years, and a free Chinese meal every December. They are inspiring to me.

There are perhaps too many people to name, but thank-you to my friends and colleagues within the Centre for Electronic Imaging and extended Department of Physics, past and present. They are: Andrew Clarke, Mohit Melwani Daswani, Jason Gow, Ben Dryer, James Tutt, Richard and Kathryn Harriss, Jonathan Keelan, James Mortimer, Erika Kaufmann, Calum MacCormick, Pete Landsberg, Phillipa Smith, Adriano Ferruci, Nathan Bush, Daniel Weatherill, Joe Rushton, Daniel-Dee Lofthouse-Smith, Andy Davies, Matthew Lewis, Alice Dunford, Dan Wood, James Ivory, Anton Lindley-Decaire, Anthony Evagora, Ross Burgon, Konstantin Stefanov, James O'Farrell, Thomas Buggey, Karen Guyler and Jesper Skottfelt.

Thanks to the members of the DPS House Band, particularly Dan Dawson who got me involved.

Thank-you to my parents, grandparents and sister who have been there for me my entire life and brought me up to be within a shot of an engineering degree.

Finally, thanks to Emma for her love, unwavering support and convincing belief in me when things got tough.

*

I would like to gratefully acknowledge the financial support received from the Science Technology Facilities Council and Teledyne-e2v during my studentship.

Contents

List of Figures

List of Tables

Abbreviations

ADU	Analogue Digital Unit
AR	Aspect Ratio
CCD	Charge-Coupled Device
CDS	Correlated Double Sampling
CTE	Charge Transfer Efficiency
CTI	Charge Transfer Inefficiency
CVF	Charge to Voltage Factor
DSP	Digital Signal Processing
ESA	European Space Agency
ESF	Edge-Spread Function
FF-PTC	Flat-Field Photon Transfer Curve
FWC	Full-Well Capacity
ICD	Interface Control Document
LED	Light-Emitting Diode
NaN	Not a Number
ND	Neutral Density
NIMO	Non-Inverted Mode Operation
NIR	Near Infra-Red
NISP	Near Infra-Red Spectrometer-Photometer
PRT	Platinum Resistance Thermometer
PSF	Point-Spread Function
PTC	Photon Transfer Curve
QE	Quantum Efficiency
SGL	Strong Gravitational Lensing
SMA	Sub-Miniature version A (50Ω Coaxial connector)

SP-PTC	Single-Pixel Photon Transfer Curve
TTL	Transistor-Transistor Logic
UPS	Uninterruptible Power Supply
UV	Ultraviolet
VIS	VISible Imager
V-PTC	Variance Photon Transfer Curve
WGL	Weak Gravitational Lensing
XCU	XCAM Camera Utility

For Panda and Pinniped.

Chapter 1

Introduction: The Euclid VIS Instrument

1.1 Universal Expansion

1.1.1 Cosmic Scaffolding

In 1998 two teams of astronomers from separate institutions were approaching the same conclusion concurrently: using Type-Ia supernovae as standard candles [1] it was concluded that the rate of expansion of the Universe is accelerating. This behaviour questioned quantum theory as we know it, specifically the nature of empty space and the effect of dark matter which cannot be directly observed using traditional astronomical methods. The "cosmic scaffolding" [2] of the Universe is currently of great interest to the scientific community and it will be measured indirectly using gravitational lensing surveys in order to further investigate the causes of universal acceleration.

1.1.2 Gravitational Lensing

Gravitational lensing is a distortion in space-time in which the path of light travelling through space is curved as it passes an area of gravitational influence. The process is often separated into two categories: Strong Gravitational Lensing (SGL) and Weak Gravitational Lensing (WGL). With SGL there is a conspicuous distortion of the field of view detectable by telescopes of comparably low spatial resolution. Figure 1.1 shows an example of SGL as a double Einstein ring - a galaxy strongly lensed by another galaxy twice in a row. For this rare phenomenon to be observed both gravitational lenses have to exist along the observational axis.

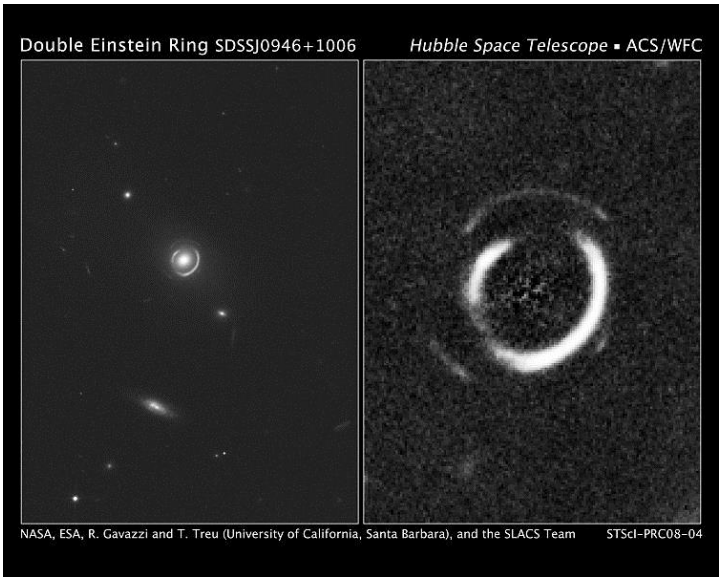

FIGURE 1.1: The Double Einstein Ring SDSSJ0946+1006 observed by the Hubble Space Telescope (Image courtesy of NASA)

WGL obeys the same concept as strong lensing however it is subtle and imperceptible without image processing. In this case galaxies peripheral to a gravitational influence appear normal whilst remaining subject to a reduced lensing effect. The lensing amount can be quantified using measures of ellipticity. Captured galaxy images are convolved with a statistical model of an isotropically formed galaxy in order to attempt to observe

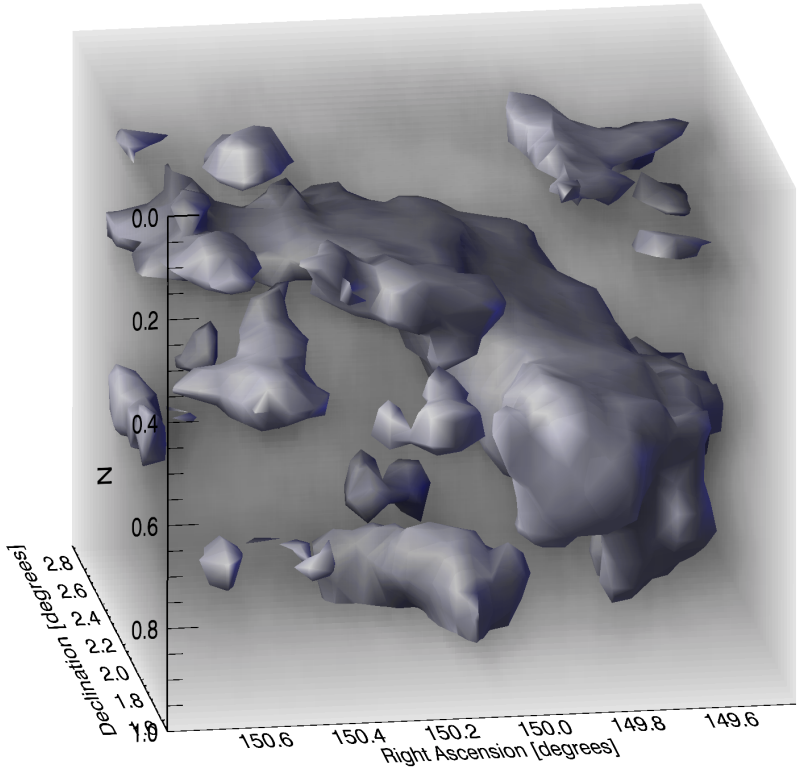

FIGURE 1.2: A 3D image of dark matter distribution (Image courtesy of Richard Massey/Nature)

the effect of weak lensing distortions over a field of galaxies. Massey [3] states the observable shear (stretching) field is proportional to a second derivative of the gravitational potential projected along a line of sight (2010). By processing averaged lensing measurements a 3D map of gravitational influence can be constructed from shear measurements as suggested by Figure 1.2 [2]. Note the Figure is shown on Cartesian axes while in reality the 3D shape would appear as a cone bounded by the angles of the telescopic field of view with a height (z-depth) representative of red shift. In the case of Figure 1.2, red shift is denoted by the vertical axis.

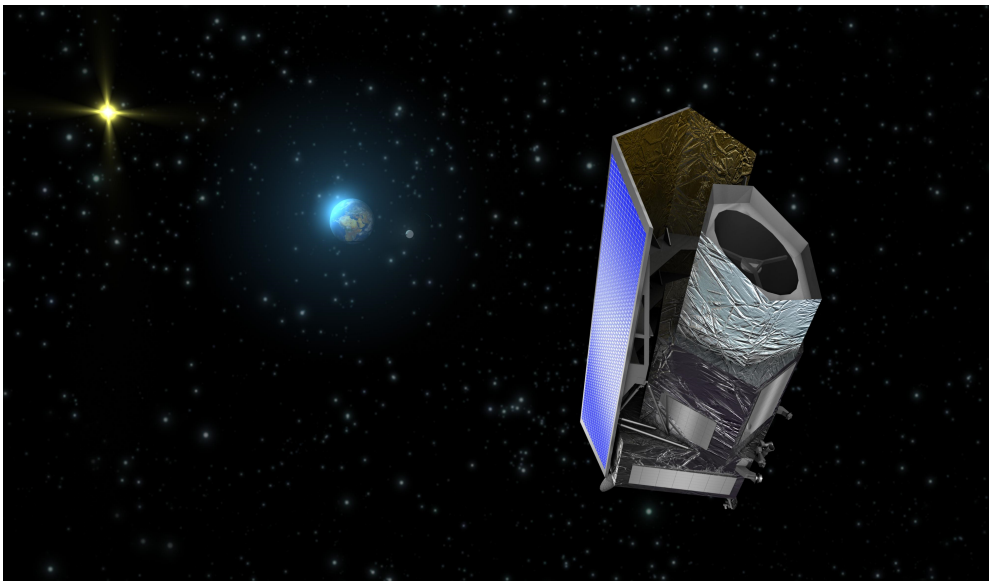

FIGURE 1.3: An artist's impression of the Euclid spacecraft (Image courtesy of ESA)

1.2 The Euclid Mission

1.2.1 Mission Synopsis

In 2012 as part of their Cosmic Vision Programme, the European Space Agency (ESA) selected Euclid as their next M-class mission with the purpose of mapping the dark Universe. Scheduled for launch in 2020 and equipped with the VISible Instrument (VIS) for optical imaging and the Near-Infrared Spectrometer Photometer (NISP) for red shift measurements, Euclid will survey 20,000 $\deg^2$ of the extragalactic sky, measuring the shapes and spectra of 2 billion galaxies in the process [4]. Using a Korsch telescope over a nominal six years, Euclid will undertake a WGL survey, indirectly observing the clusters of dark matter as a function of red shift in order to fulfil the primary science theme of updating the way the Universe is described by General Relativity.

1.2.2 Euclid VIS

VIS will observe galaxies in the 550-900 nm passband, with a shutter mechanism available for readout and dark calibration. The camera also features a flat-field illumination unit for in-flight detector calibration. VIS will consist of an array of thirty-six 4×4 kpixel Charge-Coupled Devices (CCDs) [5], representing a 576 Mpixel image, which is compressed by the data processing unit for transfer to ground [6]. The CCD273 is manufactured by Teledyne-e2V in Chelmsford, England. Section 3.3.1 details the detector specifics.

1.2.3 PSF Requirements

Cropper et. al. [7] outline the systematic challenges when approaching a weak lensing survey in the paper "Defining a Weak Lensing Experiment for Space" (2013). From a detector viewpoint, the entire signal chain relies on a very accurately realised system Point-Spread Function (PSF). A PSF describes the spatial input response, or in layman's terms: the blurring of an imaged object [8]. If the PSF is known, then the blurring of the captured images can be reversed by deconvolution, and the galaxy shapes fed into the weak lensing processing chain.

1.3 Research Goals

The shape-oriented characterisation of a CCD for the Euclid VIS instrument forms the basis of this study, which takes an optical approach to characterising CCDs. The relative performance of Point Spread Function (PSF) and inferred effect on weak lensing measurements will be measured experimentally. The appearance of galaxies will be

emulated by an optical projection system, the systematic construction and evaluation of which is summarised in the following chapters, with research goals as follows:

1. Construct an optical test facility for the projection of galaxy-like objects
2. Characterise the optical test facility
3. Characterise the response of the CCD273 to galaxy-like objects
4. Perform laboratory optimisation of the CCD273 operating parameters

1.4 Thesis Organisation

This study is organised into eight chapters, the contents of which are as follows.

1. Chapter 1 contextualises the study and provides background on the Euclid mission and relevant research goals.
2. Chapter 2 provides a theoretical background study of the inception, construction and operation of CCDs, adapted for a four-phase device such as the Teledyne-e2v CCD273.
3. Chapter 3 details the non-optomechanical laboratory instrumentation, including the Teledyne-e2v CCD273 itself and the photon transfer characterisation of the system.
4. Chapter 4 documents the optomechanical design of the optical system used to characterise the Teledyne-e2v CCD273, including system interfaces, spot and flat-field projection assemblies, repeatability validation, focusing and positioning algorithms, spot PSF measurement techniques and light-tight isolation verification.

5. Chapter 5 introduces a new Photon Transfer Curve (PTC) technique adapted for spot image analysis: the Single-Pixel PTC (SP-PTC). In this chapter, spot images are captured from low signal to pixel full-well capacity and the effects are observed. A significant portion of the chapter is dedicated to the detection of systematic error which undermines shot noise limited characterisation, and novel mitigation techniques used in order to eliminate error and infer the signal-dependent behaviour of the system PSF.

6. Chapter 6 acknowledges the existence of the Brighter-Fatter Effect (BFE) and devises a new experimental technique for estimating to what level the Teledyne-e2v CCD273 is affected. The effects of CCD biasing parameters on the BFE are also investigated.

7. Chapter 7 parameterises the image clock, substrate and output amplifier drain voltages in order to optimise the full-well capacity and linearity performance of the Teledyne-e2v CCD273. The four image-area image clock phases are individually characterised with respect to their signal-dependent spot image response and the data is related to physical microscope images of the device. Additionally, a method for linearising experimental data is documented.

8. Chapter 8 summarises the thesis content, contextualising the presented data with the Euclid mission and arriving at the conclusion. Based on the thesis work, the development of a more advanced optical characterisation system for the JUpiter ICy moon Explorer (JUICE) visible imager is discussed.

1.5 Associated Publications

E. A. H. Allanwood, N. J. Murray, K. D. Stefanov, D. J. Burt, and A. D. Holland. *"Point-spread function and photon transfer of a ccd for space-based astronomy."* SPIE Optical Engineering and Applications, International Society for Optics and Photonics, 2013.

N. J. Murray, **E. A. H. Allanwood**, B. J. Dryer, D. P. Weatherill, K. D. Stefanov, A. D. Holland, and D. J. Burt. *"Comparison of point spread function in p-and n-channel CCDs."* Journal of Instrumentation, 10(08):C08007, 2015.

N. J. Murray, D. J. Burt, A. D. Holland, K. D. Stefanov, J. P. D. Gow, C. MacCormick, B. J. Dryer, and **E. A. H. Allanwood**. *"Multi-level parallel clocking of ccds for: improving charge transfer efficiency, clearing persistence, clocked anti-blooming, and generating low-noise backgrounds for pumping."* SPIE Optical Engineering and Applications, International Society for Optics and Photonics, 2013.

Chapter 2

Charge-Coupled Devices

2.1 Introduction

As a basis for the experimental work presented, the theory and operation of the CCD is first considered.

2.1.1 Inception

The Charge-Coupled Device (CCD) was realised as a side-product of computer memory development at Bell Telephone Laboratories in 1969 [9]. Delay line memory is the concept in which data is serially recirculated around a loop with a recall and amplification stage between each cycle. Eckert [10] likens the process to "The short-range human device of repeating a phone number to oneself from the time it is located in the phone book until it has been dialed." (1998). The CCD was initially designed to hold bits in a similar fashion, analogous to the operation of a logical shift register. The first device was manufactured to hold one byte and it was during characterisation that the potential for electronic imaging was first noted [11, 12]. Within a decade the technology matured

to the level at which it became applicable not just for regular photography but also astronomical imaging.

This section discusses the design and characteristics of CCDs from first principles as a basis for discussion in relation to shape-based astronomical measurements in later chapters.

2.2 Silicon as a Semiconductor

2.2.1 The Band Gap

Prior to discussing the logistics of charge generation, storage and transfer in CCDs it is necessary to understand the nuances of intrinsic silicon and its extrinsic doped variants. The conductivity of a material is proportional to the concentration of delocalised electrons and partially filled states, of which there are few in intrinsic silicon. In order for an electron to become promoted from the valence band to the conduction band it requires additional energy to cross the band gap, which may be provided in part by an incoming photon. Silicon is intrinsically an insulator, bonding with itself to form a crystal lattice. Dopant atoms may be introduced to Silicon in order to change the nature of the material by creating an abundance of free electrons or holes depending on whether the material is negatively or positively doped.

Figure 2.1 illustrates the electronic orbital configuration for silicon, phosphorus (a negative dopant) and boron (a positive dopant). The outer shell of phosphorus has five electrons and three vacancies, therefore when bonding with silicon there is one free electron, which can cross the band gap at much lower energy. Conversely, the outer shell

of Boron has three electrons with five vacancies resulting in an extra vacancy or "hole" when bonding with silicon.

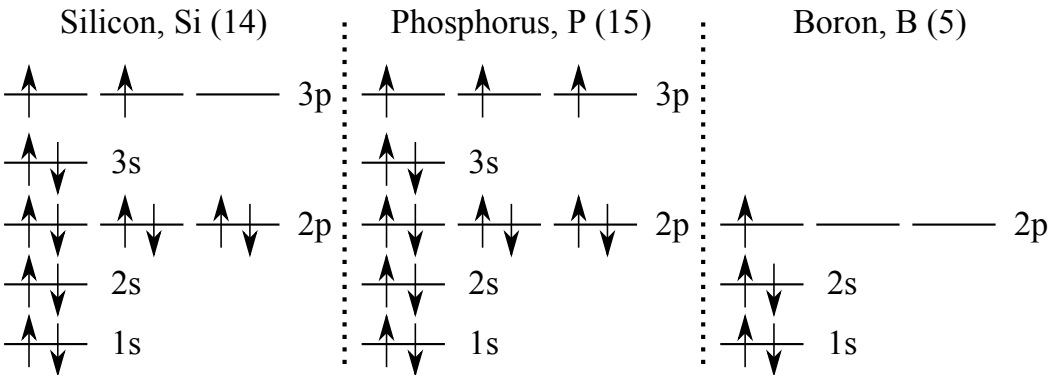

FIGURE 2.1: Diagram illustrating the electron orbital shell configuration of intrinsic silicon and two popular negative and positive dopant atoms.

2.2.2 The Depletion Region

Connecting together regions of n-type and p-type silicon forms a volume surrounding the interface known as the depletion region. It is here that the free electrons from the n-type region meet the holes from the p-type region, combining to deplete the interface of any charge carriers. Including such a structure in an electronic circuit has useful properties as demonstrated in Figure 2.2 where current is only allowed to flow in one direction. Consider the reverse bias configuration: the free electrons in the n-type material are attracted to the battery anode whilst the p-type holes are filled by electrons originating from the cathode, resulting in a widening of the depletion region and practically no current flow. Reversing the battery such that electrons travel into the n-type material and flow away from the p-type material (creating more holes) creates a situation where the depletion region disappears and current is allowed to pass. This is the concept behind the diode and led to the inception of similar devices such as the bipolar junction and field effect transistors.

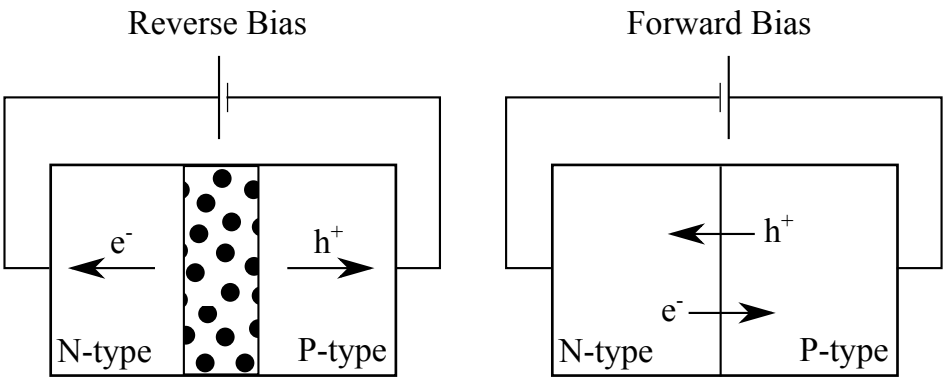

FIGURE 2.2: A p-n junction shown in forward and reverse bias to demonstrate the effect on the depletion region.

Figure 2.3 relates the band gap to the Fermi level, E_F for intrinsic, n-doped and p-doped silicon. An electron may "jump" from the valence band to the conduction band if excited thermally, or by an incoming photon.

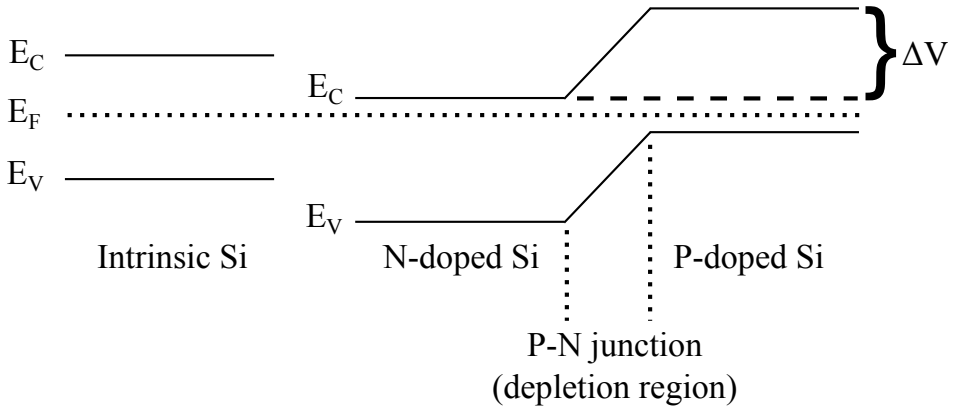

FIGURE 2.3: Band diagram showing the conduction E_C and valence bands E_V relative to the Fermi level in intrinsic and extrinsic silicon.

2.2.3 The MOS Capacitor

A structure very similar in nature to a CCD pixel is a Metal-Oxide-Semiconductor (MOS) Capacitor. A metal electrode is capacitively coupled to a p-type substrate through an insulating layer referred to as the gate dielectric. As an electric field is exerted by a voltage applied to the metal (or often, polysilicon) gate, the effect is felt on the other side of the dielectric for some distance into the silicon. Figure 2.4 illustrates

the capacitor analogy and demonstrates cases where the gate voltage, V_{Gate} is varied with respect to the flat-band voltage $V_{Flat-band}$. The flat-band voltage is due to an in-built positive charge at the Si-SiO_2 or "surface", caused by "dangling bonds" [13], the nature of which, including channel potential profiles are further discussed in Section 2.3.2. As V_{Gate} exceeds $v_{Flat-band}$, electrons are drawn to the surface while holes are drawn towards the substrate. If the conditions are reversed, holes are drawn to the surface and electrons to the substrate. These are the basic principles of depletion, e.g. electron storage under electrodes, and accumulation. Accumulation mode is studied in this thesis in Section 7.3 at the substrate is made positive with respect to the gate in order to flood electron charge traps as the Si-SiO_2 interface with holes.

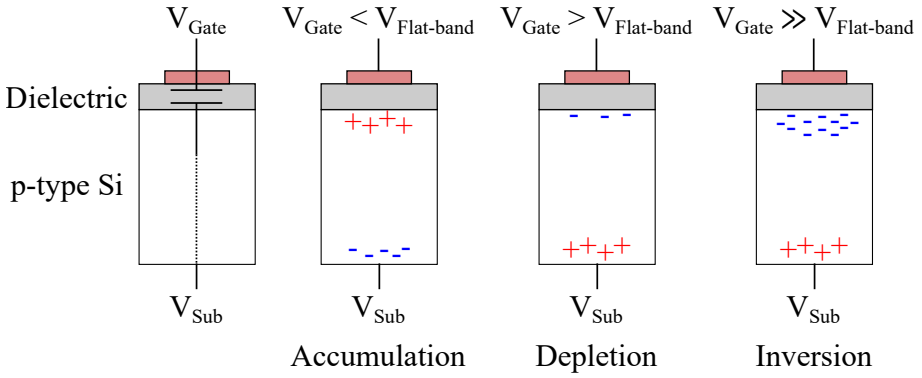

FIGURE 2.4: Diagram illustrating the MOS capacitor structure and movement of carriers, with respect to biasing conditions.

This work features an n-channel CCD273, where "n-channel" denotes that the majority carrier of current flow is electrons, while in a p-channel device the majority carrier would be the absence of electrons which are called "holes". The CCD273 is a depletion-mode device which has been previously been characterised by Gow. et. al. [14] with respect to radiation-damage based flat-band voltage shift - a consequential change in electric field influence and thus charge storage performance.

2.2.4 The MOSFET

In a CCD the measurement of charge requires amplification, and the Metal Oxide Semiconductor Field-Effect Transistor (MOSFET) is used for this purpose. Section 2.3.4 details the process in which charge is used to potentiate the current flow of a MOSFET, combined with a load resistor in a common-drain configuration. The process by which current flow is influenced by electric field effect will be summarised here.

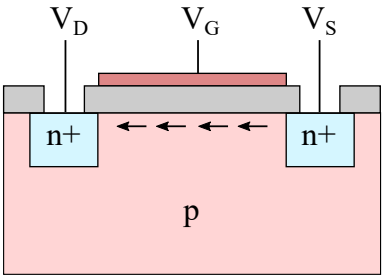

FIGURE 2.5: Diagram illustrating the structure of an n-channel MOSFET, with the path of electrons, opposing the direction of electrical current flow, from source to drain.

Figure 2.5 illustrates the typical construction of an n-channel MOSFET. Like the MOS capacitor of Section 2.2.3, the MOSFET features a polysilicon electrode, insulated from a p-substrate with a gate dielectric. In two places the dielectric is etched away, with contacts made from two n-doped regions, resulting in two p-n junctions. When a positive potential difference is applied between Gate, V_G and Source, V_S, an electric field is exerted on the channel, depleting the surface of holes. When V_{GS} exceeds V_{Th}, the threshold voltage is said to be the point at which a channel of electrons becomes established, and beyond depletion: inversion (as in Figure 2.4). The drain current is parameterised by the gate voltage, geometry, electron mobility, gate oxide capacitance and threshold voltage. In this work the drain voltage of the CCD output source follower is characterised in terms of linearity, which is explained in Section 7.5.

2.3 CCD Structure and Operation

2.3.1 The CCD Pixel Array

A CCD consists of a two dimensional array of elements known as pixels. Figure 2.6 illustrates a simplified single pixel juxtaposed against a much larger two-dimensional array. An n-type buried channel is sandwiched between a gate dielectric and p-type substrate with poly-silicon electrodes manipulating the electric field from above. In the example shown a voltage is applied to the two innermost electrodes causing a depletion region to form in the pixel centre while the surrounding inactive electrodes act as a barrier. Combined with the effect of p-type channel stops, this configuration confines any generated electrons to a region referred to as the potential well. A standard CCD model consists of a three electrode pixel architecture, however; a four electrode model relevant to the Euclid VIS CCD273 studied is presented here.

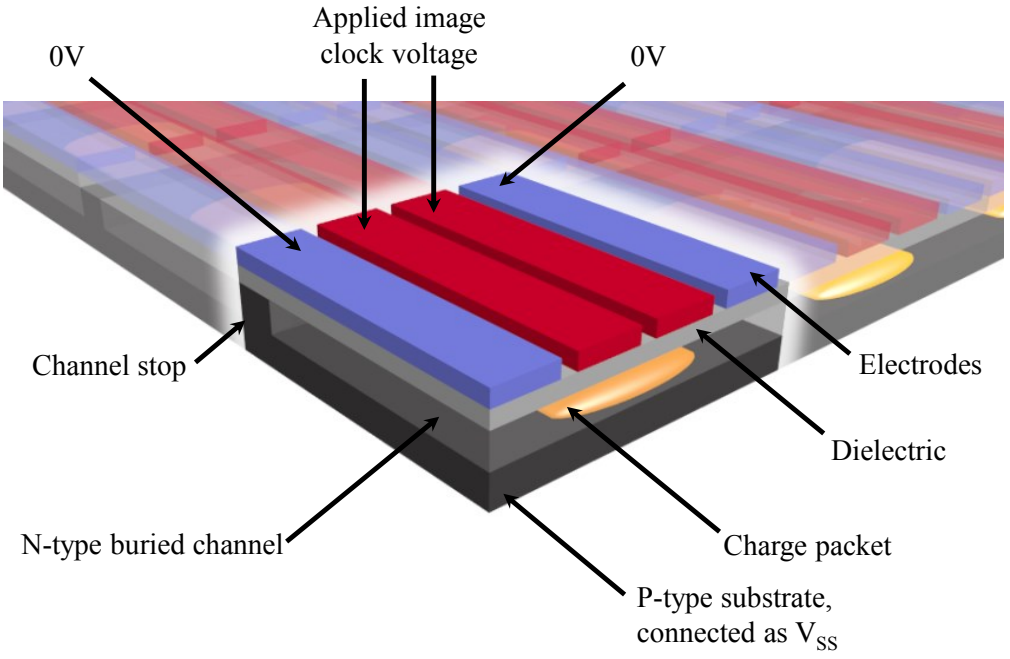

FIGURE 2.6: The structure of a pixel in a four-phase device.

2.3.2 Charge Collection

Charge collection behaviour is an important aspect of this study and in order to present the theory in a way which is relevant to the device under test, Figure 2.7 illustrates the cross section of a front-illuminated pixel, with the potential profile alongside. The diagram is a cross-section representing a slice from the top surface of the CCD (left) to the substrate (right). In the diagram, example potential profiles are shown for a positive bias applied to the electrodes of a buried channel device (blue) and a surface channel device (green). The CCD273 is a buried channel device, hence photo-generated electrons are held in a potential well, away from the *"surface"* or Si-SiO_2 interface. The green surface channel profile illustrates the potential profile of an example surface channel device without a buried n-channel. In the surface channel profile, the highest potential would be V_{Img}, which has the unfortunate side effect of drawing electrons towards the dangling bonds of the Si-SiO_2 interface.

The dangling bond analogy refers to unpassivated vacancies in between the silicon dioxide dielectric and silicon channel which "dangle", trapping passing electrons and releasing them in later charge packets, contributing to considerable Charge Transfer Inefficiency (CTI). Surface state interaction and mitigation is discussed experimentally in relation to image clock electrode biases in Section 7.2.3.

The term "front-illuminated" refers to a device which receives illumination through the top electrodes, with incoming photons being subject to reflection, scattering and absorption by the electrode structure. The term "back-illuminated" refers to a device which is illuminated from the substrate side. An important consideration with charge collection in CCDs is the interaction depth, which is dependent on wavelength of incident photons. Devices are often back-thinned on the substrate side and turned upside down

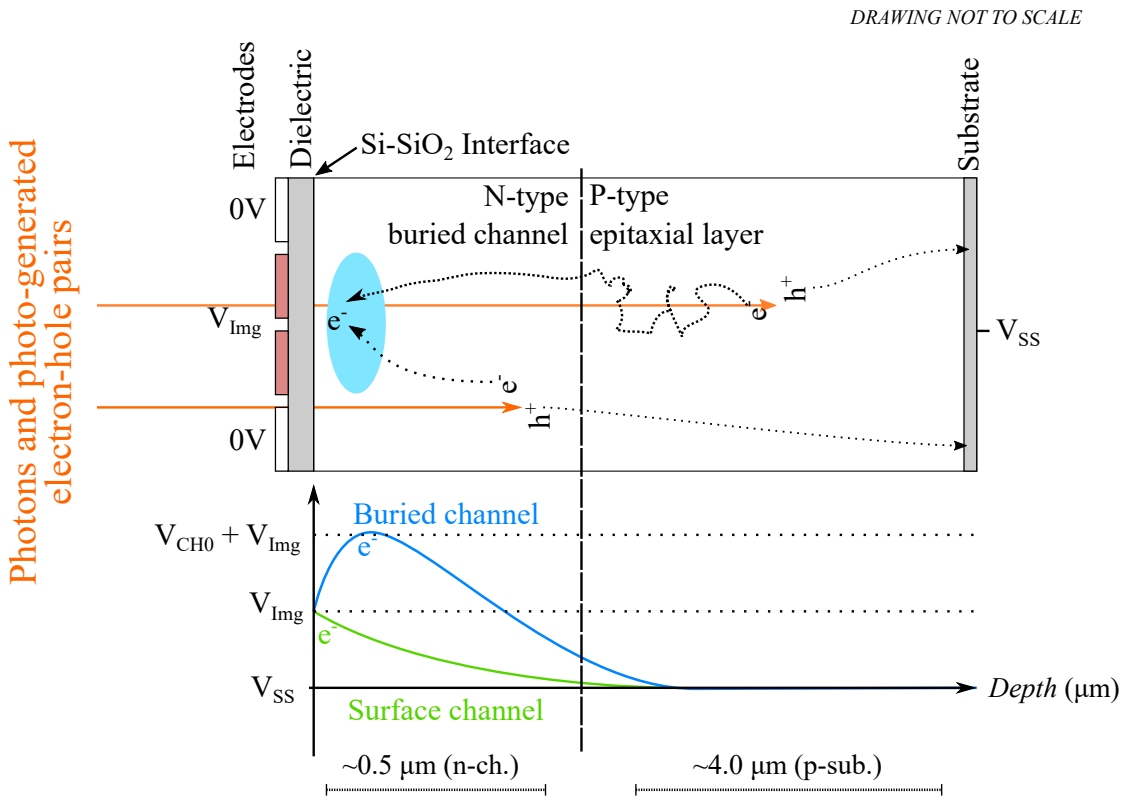

FIGURE 2.7: Charge collection diagram illustrating the approximate pixel structure above and potential profile below.

and back-illuminated, to allow for improved spectral response or *Quantum Efficiency* (QE) at shorter wavelengths. In the context of this work red wavelength illuminations are used with a front-illuminated CCD, the specifications of which are detailed in Chapter 3. For the flight device, a back-illuminated sensor will be used and the wavelength-dependent charge collection behaviour will be different to that seen in this thesis. For instance, red photons are expected to interact closer to the influence of, or inside the buried channel in a back-illuminated sensor which is appropriate for a mission surveying red-shifted galaxies.

With the two electron-hole pairs of Figure 2.7, one is shown to have been generated in the field-free region and this is associated with the possibility of lateral diffusion between pixels. The spatial response of a detector is wavelength dependent due to diffusion of electrons which are generated far away from the influence of the electric field. In

the scope of this work, the front-illuminated CCD273 which has a different collection behaviour to the flight-grade back-illuminated CCD273 is used for experimentation. Therefore the red light used for characterisation here will have different lateral diffusion characteristics to the flight device.

2.3.3 Charge Transfer

Figure 2.9 shows the pixel in the context of a fictitious 5×5 pixel device. For each row four electrodes referred to as image phases $[I\Phi1, I\Phi2, I\Phi3, I\Phi4]$ span all columns, repeating in the direction of parallel transfer toward the serial register. During readout the image phases are driven by periodic voltage waveforms which encourage transport of charge packets by sequentially alternating which phases are depleted and which are barriers. This process is known as "clocking" - a phrase inherited from original device purpose as a digital shift register. Figure 2.8 illustrates the charge transfer process for a one row parallel transfer of the CCD273.

Two acronyms are used when discussing CCD charge transfer performance: the Charge Transfer Efficiency (CTE) of a CCD is a scalar value representing the percentage of electrons transferred during a single transfer between pixels. The Charge Transfer Inefficiency (CTI) is the complement of CTE, representing the percentage of electrons *not* transferred during a single transfer between pixels. In devices without a buried channel [15, 16] electrons are more frequently subject to interaction with "surface" states, previously described as "dangling bonds". Charge trapped in surface states may be released into other charge packets during clocking, causing a streaking effect in the image. Furthermore, radiation damage during space flight can cause a multitude of traps in the silicon lattice, known as bulk defects. The longer a CCD is in space the more traps charge form from radiation damage, and the more susceptible the CCD is to CTI.

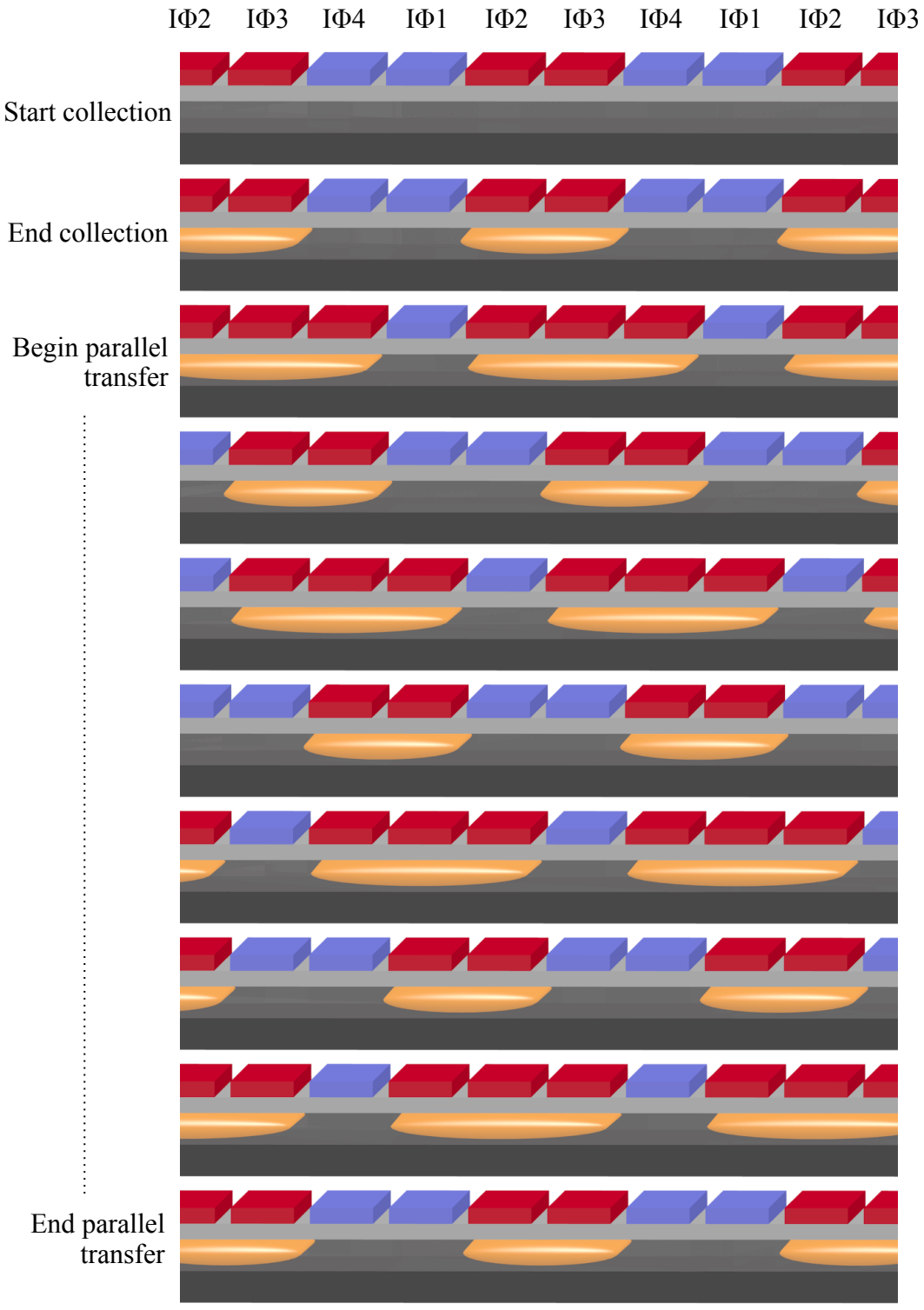

FIGURE 2.8: A sideways view of the parallel register (a single column) during integration time and readout using a 2-3-2 clocking scheme.

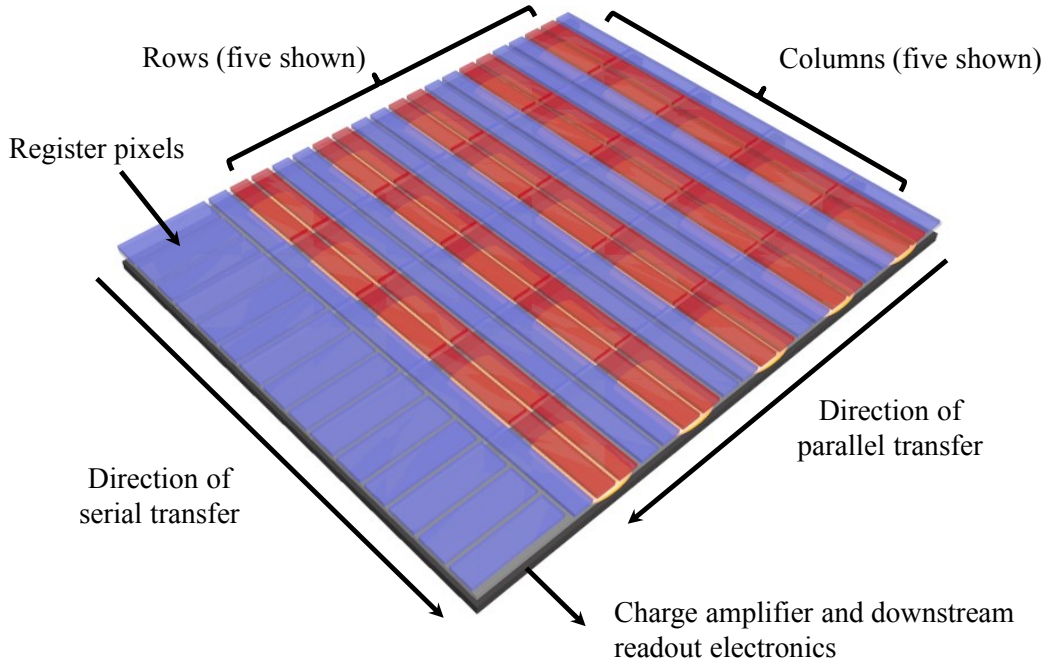

FIGURE 2.9: A simplified 5×5 pixel CCD demonstrating directions of charge transfer in parallel and serial registers.

2.3.4 Measuring Charge

For each transfer of the serial register, charge passes through a charge amplifier circuit, which serves to convert charge into a value in microvolts. The number of microvolts per measured electron is often referred to as the Charge to Voltage Factor (CVF). A simplified schematic is presented alongside the terminus of the serial register in Figure 2.10. The sense node is a small volume by which to measure charge and it represents a capacitance C_{SN}. The source-follower is a high-impedance input amplifier of gain less than unity, which mitigates the loading effect on the sense node by any downstream amplification or measurement circuitry. The source follower consists of a MOSFET as described in Section 2.2.4. Prior to serial charge transfer, the sense node is reset to a specified voltage level, set by the reset drain voltage, V_{RD}. This reset level is presented and sampled at the output, as the first step of a two-stage Correlated Double Sampling (CDS) process. The output gate is then turned on and the last serial register

phase (in this case, V_{Serial} is turned off, and the charge falls into the sense node. The transferred electrons "pull down" the voltage set by V_{RD} and after settling the signal level is presented and sampled at the output. The process then repeats for every pixel in the serial register, for each parallel transfer until the device is sampled completely.

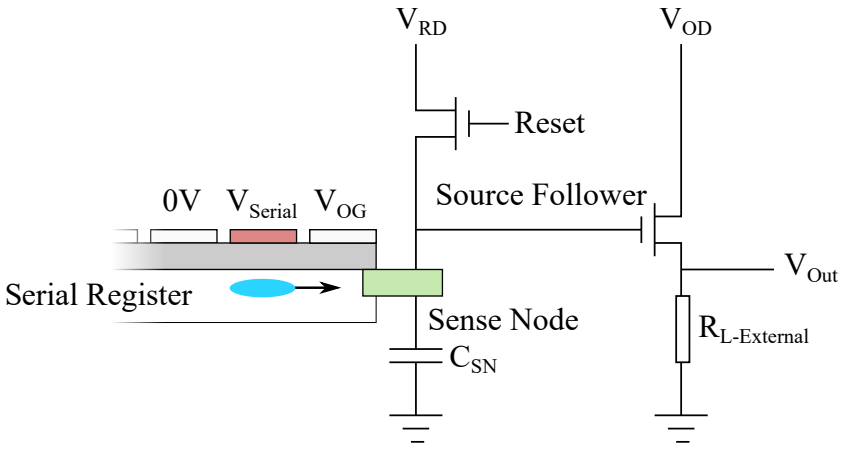

FIGURE 2.10: A simplified schematic of the signal path from the end of the serial register to device output.

Figure 2.11 illustrates the CDS electronics found downstream from the CCD source follower. The headboard preamp boosts the output such that signal to noise ratio between the CCD output and camera electronics is improved. Following this the signal is split between two sample and hold circuits. The purpose of the sample and hold circuitry is to eliminate reset noise, which is caused by variations in sense node reset levels between pixel samples. Following a sense node reset in the CCD output electronics, the offset level (i.e. the voltage at which there are no converted photo-generated electrons present) is presented to V_{In}. It is during this period that ϕ_{SHR} is pulsed and the amplified reset level is stored in C_{Reset}. A serial transfer then moves charge into the sense node and the electrons "pull down" the voltage seen at the output of the source follower. This signal is then sampled by pulsing ϕ_{SHS} and stored in C_{Signal}. With the reset and signal levels sampled and held, the differential amplifier subtracts the reset level from the signal level,

presenting a voltage to the Analogue to Digital Converter (ADC) which in turn, reports the nearest digital number or Analogue Digital Unit (ADU) to the camera software.

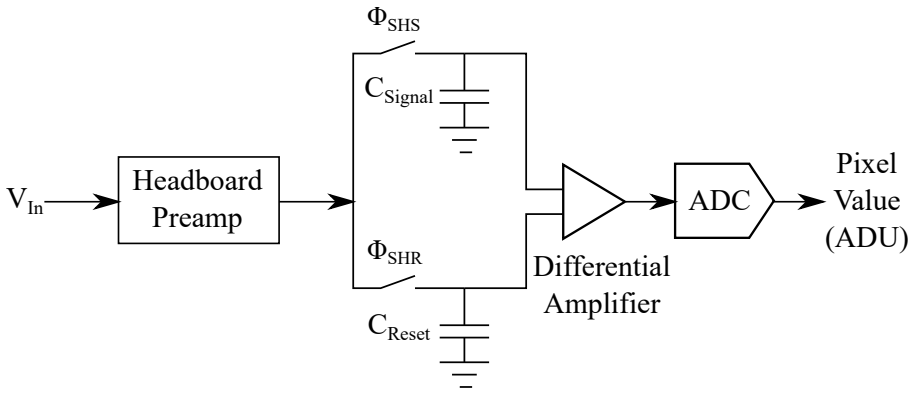

FIGURE 2.11: A simplified Correlated Double Sampling (CDS) electronics circuit.

2.4 Summary

This chapter introduces key concepts of CCD operation from a solid state physics background, with reference to specific areas of interest including the CCD273 four-phase parallel electrode architecture, charge collection, charge transfer process and output amplifier biasing variables. The detector design and camera electronics used for biasing, clocking and analogue to digital conversion are detailed in the next chapter.

Chapter 3

Laboratory Instrumentation

3.1 Introduction

The Centre for Electronic Imaging [17] has a history of characterising imaging detectors for space technology readiness. The experimental configuration usually involves a cryogenic cooling system, coupled to the detector in order to replicate the mission operating temperature in the laboratory. An example of this is given by Gow [18] in which the experimental arrangement for the CTI measurements in the CCD204 and CCD273 is detailed (2012). The mission operating temperature for the CCD is usually below freezing due to the need to suppress thermally generated dark current in the image area over astronomical integration times. At room temperature, a CCD left to integrate charge for a long frame time analogous to that of the Euclid mission (hundreds of seconds) would suffer from dark current to such an extent that no useful signal could be observed. Euclid detectors have already been characterised by the CEI and shown to exhibit dark current of less than 1 electron per pixel per 500 seconds of operation at $-100\,^{\circ}\mathrm{C}$ (173 K) [19].

In addition to cryogenic cooling, a vacuum system must be utilised in order to evacuate air from around the device to prevent condensation of water onto electronic components. Upon establishing mission-like conditions, system calibration is conducted in order to prepare the camera for experimental testing. This chapter details the instrumentation used to run the Teledyne-e2v CCD273 and the system calibration process.

3.2 Vacuum-Cryogenic System

3.2.1 Vacuum Chamber Configuration

To emulate the $-110\,^{\circ}\mathrm{C}$ (163 K) atmospheric and operating conditions at the L2 Lagrangian point by which Euclid will be situated, and suppress thermally generated dark current, the camera head was situated in a windowed vacuum chamber as illustrated in Figure 3.1.

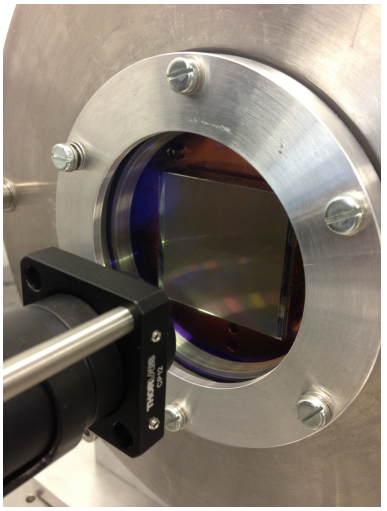

FIGURE 3.1: The CCD was mounted as close to the chamber window as possible to minimise the working distance required for the optics.).

The chamber was pumped down to 1.6×10^{-6} mbar using a Pfeiffer Vacuum Turbopump. In the absence of a vacuum, the moisture in the air would condense on the cooling camera head, likely damaging the system. For this reason an Uninterruptible Power Supply (UPS) was deployed in series with the turbopump to mitigate the risk of vacuum loss in the event of a power outage. Secondly, the detector was cooled to $-100\,^{\circ}\mathrm{C}$

(173 K) using a Brooks Polycold PCC Compact Cooler [20]. $-100\,^{\circ}\mathrm{C}$ was the best temperature that could be achieved by the setup and deemed appropriate for dark current suppression based on the work by Gow [19] (2012).

The factors influencing the lowest temperature to which the camera head could be cooled were many: Free space was limited due to a dense chamber layout and a thermally leaky window was necessary for optical projections. In an ideal system there would be a greater number of thermal interconnects between the cold finger to the rear of the chamber and the cold bench supporting the CCD. Thermal lagging material could have been positioned around the chamber walls to slow the rate at which the chamber was warmed by the surrounding laboratory, however; this would have increased the risk and precision required when inserting the camera head into the chamber. Figure (3.2) illustrates the thermal and electronic configuration of the camera head from a top-down perspective while Figure (3.1) shows the position of the CCD, within the window flange.

3.2.2 Vacuum System

A Pfeiffer Vacuum HiCube 80 turbo pumping station with an ultimate pressure of 1×10^{-7} mbar was used for maintaining a vacuum.

3.2.3 Cryogenic System

A Brooks Polycold PCC Compact Cooler [20] was utilised for cooling the copper cold bench within the vacuum chamber. The system consists of a compressor, send and return high pressure gas lines carrying PT-30 refrigerant and a cold-end which interfaces with the rear of the vacuum chamber. Copper braids are used to link the cold-end to the cold bench, as shown in Figure 3.2.

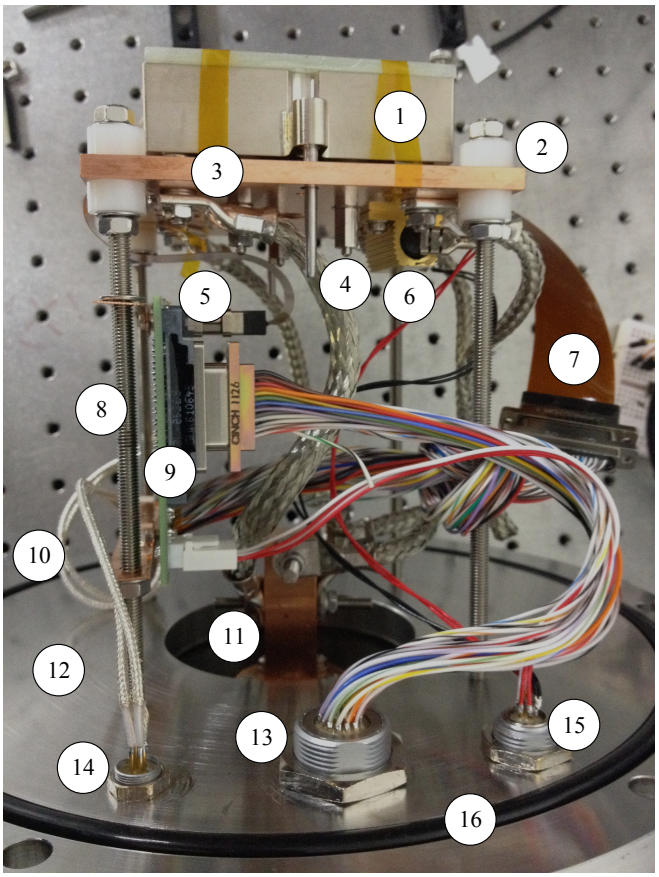

FIGURE 3.2: Top-down: the configuration of the camera head during maintenance. See Table. (3.1) for description of numbered features.

3.3 Camera System

3.3.1 The Teledyne-E2V CCD273

All experimental work was conducted using a Front-Illuminated (FI) Teledyne-E2V CCD273-84. Figure 3.3 [21] illustrates the device layout, which features two parallel-transfer arrays separated by a central Charge Injection (CI) structure. Each array is served by a single register, split down the middle to serve two output nodes. The CCD273 is a four quadrant device by design, although the headboard serial clock connections could possibly be configured such that only one output node is used for each array. This would be detrimental to serial transfer time and serial Charge Transfer

Item	Description
1	CCD transportation cover in order to reduce contamination during maintenance.
2	Plastic thermal insulation, separating the cold-bench from the supporting structure.
3	The copper cold bench is highly thermally conductive and serves as an anchor point for the CCD mounting studs. Three steel braids used for thermal coupling terminate here.
4	Mounting stud of the CCD package (one of three).
5	CCD flexible wire connection (one of two).
6	Temperature controller resistive load.
7	CCD flexible wire connection (two of two).
8	M4 threaded rod (one of four) used to mount the headboard PCB and accurately position the cold bench near the chamber window.
9	CCD headboard PCB featuring pre-amp, filter and temperature management circuits.
10	Coaxial Video cable (two of four channels).
11	Thermal connection to CryoTiger.
12	Chamber rear cover.
13	Fischer connector carrying bias voltages and clock waveforms.
14	Coaxial video cable (two of four channels).
15	Connection to resistive heating element and headboard, CCD platinum resistance thermometers (PRTs).
16	Rubber o-ring seal to assist vacuum integrity.

TABLE 3.1: List of chamber features corresponding to Figure (3.2).

Inefficiency (CTI), hence the design decision for four output nodes.

The CCD273 design is based on the CCD203, a device previously flown on the NASA Solar Dynamics Observatory. The CCD273 differs from the CCD203 in the respect that it has improvements [22] in amplifier noise, responsivity, red response and the addition of parallel charge injection structures. The CCD273 also features a narrower serial register in order to mitigate CTI, at the expense of losing parallel binning function - which will not be employed on Euclid VIS. The CCD273 design features thin gate dielectric electrodes, a process improvement developed by Teledyne-e2v in order to reduce the impact of ionising radiation, which typically causes a proportional flat-band voltage shift [23].

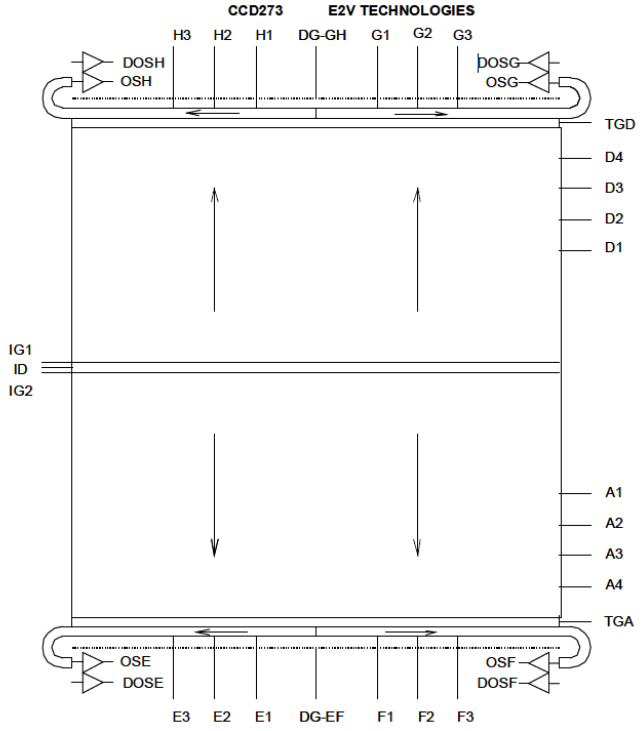

FIGURE 3.3: The CCD273 layout.

The design parameters for the CCD273 test device are listed in Table. 3.2, while the physical packaging and handling jig are shown in Figure 3.4.

Device Information - Teledyne-E2V CCD273-84	
Pixel Size	$12\mu m$ square
Array Dimensions	2066 rows × 4096 columns
Electrode Configuration	4-phase parallel, 3-phase serial
Electrode Structure	Thin-gate
Mode of Operation	Non-inverted (NIMO)
Number of Output Nodes	4 active, 4 dummy
Number of Serial Pre-scan Elements	51
Dump Gate	Yes
Illuminated Face	Front-illuminated (test device)
AR Coating	None

TABLE 3.2: The CCD273 design parameters.

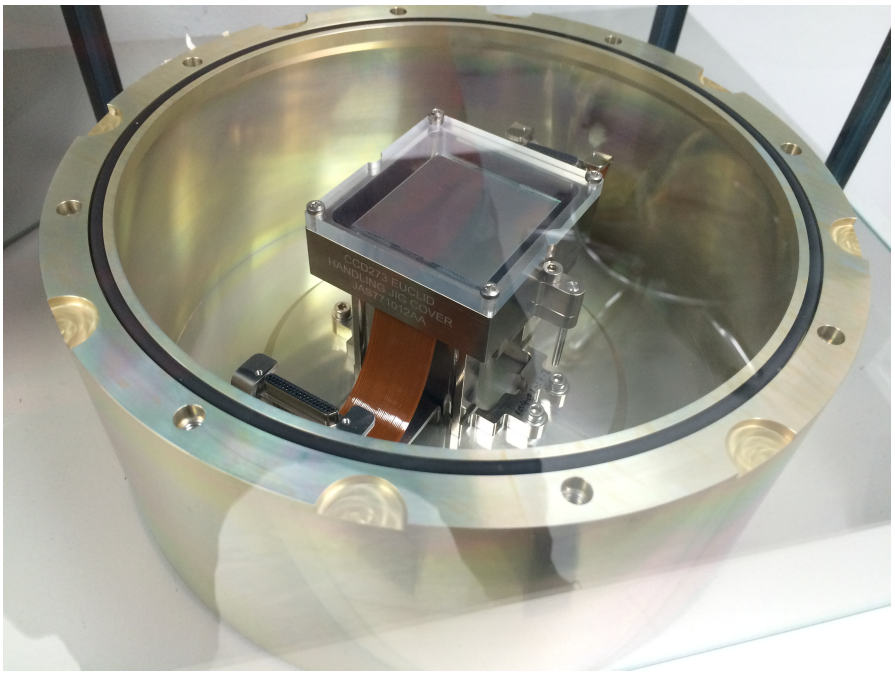

FIGURE 3.4: The CCD273 packaging and handling jig, supporting the device with adjoining flexi supports. Model shown here is the proton-irradiated and front-illuminated CCD273 with no anti-reflective (AR) coating.

3.3.2 Camera Electronics

An XCAM CCD electronics system [24] was utilised to bias, clock and read out the CCD273. A headboard PCB with pre-amps and low-pass filtering was situated inside the vacuum chamber and interfaced with by a 25-way Fischer port [25] carrying bias and clock signals. Four video channels were fed through a separate connector to coaxial cables terminated by SMA connectors. A single-channel dual-slope integrator Correlated Double Sampling (CDS) card with a 16-bit Analogue to Digital Converter (ADC) was utilised for the majority of measurements, while a four-channel variant of the same CDS was used when all four nodes were required to be read out simultaneously.

The XCAM proprietary image acquisition software was interfaced with MATLAB to enable configuration of key system variables such as clock sequencer selection, image size, image binning, bias voltages, clock waveform amplitudes and clock waveform timings.

A "sequencer" is written in assembly code and executed on a Digital Signal Processing (DSP) chip while the camera is powered. The default purpose of a sequencer is to wait for an image grab request and apply clock waveforms to the CCD and CDS circuits during integration time, readout and clear out routines, such that an analogue video signal is intercepted by the CDS and a digital image is returned to the laboratory computer via a USB host. Figure (3.5) provides a simplified overview of this process.

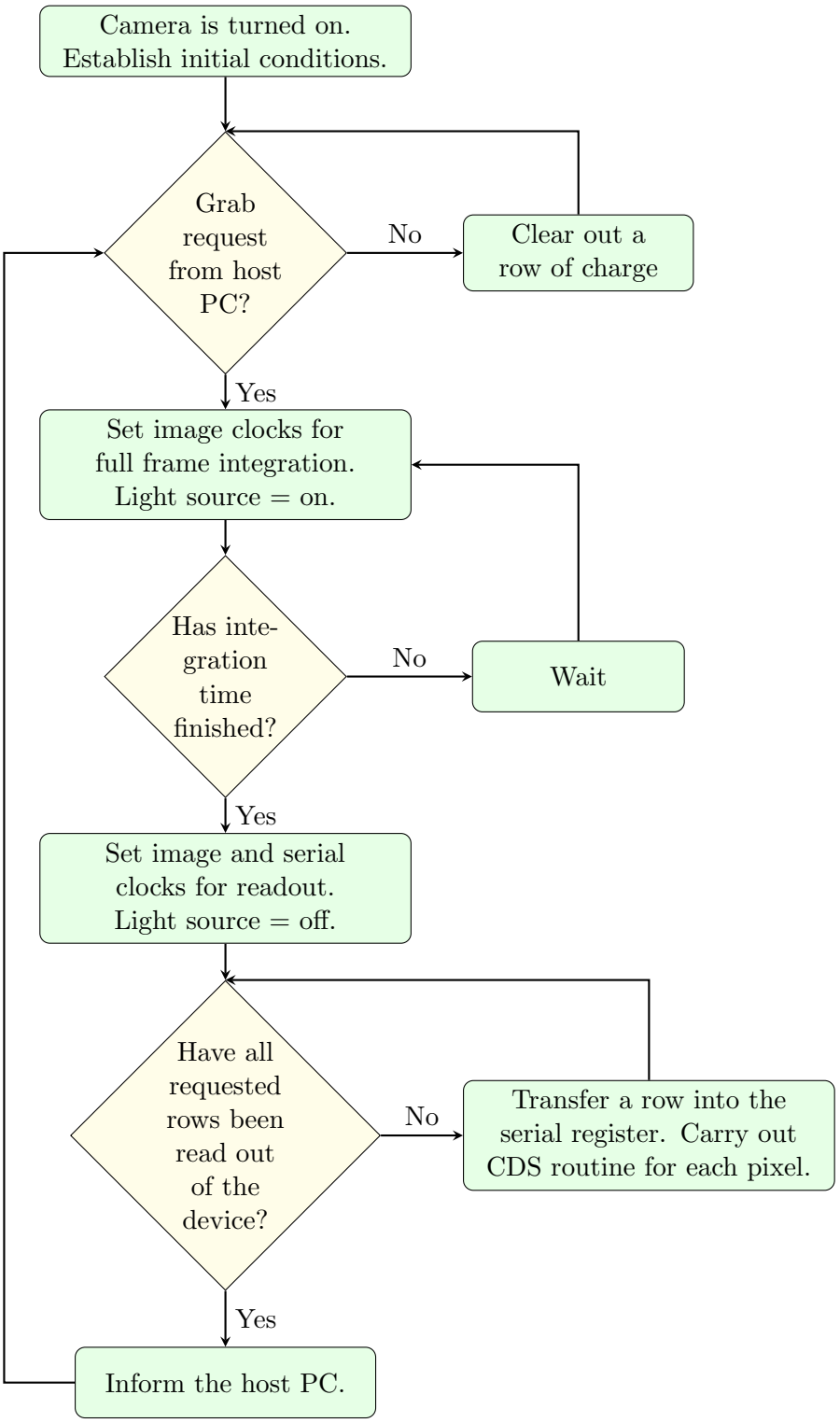

FIGURE 3.5: A simplified anatomy of a default image acquisition sequencer.

3.4 Device Calibration: The Photon Transfer Curve

3.4.1 Purpose

The Photon Transfer Curve (PTC) technique measures noise relative to mean signal in order to generate a useful characterisation of detector noise performance, while determining the overall system conversion gain, full-well capacity and linearity. A PTC considers the imaging system from photon to Analogue Digital Unit (ADU) as a black box configuration with two variables as shown in the simplified Figure 3.6. The PTC methodology will be discussed in this section, while any shortcomings due to nonlinearity will be investigated in greater detail in Chapter 7.

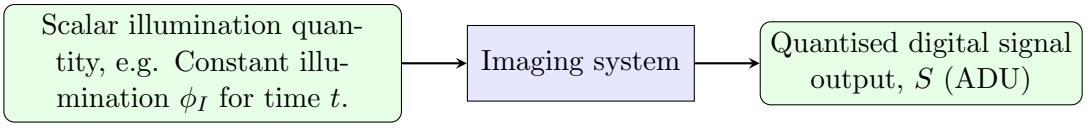

FIGURE 3.6: The imaging system considered as a black box with input and output quantities.

3.4.2 Conversion Gain

The conversion gain is a coefficient representing the number of photo-generated electrons (e^-) per ADU of the ADC, however; this value can also be represented in $\mu V/e^-$ – the voltage output from the device and input to the ADC. Depending on the characteristics of a device it is common to regard the conversion gain as a constant over a known range of signal, however; the inherent non-linearity of a system has to be considered in many cases, for example: many imaging devices are non-linear and cannot rely on such an approximation to return useful data. The conversion gain is obtained by observing the

x-intercept of the isolated shot noise characteristic line on the PTC. This process is detailed in Section 3.4.3.

An ADC with a bit-depth of N bits can register 2^N different values over an input voltage range from zero to ADC saturation. This project uses 16 bit ADCs with 65,536 discrete possible values. For signal conditioning a 6dB attenuator was used in some cases where the full-well capacity of the device caused a signal too large for the input of the ADC. This effectively halves the input voltage seen by the ADC and changed the conversion gain for some of the results.

3.4.3 Characteristic Noise Performance Regimes

A PTC features four distinguishable regimes over the range of mean signal (S), from zero ADU to full well [26]. If some regimes are not visible then it is an indication that the test set-up is inadequately configured or systematic errors are at play, potentially causing one noise source to dominate another at an unusually low signal. For the purpose of discussion an ideal PTC is shown in Figure 3.7. The solid line represents the total noise of the system $\sigma_{\text{Total}}(S)$, which can be expressed as the individual noise sources (detailed in Table 3.3) added in quadrature

$$\sigma_{\text{Total}}(S) = \left(\sigma^2_{\text{Read}} + \sigma^2_{\text{Shot}}(S) + \sigma^2_{\text{Fano}}(S) + \sigma^2_{\text{FPN}}(S)\right)^{1/2} \tag{3.1}$$

however; Fano noise will not be considered in the scope of this work as it is inapplicable to the optical λ range. Fano noise is the variance in the number of electron-hole pairs produced when a higher energy photon (e.g. soft X-ray) interacts with the silicon lattice. The 639 nm LED used for experimentation corresponds to a photon energy, E, of 1.94 eV

using the relationship

$$E(\text{eV}) = \frac{hc}{\lambda} = \frac{1.24}{\lambda(\mu\text{m})} \tag{3.2}$$

while Fano noise only becomes applicable for photon energies above 10 eV [26]. From Eq. (3.2) the Fano noise threshold is calculated as being relevant for wavelengths below $\lambda \leq 124$ nm, in the UV region of the electromagnetic spectrum.

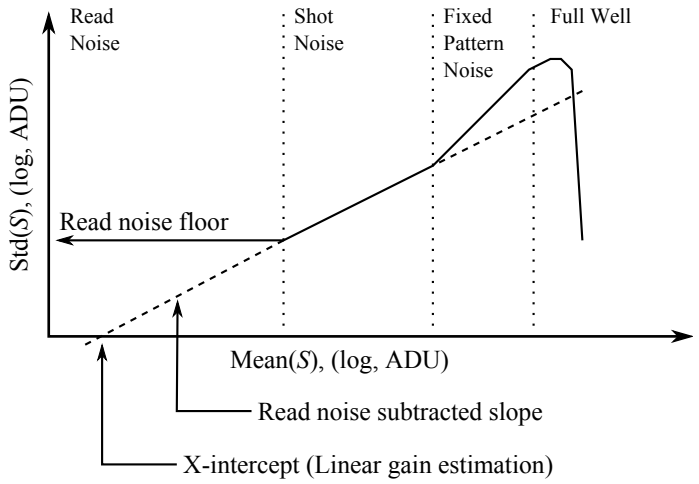

FIGURE 3.7: An ideal PTC showing the regimes identified by their typical characteristics, plotted on log-log axes [26].

The fundamental line determining the conversion gain of the system is the read-noise subtracted and shot-noise limited slope, labelled in Figure 3.7 as the second regime of four. It is shown extending into the other regimes using a dashed line. RMS shot noise, also known as Poisson noise is a Poisson process, scaled by the arrival rate of photons per pixel, ϕ_I and quantum efficiency, η_i.

$$\sigma_{\text{Shot}}(S) = (\eta_i S)^{1/2} \tag{3.3}$$

Photon Transfer Curve Noise Components	
σ_{Read}	Read Noise - A constant noise contribution irrespective of signal, attributed to the output signal chain amplifiers and analogue to digital conversion.
$\sigma_{\text{Shot}}(S)$	Shot Noise - A noise source that varies with respect to the arrival rate of photons, proportional to the square root of image signal. Shot noise only becomes apparent when the signal reaches a level at which the noise of the arrival rate of photons exceeds that of the read noise.
$\sigma_{\text{FPN}}(S)$	Fixed Pattern Noise - Emerges due to a differing response between pixels, which becomes apparent at higher signal levels. FPN has a slope of one as it scales proportionally with mean signal.
$\sigma_{\text{Fano}}(S)$	Fano Noise - Noise caused by the chance for a higher energy (e.g. X-ray) photon to produce multiple electrons. This is not relevant to this study which focuses on optical wavelengths, which are not subject to Fano noise.

TABLE 3.3: Noise sources contributing to the Photon Transfer Curve (PTC)

Where

$$S = \phi_I \eta_i \tag{3.4}$$

In order to extract $\sigma_{\text{Shot}}(S)$ from $\sigma_{\text{Total}}(S)$, first σ_{Read} and $\sigma_{\text{FPN}}(S)$ must be calculated. The "fixed pattern" can be removed by frame differencing: the pixel-by-pixel subtraction of one frame from another, taken in identical illuminating conditions. Due to the superposition of the two frames the noise increases by a factor of $\sqrt{2}$, thus the resultant data must be divided by $\sqrt{2}$.

$$\left(\sigma_{\text{Shot}}(S)^2 + \sigma_{\text{Read}}^2\right)^{1/2} = \frac{\sigma_{\Delta}(S)}{\sqrt{2}} \tag{3.5}$$

This leaves the quadrature subtraction of σ_{Read}, which is a case of generating zero photo-generated signal data from the over-scan region of image area. Care must be taken in generating this data, for instance - in the presence of image area signal and serial CTI, charge will manifest in the over-scan region. For this reason it is appropriate

to gather read noise from a dark device.

$$\sigma_{\text{Shot}}(S) = \left(\frac{\sigma_{\Delta}(S)^{\,2}}{\sqrt{2}} - \sigma^2_{\text{Read}} \right)^{1/2} \tag{3.6}$$

The x-intercept of the extracted shot noise curve represents the reciprocal of the conversion gain. A way of corroborating the conversion gain by plotting a Mean-Variance PTC is detailed in Section 3.4.4.

3.4.4 Mean-Variance PTC

The Variance PTC (V-PTC) exploits the relationship where the mean, $\mu(e^-)$ is equal to the variance, $\sigma_{Shot}(e^-)^2$ given the system obeys Poisson statistics.

$$\mu(e^-) = \sigma_{\text{Shot}}(e^-)^2 \tag{3.7}$$

(Assuming the previous quadrature elimination of σ_{Read} and $\sigma_{\text{FPN}}(S)$)

$$\frac{\sigma_{\text{Shot}}(S)^2}{\mu(S)} = K_{\text{ADC}}(e^-/\text{ADU}) \tag{3.8}$$

thus, the linear conversion gain K_{ADC} can be derived from the gradient of the V-PTC plot, while the source data S obeys Eq. (3.7).

3.5 Summary

In order to establish a base camera system on which the optical characterisation system of Chapter 4 may be built, this chapter details the configuration of chamber-side

camera hardware, camera electronics and the operation and calibration of the system. A hardware layout has been constructed for operating the CCD273 close to an optical window while maintaining mission-like temperature and the required vacuum to prevent electronics freeze-out. The system operation and the methodology used for calculating the conversion gain has been described, and this is the basis by which all experimental data has been acquired.

Chapter 4

Optomechanical Design

4.1 Introduction

Following on from Chapter 3 in which laboratory instrumentation is configured and characterised, Chapter 4 documents the design, construction and characterisation of the optical test system utilised in the following experimental chapters. The final system encompasses a library of bespoke software solutions in addition to a custom optomechanical construction.

The optical system design was approached with several goals in mind:

1. Projection of repeatable galaxy-shaped objects in order to make the data from the study relate to Euclid VIS. In this case "galaxy-shaped" refers to a small point-source illumination, isotropic and not eccentric in nature with the purpose of later measuring any system-induced shape distortion.

2. Repeatable auto-focusing of point source illuminations. The smaller the spot size, the better - for the purpose of an impulse-like pixel response.

3. Repeatable positioning of spot projections with respect to the column and row coordinates on the CCD.

4. Ability to project acceptably uniform (e.g. flat over a region of interest) flat fields to generate a Photon Transfer Curve (PTC) for system calibration.

The above goals were interpreted as a requirement for two separate projection subsystems, mounted on a three-axis translation stage subsystem - enabling positioning and focus for the spot projection, and fine-tuning of a diffuse flat field. Sections 4.1.2 and 4.1.3 detail the development of the Spot Projection Assembly and the Flat-field Projection Assembly, respectively. The Translation Stage Asssembly is discussed in Section 4.1.4. A map showing the interfacing paths between subsystems of the complete system is presented in Section 4.1.5, prior to discussion of software algorithms employed for system operation and characterisation in Section 4.2.

4.1.1 Terminology and Initial Considerations

The core work in this chapter involves focusing a beam of light down to a small spot with a repeatable PSF. Ideally "focusing" refers to the process in which a beam of light converges down to an infinitesimally small point. In reality, a spot focus is subject to diffraction and is therefore widened. Further widening as a result of imperfections in the optics include chromatic and spherical aberration (amongst many others not discussed here). Chromatic aberration is the axial dispersion of light from different wavelengths, which is not relevant to narrowband illuminations such as that from LEDs or lasers. Spherical aberration is more pertinent in the respect that the focal point may vary across the surface of a given lens, leading to axial dispersion of light from a single wavelength. This system utilises achromatic doublets, which are compound lenses

of different refractive indices compensating for chromatic aberration. Achromats were used with the purpose of testing with LEDs of varying wavelengths, but time constraints prevented that. Spherical aberrations present are not considered as the output of the spot projection assembly of Section 4.1.2 was considered good enough to contain the majority of the PSF within one target pixel, and the eight surrounding peripheral pixels.

The PSF is also affected by the absorption depth of incident photons, as discussed in Section 6.3.1. The testing was conducted with a Front-Illuminated (FI) CCD and a red light source only, therefore it could be theorised that in a future experiment where blue light is used the PSF measured could be smaller. The rationale behind this assertion is that with a FI, charge will be generated closer to, or inside the influence of the electrodes as opposed to being allowed to diffuse in the field-free region. An equivalent study with a Back-Illuminated (BI) device would demonstrate these hypotheses.

4.1.2 Spot Projection Assembly

The ThorLabs, Inc. SM1, 1" lens tube system was selected as the most cost effective and adaptable method of engineering an enclosed spot projection in a lit lab environment. Figure 4.1 illustrates the transmissive optical configuration used. A 5 µm pinhole is LED-illuminated and imaged onto the detector through an achromat pair. Achromatic doublets were chosen to reduce the spherical aberration at any given wavelength and chromatic dispersion over multiple wavelengths, however; in the course of the study only a narrow-band 639 ± 10 nm (red) ThorLabs LED630E [27] LED was utilised.

The CCD273 pixels are 12 µm in size therefore it seemed prudent to use a different sensor with smaller pixels to align the pinhole and calibrate the optics in the spot projection assembly. A CMOS Jade APS with 5.8 µm pixels [28, 31] was positioned at the 50 mm

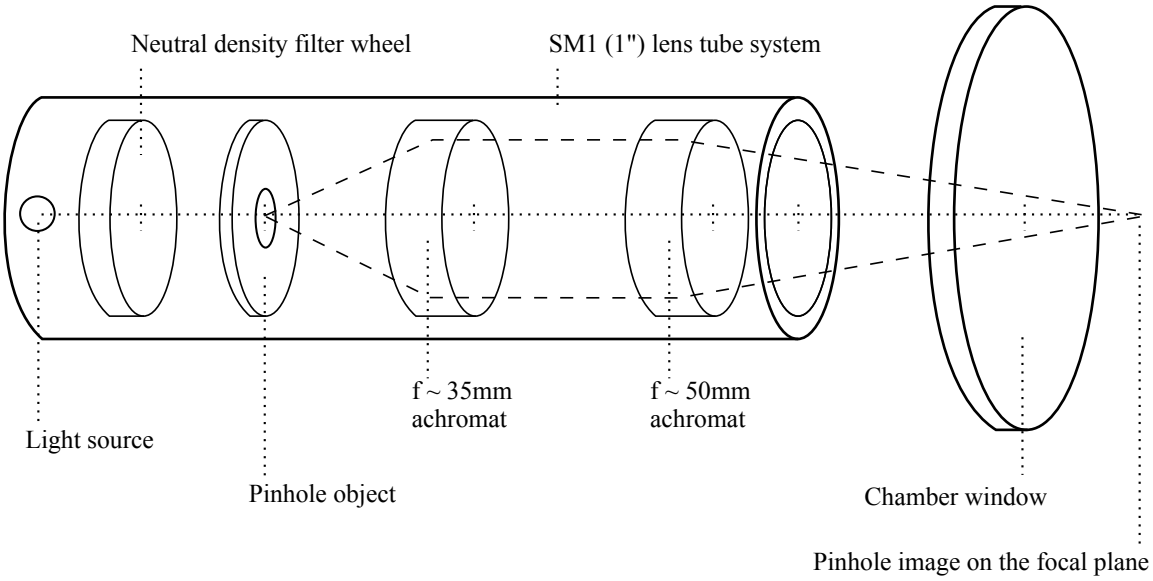

FIGURE 4.1: The spot projection optics, part of two optical projection systems mounted on the 3-axis translation stage.

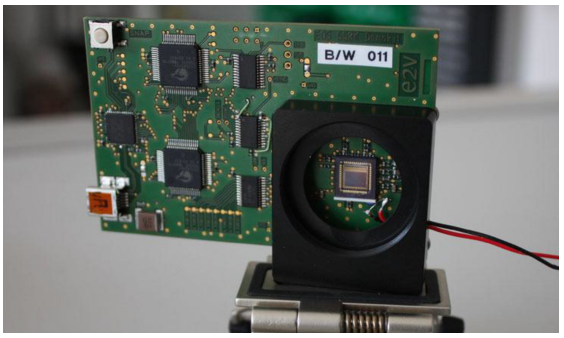

FIGURE 4.2: The CMOS Jade APS sensor board used for focusing the fixed Spot Projection Assembly (Image credit: Ben Dryer).

working distance and the positions of the preceding elements were adjusted utilising a side window in the threaded SM1 lens tube until the spot appeared in sharpest focus by visual inspection. A six-slot ThorLabs, Inc. filter wheel populated with five orders of magnitude of Neutral Density (ND) filters was added between the light source and the pinhole in order to control the optical flux. This would later enable more flexibility in generating Photon Transfer Curves (PTC) over multiple orders of magnitude of signal levels.

4.1.3 Flat-field Projection Assembly

The Flat-field Projection Assembly, shown in Figure 4.3 consists of the same type of 639 ± 10 nm ThorLabs LED630E used for spot projection, followed by a ThorLabs ED1-S50 engineered diffuser. The diffuser was positioned inside an SM1 lens tube at a forward axial distance of 25.4 mm from the LED. The LED-facing micro-lensed surface is designed to intercept a beam of 0.5 mm or greater, such that the exiting beam renders a 50 ° divergent, diffuse and square pattern. Taking into account the ± 15 ° normalised radial intensity distribution specified by the LED data sheet, the diffuser "sees" an adequate diverging beam width of 13.6 mm. The divergence θ_v, of a beam of length l, with terminating beam widths D_i (start) and D_f (end) is provided by the relationship in Equation 4.1.

$$\theta_v = 2 \cdot \arctan\left(\frac{D_f - D_i}{2l}\right) \tag{4.1}$$

Rearranging Equation 4.1 for D_f as in Equation 4.2, allows the CCD coverage of the approximated flat field beam to be calculated as a function of the divergence, θ_v and the distance from the diffuser to the axial position of the CCD focal plane, l.

$$D_f = 2l \cdot \tan\left(\frac{\theta_v}{2}\right) + D_i \tag{4.2}$$

The starting width of the diverging beam, D_i was calculated as 13.6 mm and the divergence θ_v is stated by the manufacturer as 50 °, thus Equation 4.2 can be simplified to Equation 4.3 to give the flat field coverage as a function of l only. This linear relationship is illustrated in Figure 4.4.

$$D_f = 0.93 \cdot l + 13.6\text{mm} \tag{4.3}$$

The diffuser data sheet [29] illustrates the angular intensity profile, demonstrating a

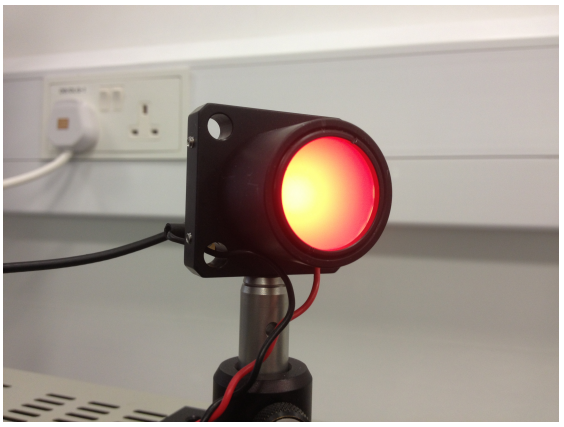

FIGURE 4.3: The initial solution used for the Flat-field Projection Assembly.

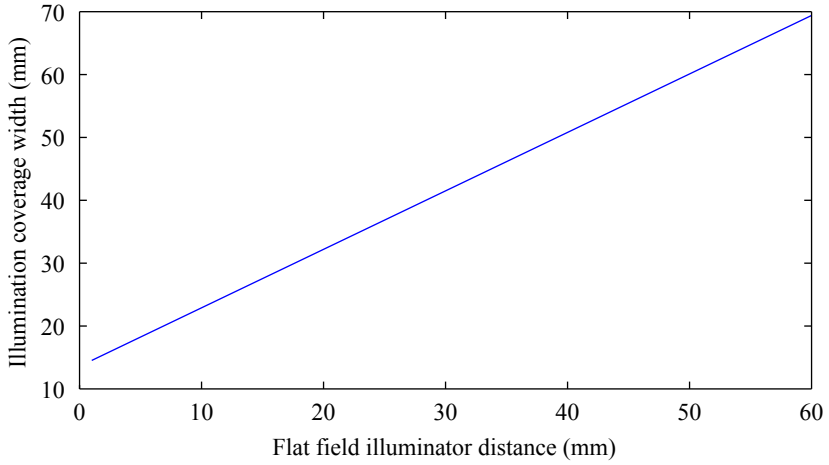

FIGURE 4.4: The flat-field coverage width as a function of the working distance of the diffuser grating from the CCD.

range between absolute values of 0.7 and 0.9 intensity across the 50 ° divergence. This information combined with the above calculation was indicative of how the flat-field illumination system would perform, however: assumptions were made in neglecting reflections and the position of the optics was assumed to be centred over the focal plane.

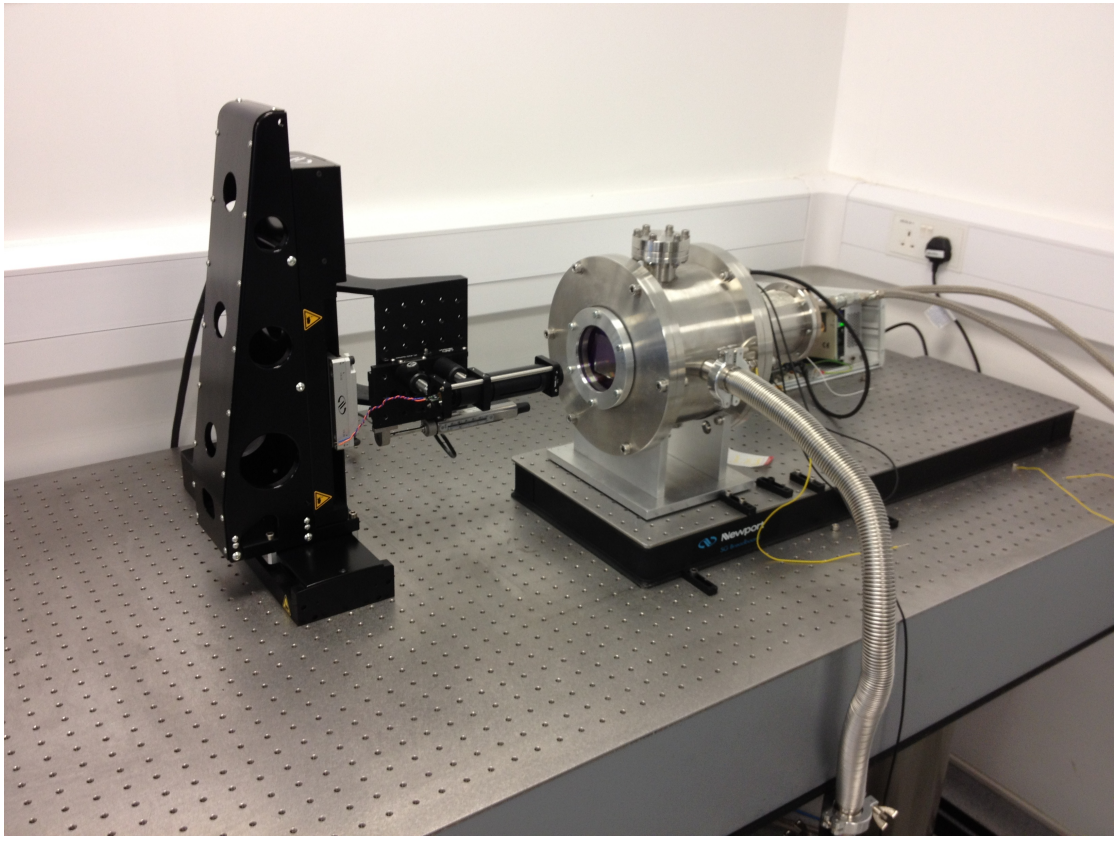

FIGURE 4.5: An early iteration of the spot projection optics and translation stage assembly, prior to light-tight isolation with an optical enclosure.

4.1.4 Translation Stage Assembly

To direct the spot projection assembly at individual specific pixels on the CCD a three-axis translation stage was assembled. Figure 4.5 illustrates an early opto-mechanical layout while Table 4.1 details the manufacturer-stated repeatability limitations of each translation stage axis. For precautionary validation, the system-wide spot positional repeatability was tested by scanning a spot across the CCD in a cyclic square pattern, stopping at each corner to capture a spot image. A Region Of Interest (ROI) was established around each spot projection site and the centre of mass of the ROI was measured for each frame in the row and column directions. The spot illumination level was deliberately bright enough but below the pixel full-well capacity so as to dominate

any noise. The positional spreads for x (column) and y (row) directions were calculated using the standard deviation of 100 repetitions, as shown in Table 4.2. The positional error in nanometres was calculated by converting the absolute pixel centre of mass to metres by multiplying by the 12µm known pixel size.

Axis	Travel (mm)	Part Number	Guaranteed Repeatability
x-axis (Horizontal)	100	ILS100CC	± 1 µm Bi-directional, 1 µm Uni-directional
y-axis (Vertical)	100	ILS100CC	± 1 µm Bi-directional, 1 µm Uni-directional
z-axis (Optical)	50	LTA-HS	± 1 µm Bi-directional, 0.5µm Uni-directional

TABLE 4.1: The translation stage axes configuration and manufacturer-given repeatabilities [30, 31].

#	Positional Spread X: (pixels)	Positional Spread Y: (pixels)	Positional Spread X: (nm)	Positional Spread Y: (nm)
1	0.0056	0.0063	67.2	75.6
2	0.0061	0.0028	73.2	33.6
3	0.0052	0.0035	62.4	42.0
4	0.0051	0.0045	61.2	54.0

TABLE 4.2: The standard deviation or spread of spot position measurements in pixels and nanometres, at each position.

While the standard deviation is a reasonable measure of the positional repeatability over a large number of translations, it does not account for worst-case scenario instances. Taking the average of the full range of positions it was found that the mean full range was approximately 0.3 µm in both vertical and horizontal axes. In order to accommodate for this systematic error, a MATLAB function was written in order to process spot images returned by the camera and send appropriate adjustments to the translation stages to correct for positional error. This is covered in more detail in Section 4.2.1.

4.1.5 System Interface Map

The configuration of the entire experimental equipment is shown in Figure 4.6. The host PC is directly interfaced with camera electronics via USB, and the opto-mechanic translation stage server via Ethernet. The camera electronics uses two 5V TTL outputs to enable and disable constant current sources controlling the illumination of the flat-field and spot projection LEDs. The chamber headboard provides pre-amplification of CCD signals and interfacing with the CCD flexible D-types for bias voltage and clock signal control.

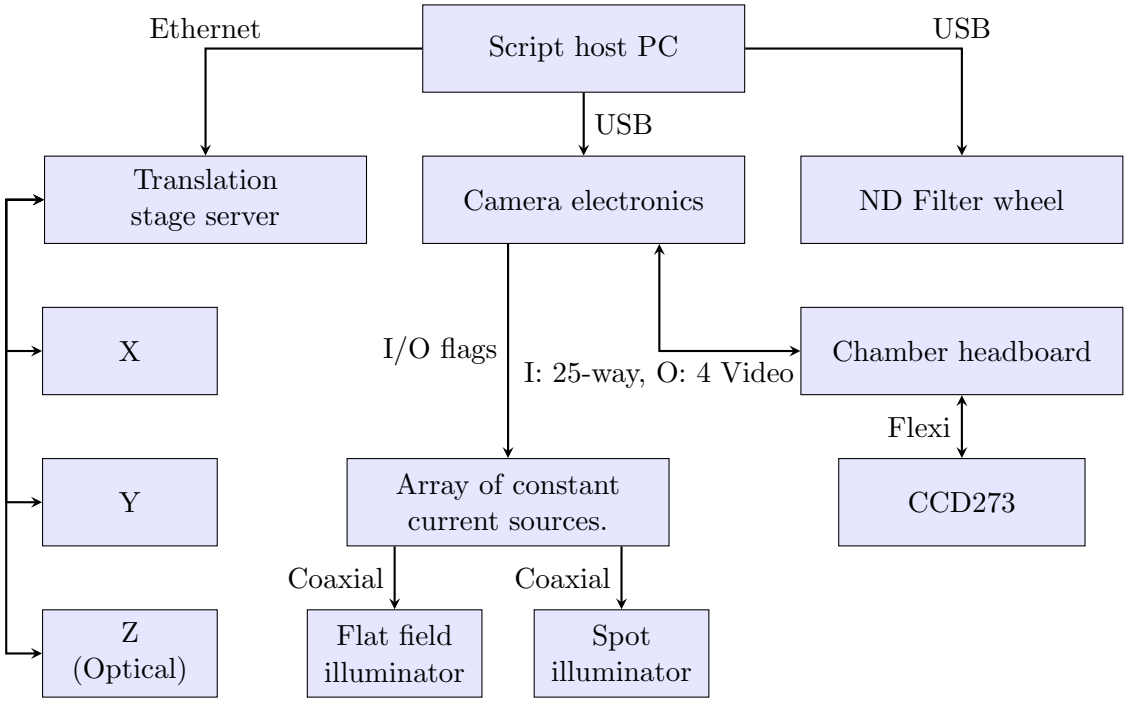

FIGURE 4.6: An overview of the complete projection, camera electronics and data acquisition systems.

4.2 Software and Algorithms

All operations, data acquisition and processing programs were written in Mathworks® MATLAB®. This section explores the function and performance of the software subsystems. The methodology detailing the focusing and positioning of the spot in Section 4.2.1 will be followed by an assessment of spot size estimation techniques in Section 4.2.3. The way in which systematic error sources are monitored using software is discussed in Sections 4.2.2, 4.2.4 and further discussed in Section 5.4.

4.2.1 Focusing and Centring the Spot

Recall Section 4.1.2 in which the Spot Projection Assembly was initially constructed and focused on a static target. When transferred to the moving carriage of the translation stage, the focal distance became approximate - thus the optimum focus needed to be found algorithmically. Optimum focus was achieved by first manually focusing the spot by inspection then assigning a stepped range of axial (z-stage) positions around the manual focus by which to capture spot images. Over the focal range multiple images were taken at each position in order to average out any noise. The use of spot image averaging, promoted unwanted blurring of the analysed image, which is not detrimental to determining best focus, however; it prevents accurate spot PSF measurements. The solution to PSF blurring is discussed as the supporting narrative of Chapter 5, Section 5.4.

The principle of the spot focusing algorithm, referred to henceforth as *Region Autofocus* (RA), is to compare the charge in the centre pixel q_{Centre} with that of the eight bounding peripheral $q_{Peripheral}$ pixels and record a signal ratio for each position on the z-stage sweep. Figure 4.7 shows a 3×3 spot image, interpolated for the purpose of illustrating

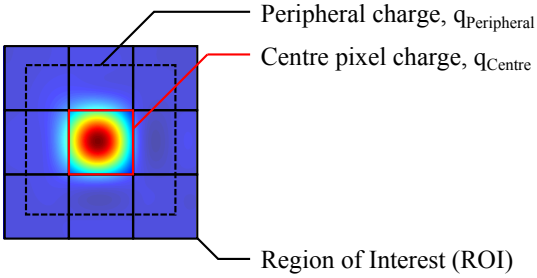

FIGURE 4.7: An interpolated 3×3 pixel spot projection ROI illustrating the centre pixel and periphery.

how the wings of the 2D spot profile spread over multiple pixels. Figure 4.8 outlines the behaviour of the converging light as it travels from the final lens in the Spot Projection Assembly and lands on the focal plane. An ideal lens devoid of any aberration or diffraction effects would focus light on an infinitesimally small vertex, however: due to spherical aberration each annulus of the lens aperture has a slightly different focal distance causing a dispersion of the focal point [32]. In the absence of spherical aberration, the minimum spot size due to diffraction effects is the lower limit on the PSF size, with the presence of any spherical aberration widening the PSF. The minimum width of the beam is widened due to diffraction and an approximately Gaussian beam waist manifests. The diffraction-limited spot sized is calculated using the Rayleigh Criterion in Equation 4.4 as being approximately 1.3 µm [33], while the increase due to spherical aberration is unknown and would require ray-tracing to calculate. When axially translating the optics the aim is to ensure that although the focal point is impossible to achieve, the beam is focused at the narrowest point of the beam waist.

$$D_{Airy} = 2.44\lambda \cdot (f/\#) \tag{4.4}$$

Figure 4.9 illustrates a more simplified version of the RA algorithm, which begins with the host PC using a look-up table of physical translation stage coordinates in order

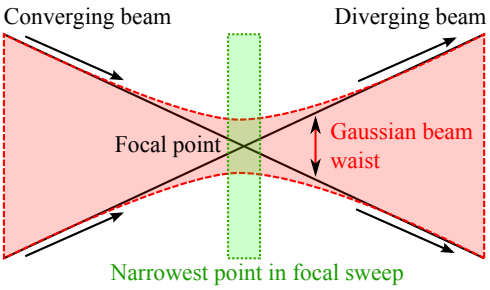

FIGURE 4.8: A Gaussian beam waist of exaggerated vergence, showing the focal point and narrow region where the beam width is approximately consistent throughout.

to position the spot projection over a pixel of interest. Using a translation stage for such a task is subject to some spot de-centring and this is corrected for by moving the translation stage in the x-y plane, opposite to the measured centre of mass. The centre of mass in x and y is measured using the weighted moment of each pixel as in Equation 4.5, which shows the calculation of the centre of mass, C_{row}, in the row (horizontal) direction. Equation 4.6 illustrates the same equation adapted for the centre of mass in the column (vertical) direction. A perfectly centred spot image reports a $[C_{row}, C_{col}] = [R_{row}, R_{col}]$, where R_{row} and R_{col} represent the middle coordinates of the Region Of Interest (ROI). The re-centring vector is calculated as in Equation 4.7, where the measured centre of mass is differenced with the ROI centre coordinate, then scaled with the pixel size, P. The vector is a three-element array representing the desired displacement of the translation stage in x, y and z. Since there is no desired displacement in the optical axis (z), the third element is zero.

$$C_{row} = \frac{x_{col_1} \sum signal_{col_1} + x_{col_n} \sum signal_{col_n} \cdots}{\sum signal_{col_1} + \sum signal_{col_n} \cdots} \tag{4.5}$$

$$C_{col} = \frac{y_{row_1} \sum signal_{row_1} + y_{row_n} \sum signal_{row_n} \cdots}{\sum signal_{row_1} + \sum signal_{row_n} \cdots} \tag{4.6}$$

$$[R_{row} - C_{row}, R_{col} - C_{col}, 0] \times P \tag{4.7}$$

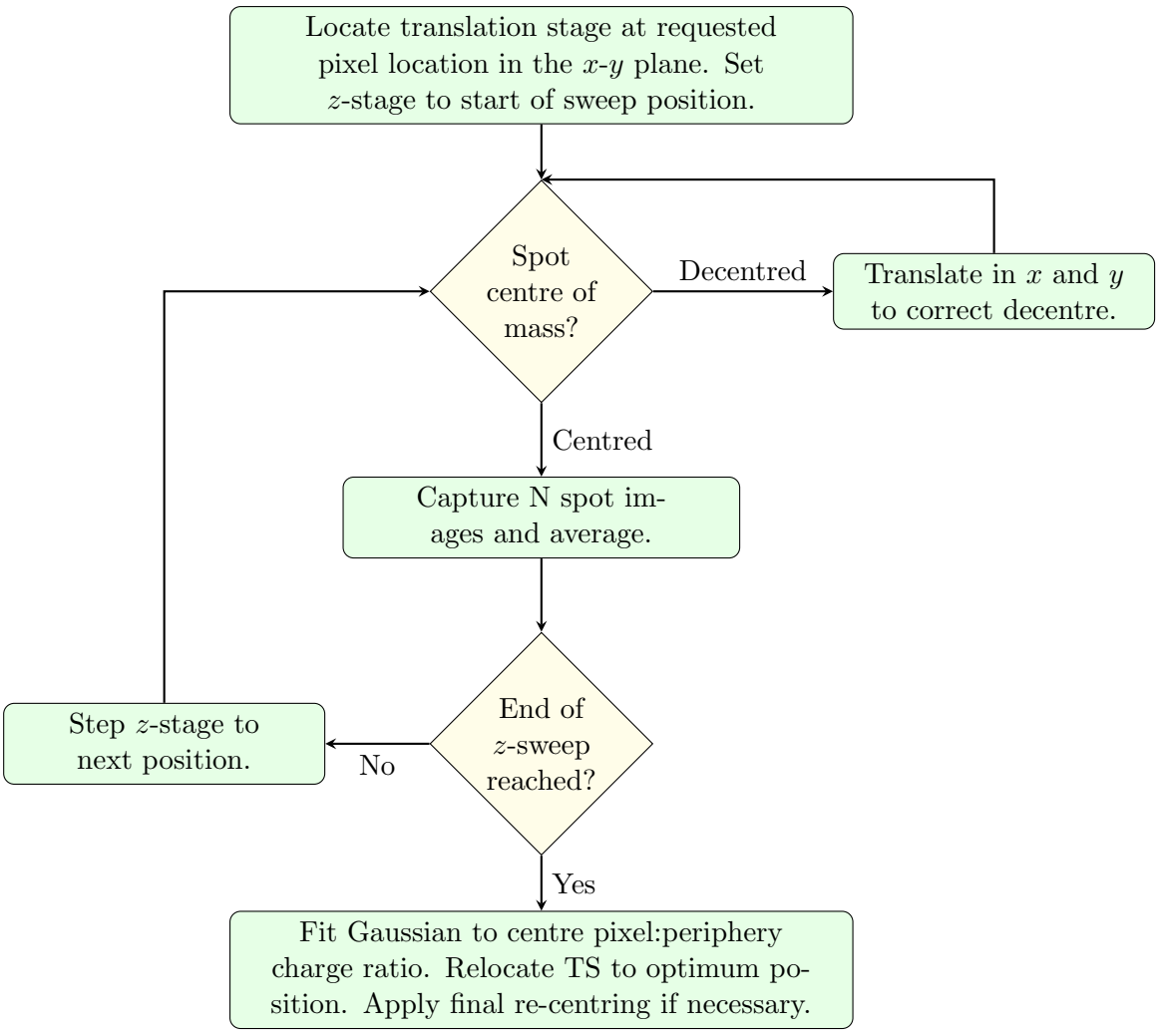

FIGURE 4.9: The Region Autofocus Algorithm

In order to visualise how the spot PSF evolves through a focusing sweep, Figure 4.10 illustrates a line profile through the middle of an 11×11 spot ROI as the spot is translated over 500×10 µm steps. Observing the centre pixel signal from this 3D dataset, Figure 4.11 plots the centre pixel signal q_{Centre} against axial position of the optics, indicating the optimum focusing position from a Gaussian fit to be at 299 z-steps or 2.99 mm from the sweep starting position.

Focusing a spot on a known pixel location yields some information which can be used to predict where the optimum focus is regionally in neighbouring pixels, but also on other

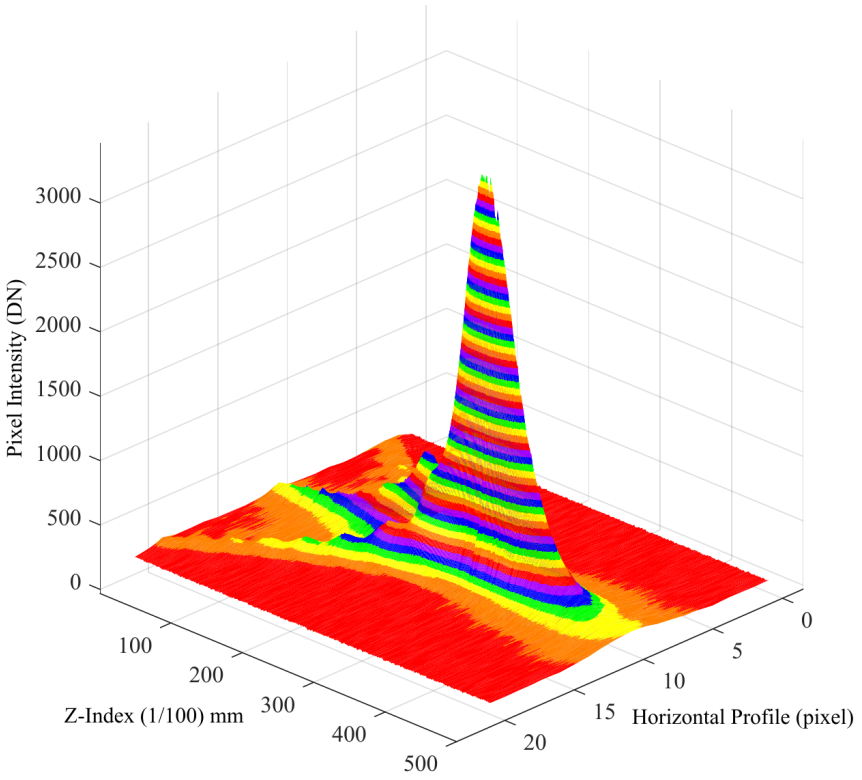

FIGURE 4.10: 500 line profiles over 5mm of focusing distance, plotted as a surface. [N.B. Texture shown is used for contour effect and is not a colour axis.]

areas of the device. Recall Section 3.2.1 where the CCD is mounted on the cold bench, within the window flange - this required high accuracy to ensure the safety of the device bond wires, however the flatness of the device with respect to the translational axes is subject to positional and alignment error. In light of this issue, the optimum spot focus cannot be assumed to be uniform across the device, and has to be re-measured whenever the region of interest is relocated.

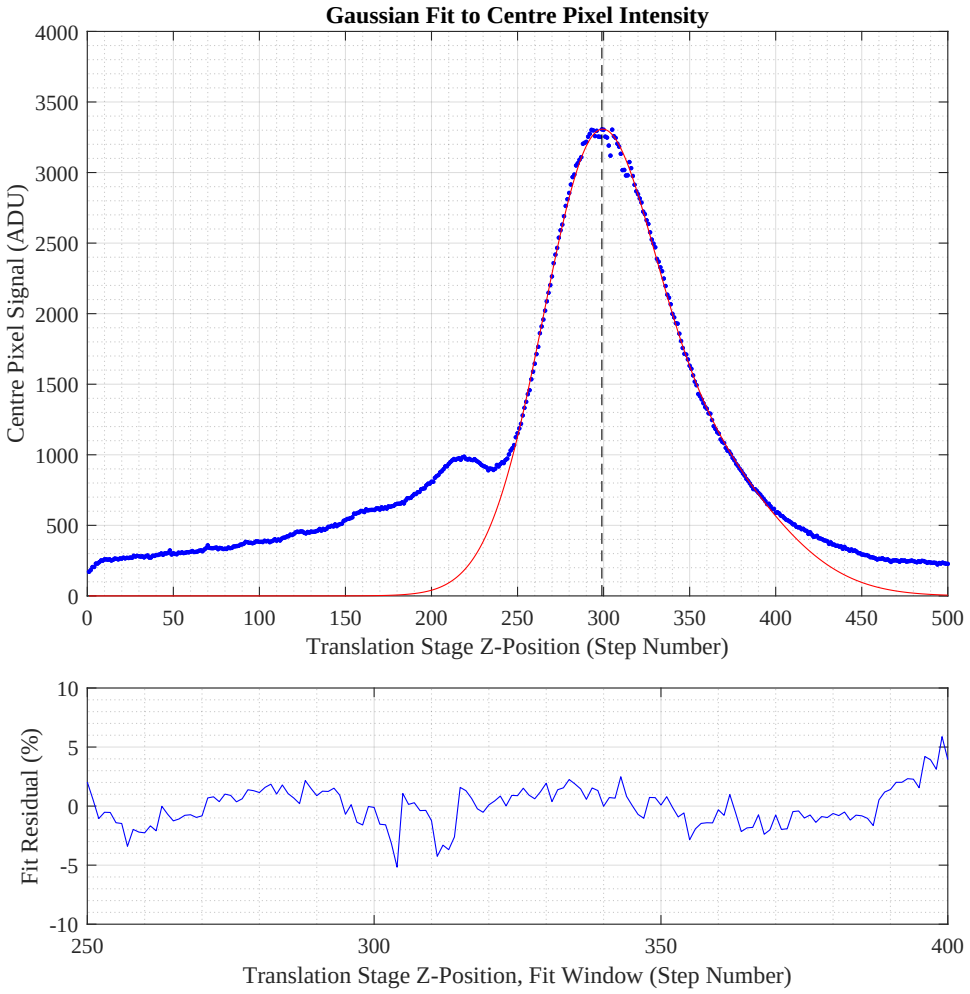

FIGURE 4.11: The ratio of charge in the centre pixel to the periphery over the course of a 500-position focus sweep in the optical z-axis.

4.2.2 Approximating Focal Plane Flatness

Utilising the z-position focus sweep used in Section 4.2.1, it was possible to focus the spot on multiple pixels across an entire quadrant of the device in order to infer the relative flatness of the device, with respect to the translation stage vertex. This was achieved by measuring optimum focus for a grid of positions in the x and y directions. The surface of Figure 4.12 illustrates the returned optimum focus z-position of each of the locations in a 400 point 20×20 pixel grid. The figure appears noisy, with local neighbours not as similar as expected, and this is attributed to the re-homing of the translation z-stage position between each focusing run. It is clear that the ever so slightly skew mounting of the CCD on the M4 studs that protrude from the chamber rear causes a range in optimum focusing distance of the order half a millimetre.

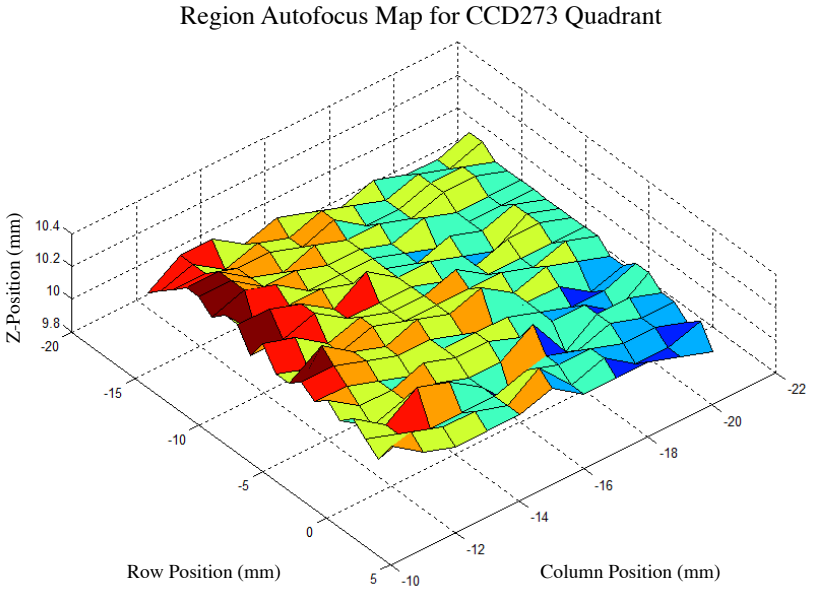

FIGURE 4.12: A surf of optimal focal distance at periodic positions around the node of the CCD273. Note that this does not measure the flatness of the CCD273, which is manufacturer stated to be in the order of microns.

4.2.3 Measuring Point Spread Function

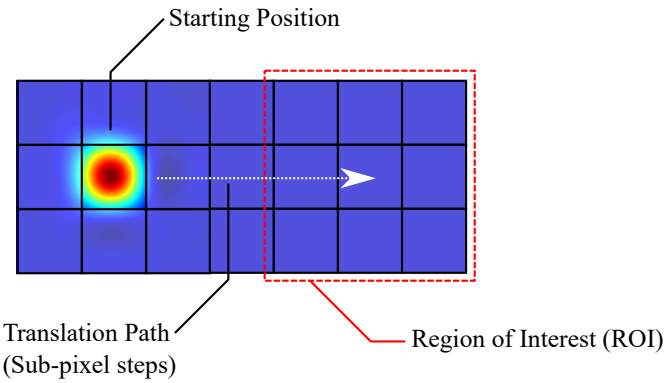

FIGURE 4.13: Virtual knife-edge measurement methodology, featuring a spot translated in sub-micron steps into a ROI in which the total signal change is measured with respect to translation steps.

The detector PSF is not to be confused with the total system PSF. In reality the system has at least two components: the optical PSF and the detector PSF. In the scope of the experiments within this thesis, only the relative system PSF as a function of experimental parameters is considered. The drawbacks of this approach are discussed in Chapter 8. Presented here are multiple approaches used to estimate the spot size, typically characterised by a scalar number denoting a width in microns: the Full-Width at Half Maximum (FWHM).

Figure 4.13 illustrates the Virtual Knife-Edge Measurement (VKEM) technique [34]. A spot is focused with the RA algorithm as in Section 4.2.1 and translated by sub-pixel steps in the row or column direction depending on whether a vertical or horizontal spot profile is desired. For each step of the translation stage, the signal level in an empty region of interest is recorded until the spot projection has entered it entirely. This method is a way of using the sub-micron positioning capability of the translation stages to increase the sampling capability of the CCD. The increase in total ROI signal is demonstrated by the Edge Spread Function (ESF) of Figure 4.14.

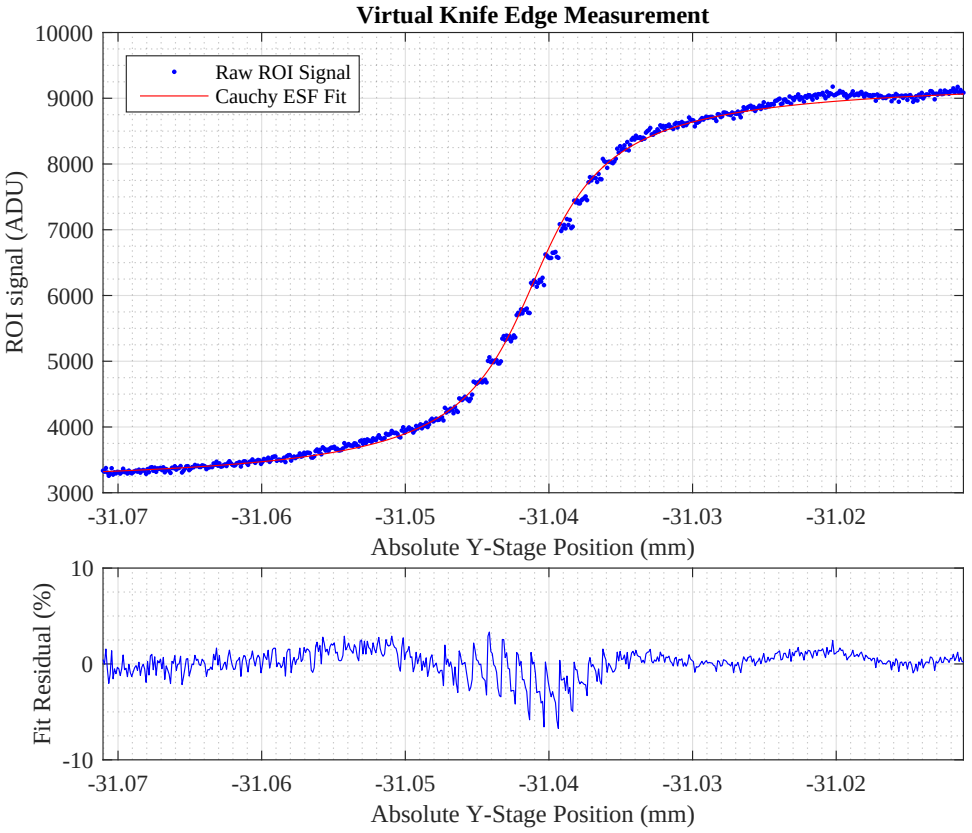

FIGURE 4.14: Virtual knife edge measurement (VKEM) illustrating the ROI sum and a Cauchy fit. Note the ripple following the plateau which could perhaps be attributed to an Airy diffraction pattern.

The nature of the VKEM technique is such that the ESF may be differentiated to yield the PSF of the translated spot. Simply differentiating the raw ROI signal is not a viable option due to ESF noise and positioning limits of the translation stage position, made apparent by point clusters at the steepest part of the signal trend. Following recommendations of Barney Smith et. al. [35], a Cauchy ESF fit was chosen to allow for a lower noise differentiation, resulting in the PSF of Figure 4.15. Here it is shown that the FWHM is contained within a sub-pixel 8 µm, while the full influence of the spot is felt for several tens of microns.

A less time-consuming method of approximating the PSF is to apply a Gaussian fit directly to the pixel-sampled spot data. A direct Gaussian fit is a less accurate method

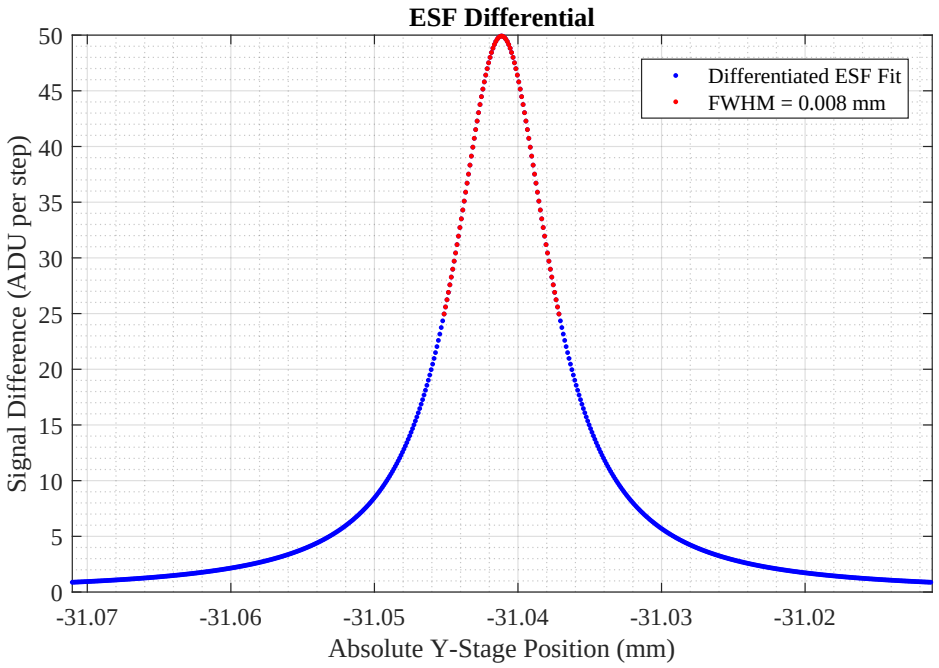

FIGURE 4.15: FWHM estimate generated by a virtual knife-edge measurement. The X-axis of data shown corresponds to translation stage steps in the physical Y-direction, while the Y-axis is a difference function applied to the Cauchy ESF fit. In this case, FWHM is given relative to translation stage units, or millimetres of translation stage travel.

because the spot is massively under-sampled compared to the VKEM technique. The Gaussian fit is improved via further analysis of a 3×3 spot ROI, which offers a way in which symmetry can be manipulated through centre of mass re-centring, as demonstrated in Section 4.2.1. Figure 4.16 illustrates a slice of a spot ROI with a Gaussian fit applied around the spot centre. In many instances in this study, the relative system PSF from a direct Gaussian fit will be examined rather than VKEM.

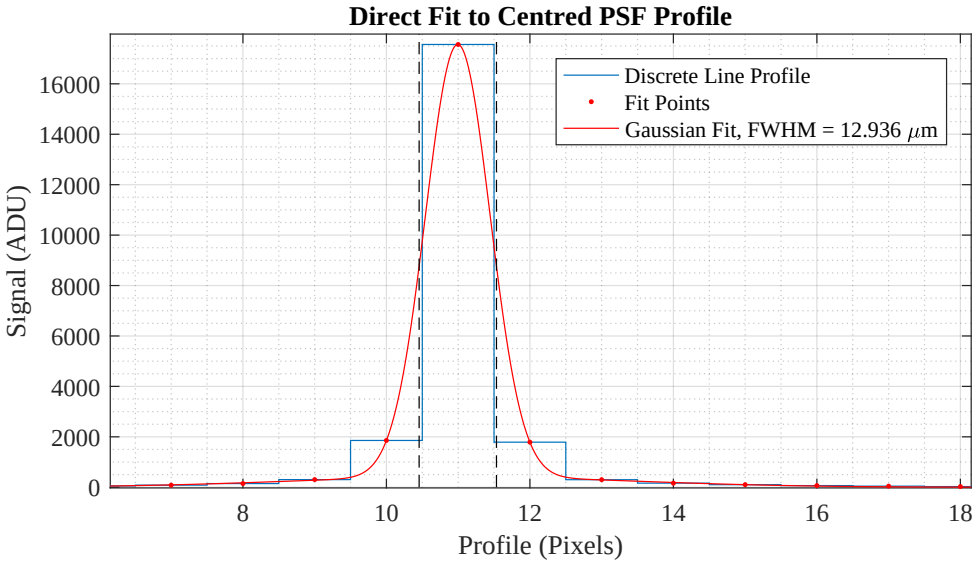

FIGURE 4.16: Gaussian fit to pixel centres used to find the FWHM of a high signal spot. Dashed vertical lines are aligned with the half maximum value on rising and falling edges.

4.2.4 Assessing Light Tightness

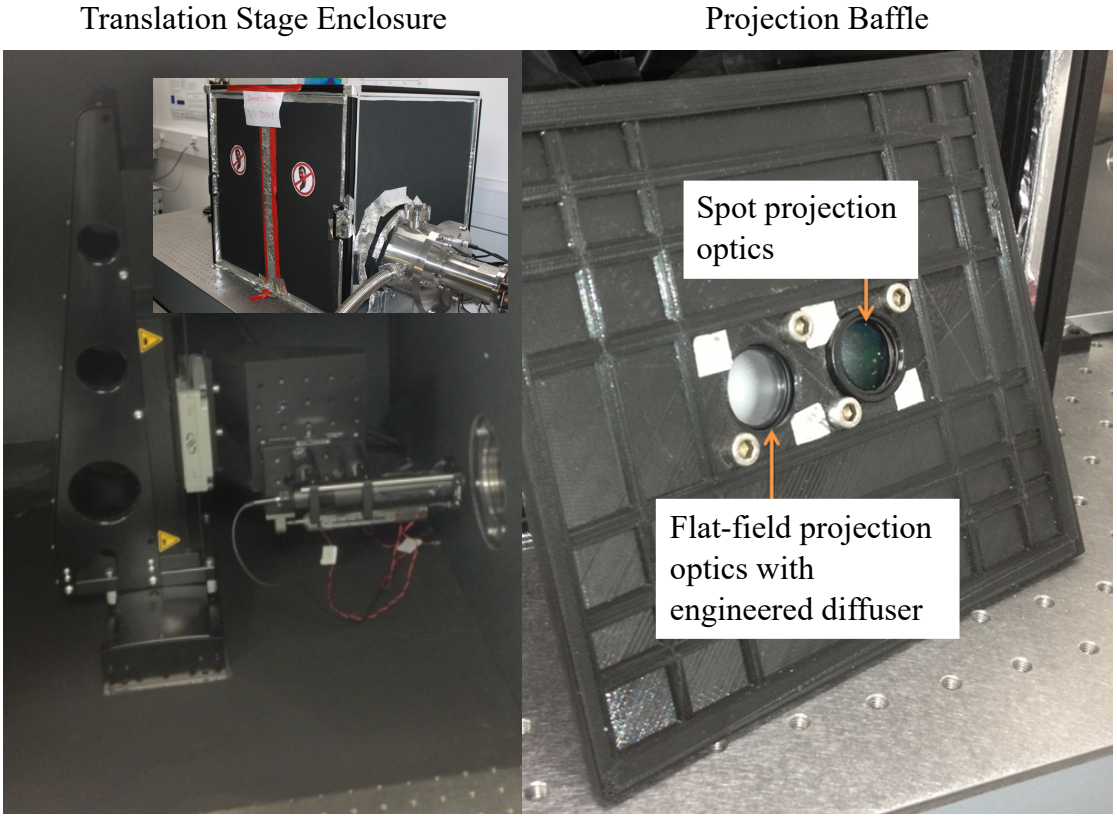

FIGURE 4.17: The dark box and baffle constructed in order to block out stray light from the laboratory and attenuate light from the translation stage IR encoders at times when they cannot be disabled.

As in Figure 4.17, a ThorLabs optical enclosure consisting of black anodised aluminium extrusions and matte foam-core board was constructed and further supplemented with aluminium tape in order to provide a light-tight environment for the translation stage and optical assembly. Figure 4.18 demonstrates the average frame signal for a continuous acquisition conducted over a ten hour period from mid-afternoon. The point at which the laboratory lights are turned off for the night, and the ensuing system stability is clearly visible. In response to this discovery, improvements were made to the light isolation until a stable system performance was achieved.

While ambient laboratory stray light was eliminated, it was also discovered that the ILS100CC translation stages used for the x and y axes of movement feature IR encoders

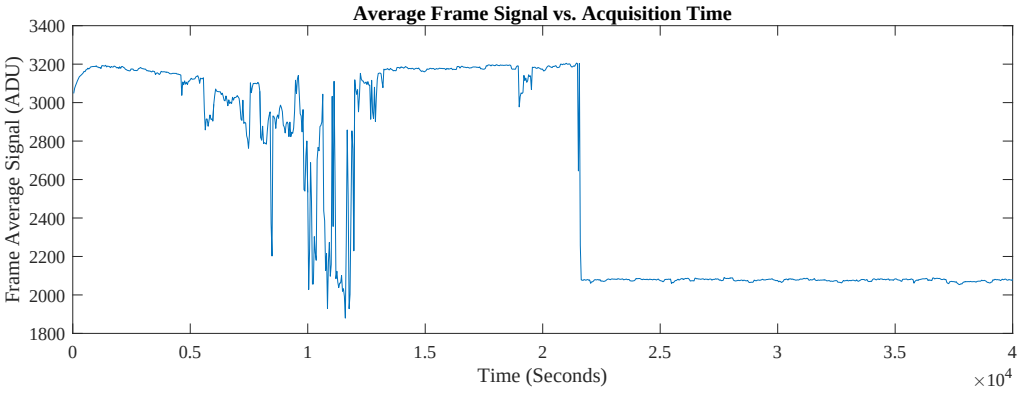

FIGURE 4.18: The imaging area mean signal versus time, for a frame integration every 40s for approximately 10 hours.

that release stray light into the optical enclosure. Stray light and noise was to the detriment of the initial SP-PTC measurements of Chapter 5, therefore a scheme was devised such that the translation stages were switched off after their positioning routine, in order to avoid unwanted noise. For noise reduction during focusing and fine positioning requiring use of the x and y axis, a baffle was designed and 3D printed in order to allow through the apertures of the Spot Projection Assembly and the Flat Field Projection Assembly while greatly reducing stray light.

4.3 Summary

Building on the basis of the camera and cryogenic systems of Chapter 3, an optomechanical system has been designed, built and characterised so as to project focused spot images and flat field illuminations. Spot and flat field projections are the basis of the experimentation in Chapter 5 and Chapter 6, with the rationale of those chapters being the PSF response of the CCD273, and methods in which the PSF can be manipulated, respectively.

Considering the initial goals of the chapter in Section 4.1, and the outcomes of the system construction and characterisation:

1. Repeatable "galaxy-shaped" objects became more like "round test spots" as it became clear that a round projection that covers a small region of pixels (e.g. 3 × 3), is more useful than an eccentric object for measuring the effect of changes in system variables as in Chapter 7. Elliptical objects for imaging through the optics were available while using a 5 µm pinhole proved convenient and simplistic. The FWHM of spots projected was measured to be approximately 12 µm or less, depending on the method used. The direct fit method uses Gaussian fits which are perhaps not ideal for fitting to a PSF, however: they provide a reasonable basis for comparison of spot geometry for the following chapters.

2. Auto-focusing was initially an open-loop system which afforded spots of poor repeatability and variable FWHM. Using the live image feedback to reposition the spot in the image plane multiple times with each focusing z-step allowed for less jitter in the data used for ascertaining the optimal z-stage position.

3. Spot positioning was achieved as a closed-loop subsystem of the autofocus algorithm, using pixel values and a centre-of-mass calculation to move the translation stage in the x and y until the spot is centred over the target pixel.

4. A flat-field was achieved using a ground-glass diffuser and a second LED of the same characteristics of that used for the spot illumination. The flatness of the illumination is not as important for the PTC process in which frame differencing is used to remove FPN, but for the Multiple Illumination Experiment of Chapter 6 it is of importance. The flatness would ideally be measured using a single pixel response by translating the flat field over that single pixel and taking measurements,

effectively using it as a photodiode unit. This was deemed beyond the scope of the current work as the region of interest was a small fraction of the complete illumination area (100 pixels) therefore the manufacturer-stated flatness was deemed acceptable.

5. (Additional) Light tightness was achieved as an outcome of troubleshooting the PTC and taking images over night. This proved invaluable for eliminating environmentally-induced systematic errors such as room lighting.

Chapter 5

Single Pixel Photon Transfer Curve

5.1 Introduction

The Euclid mission requirements warranted an investigation into the spatial response of the detector selected for the mission: the Teledyne-e2v CCD273. The initial experimental rationale was to characterise the CCD273 response to a point source illumination, an optical object analogous to that of a distant galaxy entering the telescope field of view. In this chapter the spot projection system as commissioned in Chapter 4 is utilised to investigate the point source response and signal-to-noise performance by adapting Flat-Field Photon Transfer Curve (FF-PTC) generation techniques to consider a point source illumination. Furthermore, techniques are developed for eliminating noise sources in order to improve the quality of measurements made. In the course of study a signal-dependent spatial response was discovered and characterised, a phenomenon which agrees with the findings of other recent studies [36, 37].

5.2 SP-PTC Definition

The Single Pixel Photon Transfer Curve (SP-PTC) technique renders a 2D Region of Interest (ROI) over a full range of discrete signal levels, resulting in an illumination response detailing low-light, mid-range and fully-saturated pixel performance. From the same dataset, a standard PTC of the centre pixel only is also presented in order to investigate the shot-noise limited performance of the spot image. In an FF-PTC as detailed in Chapter 3, the shot noise regime of the PTC eventually gives way to the Fixed Pattern Noise slope of one as signal is increased. The onset of FF-PTC FPN usually occurs due to the differences in photo-response between pixels, dominating shot noise. In the instance where data is obtained from a single pixel, an absence of FPN and thus a purely shot-limited response could be expected, however; this is not the case as highlighted by the analyses in this chapter.

5.3 SP-PTC Acquisition

5.3.1 Initial SP-PTC Data

Figure 5.1 illustrates an SP-PTC, consisting of the per-pixel mean on a sample size of 200 frames per illumination level. The relative illumination of each tile is denoted in light units, where one light unit represents an arbitrary sub-millisecond exposure time. Each tile has a separate colour scale in order to accommodate the large range of signal levels. The mean signal of the centre pixel in ADU is given in each tile and utilised in plotting the signal to noise PTC data on logarithmic axes as in Figure 5.2.

While observing the trend of Figure 5.2, an FPN characteristic is shown throughout the entire signal range, prior to a drop-off at which point Full-Well Capacity (FWC)

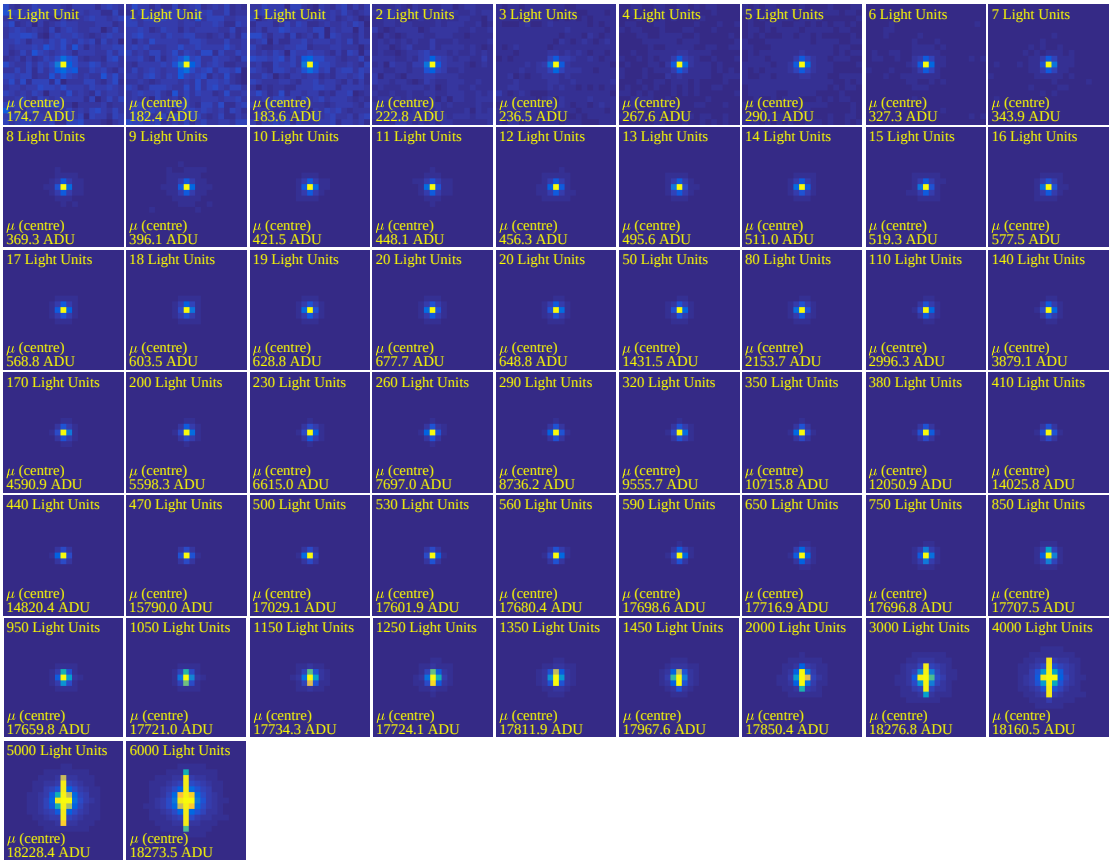

FIGURE 5.1: A 2D grid of ROIs illustrating the spot projection response including surrounding pixels for illuminations covering the full dynamic range of the CCD273. Data presented in the ROI mean on a per-pixel basis for 200 samples.

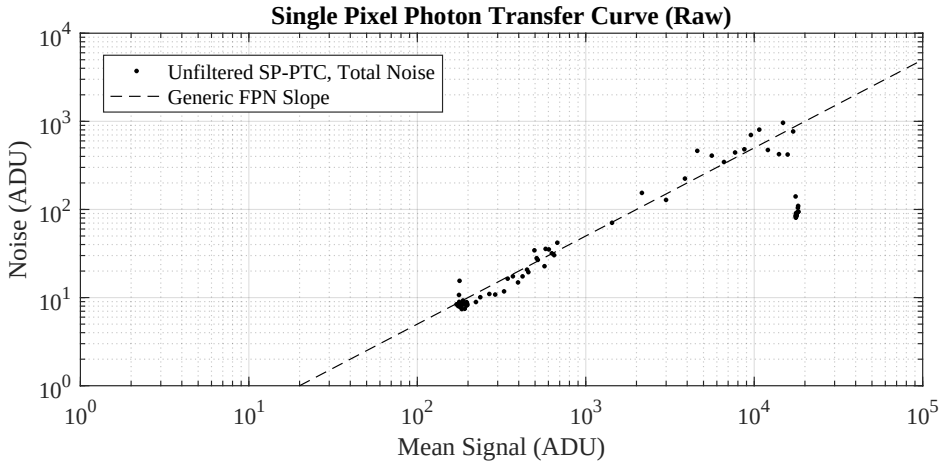

FIGURE 5.2: The spot centre pixel mean signal versus centre pixel noise for an unfiltered SP-PTC.

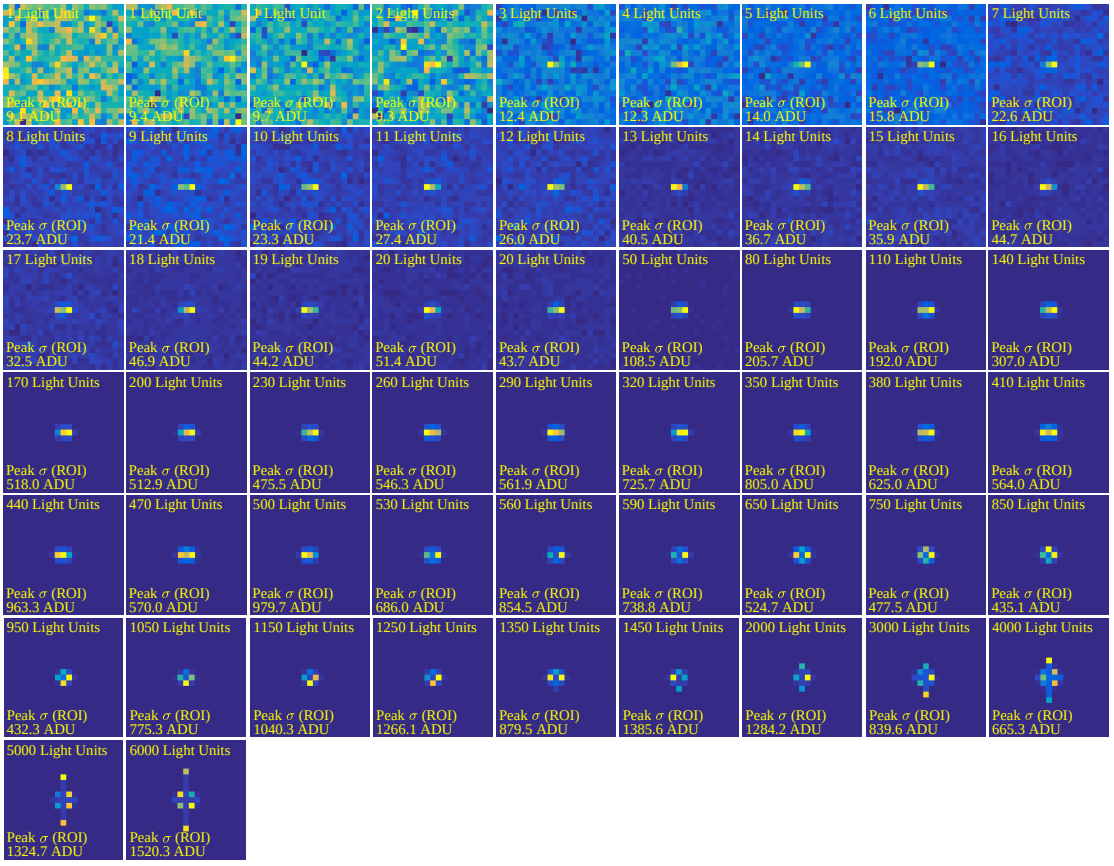

FIGURE 5.3: Partner SP-PTC to Figure 5.1, representing noise instead of mean signal on a per-pixel basis.

is reached. Such a departure from the hypothesised shot-limited performance indicates the presence of another fixed noise source. The possibility of vibrations within the spot projection system was investigated by using the SP-PTC format to plot noise on a pixel-by-pixel basis as in Figure 5.3. In this context "noise" is the standard deviation of each pixel for the population of images captured.

From visual inspection of the tiles of Figure 5.3, pixels horizontally peripheral to the centre pixel show higher noise than vertical neighbours. At low exposure times the centre pixel signal is almost indistinguishable from read out noise, while the mid-range exhibits consistent horizontal spreading and the progression to saturation sees a decrease in anisotropy through the onset of the blooming regime. In this context the "blooming

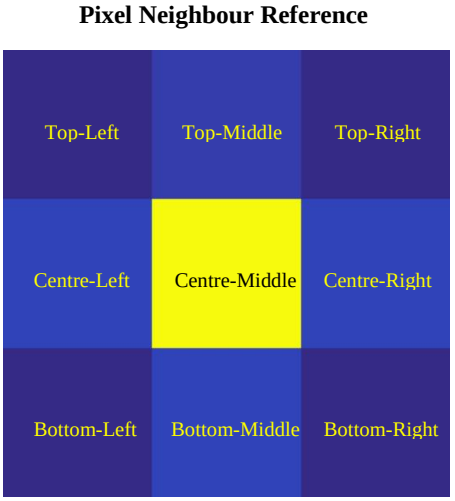

FIGURE 5.4: The 3 × 3 ROI containing the centre pixel of the projected spot, and 8 surrounding pixels. Individual pixels are labelled to support neighbour pixel analysis.

regime" is considered to be the point at which the charge is no longer contained within the centre pixel and begins to spread vertically, visible in this case from approximately 750 light units. The signal level at which considerable anisotropy occurs is characterised further, on a per-electrode basis in Chapter 7.

5.3.2 Neighbour Pixel Analysis: Unfiltered SP-PTC

Figure 5.4 labels the neighbour pixels in order for an analysis of ROI pixel response versus illumination level, as illustrated in Figure 5.5. From this data it is apparent that the orthogonal neighbours are not in agreement as they would be if the mean spot image was the result of a uniform, isotropic PSF. This development asks whether the illumination itself is in-fact uniform, however; as the dataset is the mean of a collection of 2D samples the averaging function could have a propensity to smear the spot image, resulting in anisotropy. Neighbour pixel analysis was developed in order to diagnose the origin of the anisotropy.

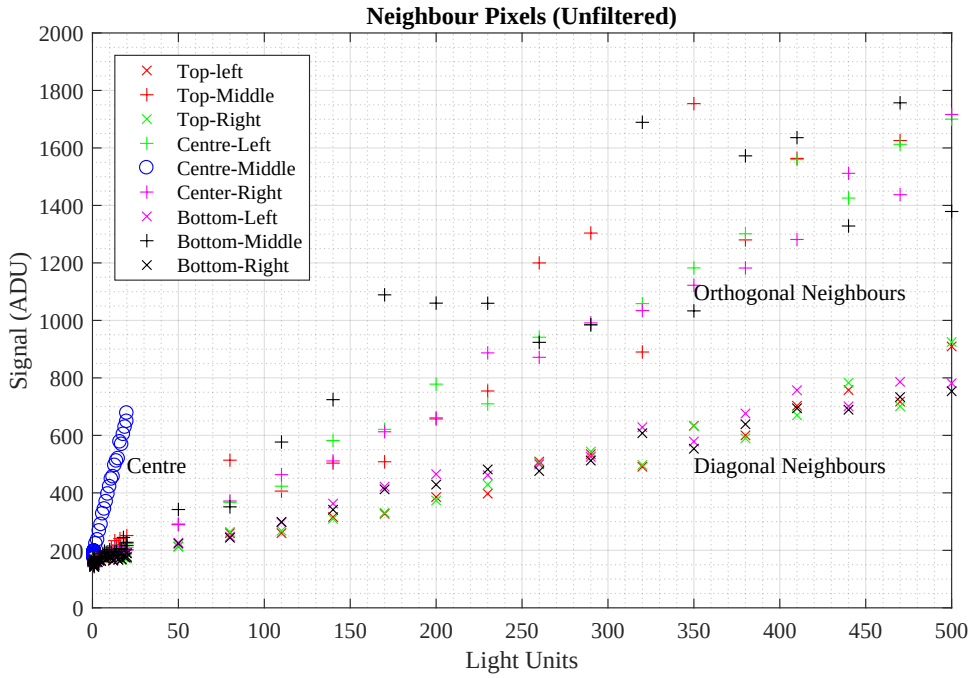

FIGURE 5.5: A plot of signal versus illumination level for the spot centre and peripheral eight pixels. Note the disagreement between orthogonal neighbours.

5.3.3 Diagnosing the Origin of FPN

To diagnose the origin of the unexpected anisotropy a centre of mass function was employed for each of the 200 individual samples, at a relatively mid-range level of illumination. The rationale behind the signal level choice is that a low illumination level frame is acquired faster than a high illumination level frame and therefore, with a millisecond-scale illumination duration the exposure time is limited to a fraction of the period of a low-frequency vibration. Another consideration is the signal to noise ratio: with a one Light Unit projection there is a small signal in relation to background level and therefore a centre of mass measurement is greatly susceptible to error introduced by read out noise.

Pictured in Figure 5.6 is a histogram acquired from all samples taken with 20 light units. The centre of mass is returned as Cartesian co-ordinates relative to the centre

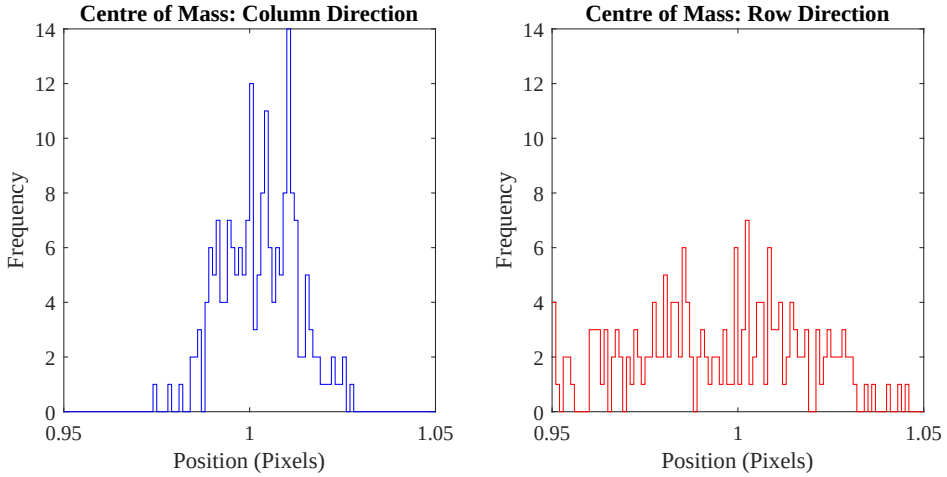

FIGURE 5.6: Centre of mass histogram taken from samples used to generate SP-PTC of Figure 5.1, [20 Light Units].

of the measurement ROI. In this instance a Gaussian-like distribution occurs in the column direction with a higher number of samples captured with the spot image over the vertical centre. In the row direction the distribution of centre of masses appears to be more stochastic in nature, implying a much greater travel of the spot image in the horizontal direction between the acquired frames. From this it was asserted that the FPN component seen in the SP-PTC measurements was the product of a mechanical vibration in the optical test bench, relative to the row direction of the device under test. This could be further confirmed by rotating the device 90 degrees and re-taking the data, while mechanical and time constraints made this impossible.

5.4 Improving the SP-PTC

5.4.1 A Lucky Imaging Analogy

The field of astronomy is full of ingenuity in terms of deriving results from challenging data sources. An example of such a concept is Lucky Imaging [38]: the process by which a vast amount of ground-based astronomical images are acquired and mostly discarded

in the search for frames devoid of atmospheric turbulence. The challenge faced here is analogous to the problem of acquiring a spot measurement in the presence of mechanical vibration. If the illumination period is low relative to the period of the vibration, a true smear-free response is achievable by only accepting and analysing frames containing a well-centred spot image.

The histogram of Figure 5.6 is important because it identifies the mode of vibration in the system while providing variables for quantifying the usefulness of each acquired sample to enable a better quality measurement. For instance, it is possible to generate a population of accepted frames for each light level based on a filter allowing only frames with a centre of mass within a specified error. This process forms the basis of processing SP-PTCs into filtered or "lucky-imaged" SP-PTCs.

5.4.2 Determining Filtering Constraints

The percentage of useful data in a dataset depends on the constraints applied, and in this case the constraints are varying numbers of acceptable samples on the centre of mass in the row and column directions. As the allowed deviation from the mean on the centre of mass is tightened, the number of available frames for analysis decreases. In order to investigate the impact of filtering tolerance on the dataset available for characterisation, Figure 5.7 was generated with a range of testing thresholds. The thresholds are enacted such that an example error threshold of $E_{Thresh} = 0.01$ pixels or a 1% positioning error accepts a frame with a centre of mass measurement in the range -0.005 to 0.005 pixels or $\pm 0.5 \times E_{Thresh}$.

The choice of centroid threshold is subject to a cost-benefit analysis. In reference to Figure 5.7, a 1% acceptable centre of mass decimates the available dataset, while a

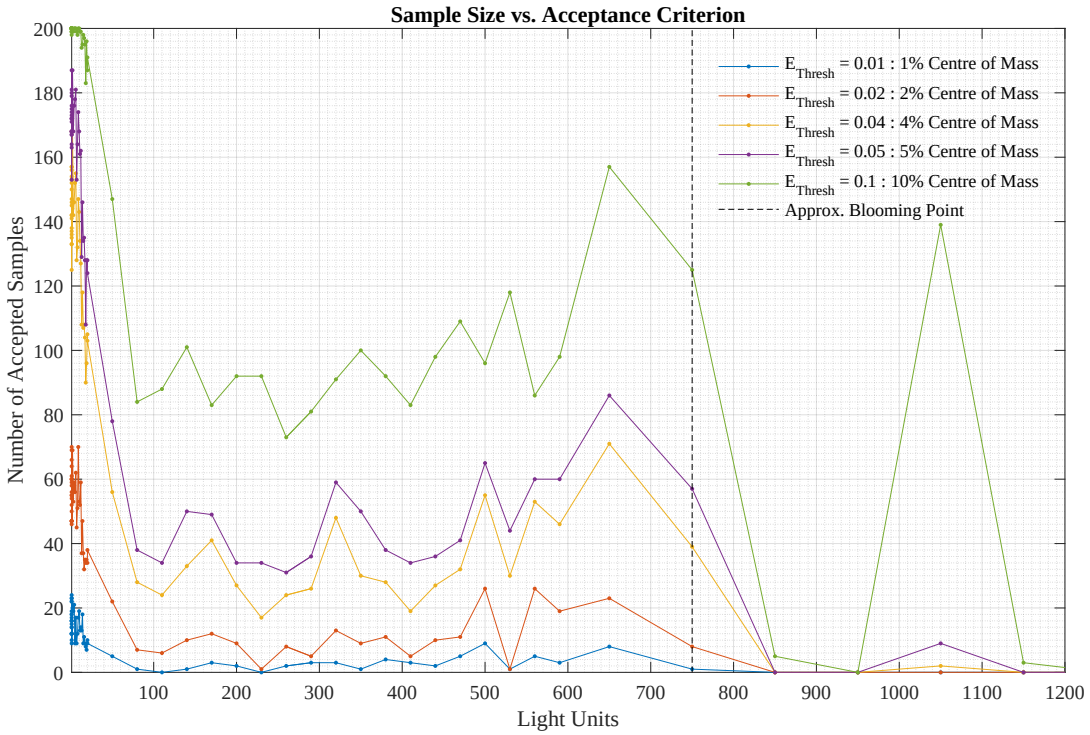

FIGURE 5.7: The number of accepted samples per illumination level for a range of centre of mass criteria.

2% threshold has a factor of three relative increase on data available for analysis. A 10% allowable centroid error accepts almost all frames gathered at low illumination levels, demonstrating that such a wide tolerance has little to no filtering effect. An increased dataset is attractive, while the chosen threshold is reflected in the error of the measured spot PSF. A 2% allowable centroid error threshold was selected as an acceptable compromise between error and sample availability.

5.4.3 Filtered SP-PTC Data

An example of spot response and noise before and after a 2% centre of mass filter is shown in Figure 5.8, with the benefit of matching colour axes. The appearance of horizontal smearing is noticeably reduced, preserving an isotropic spot image. Investigating the

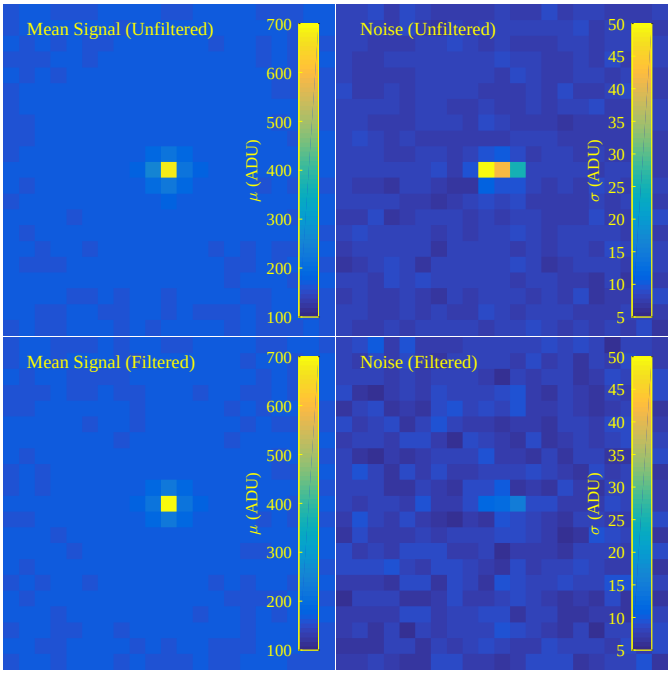

FIGURE 5.8: Example of pixel-by-pixel mean signal and noise from a 2% centre of mass filter (Top: Before filter, Bottom: After filter). Matching colour axes highlight the relative improvement in noise.

variance σ^2 in the centre pixel, the variance is cut by half to approximately equal the mean signal, indicating that the behaviour has returned to within Poissonian bounds.

Figure 5.9 updates the unfiltered Figure 5.2 with SP-PTC tiles averaged on a pixel-by-pixel basis from a reduced dataset with 2% centroid constraints. Some illumination levels lack any data compliant with the filter criterion, thus an average image is unavailable in those instances. This is likely attributable to levels of horizontal smearing permitted by longer exposure times at higher illumination levels. An updated centre pixel signal-to-noise characteristic, juxtaposed against the original unfiltered trend is shown on logarithmic axes in Figure 5.10.

The improvement in noise performance is notable by the absence of an FPN slope from low to mid-range signal levels, confirming the efficacy of the centre of mass filter. A noise slope of a half in relation to mean signal is indicative of a regime where noise is proportional to the square root of the arrival rate of photons [39, p. 101]. Figure 5.11

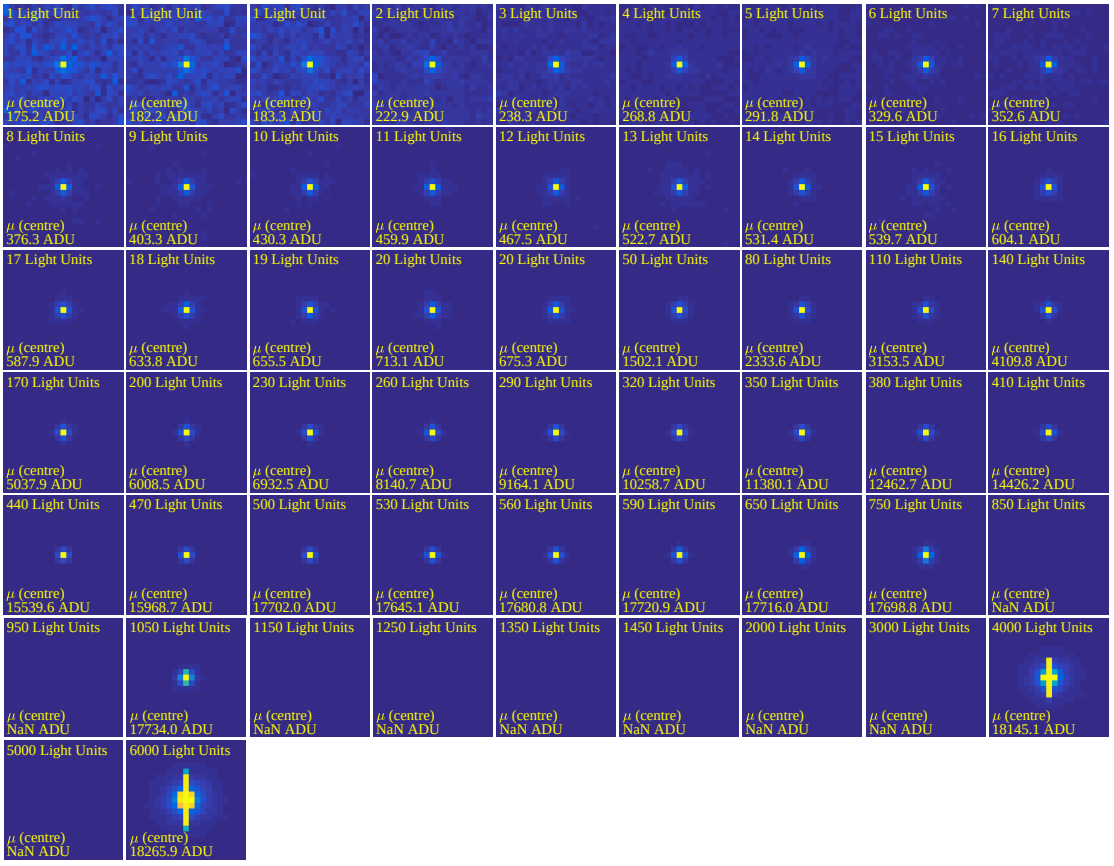

FIGURE 5.9: SP-PTC tiles illustrating the pixel-by-pixel mean signal of the centre pixel and periphery with 2% centre of mass filter applied.

shows a variable reduction in ROI peak noise when compared to unfiltered precursor, Figure 5.3. Euclid VIS shape measurements are to be conducted in the small to mid signal range as brightness of detected objects is limited by inherent anisotropy of CCD blooming. The shot-limited signal range of filtered measurements is therefore suitable for further analyses in context of the VIS instrument.

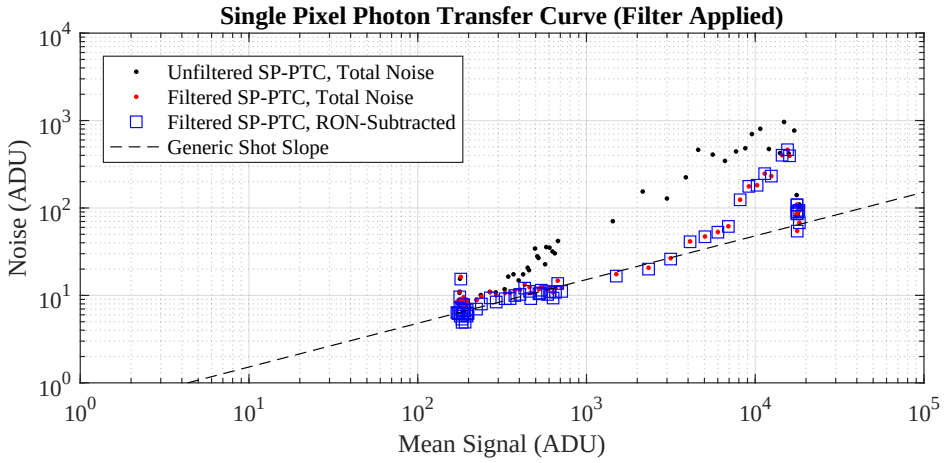

FIGURE 5.10: Logarithmic SP-PTC illustrting the signal to noise characteristics of the centre pixel with 2% centre of mass filter applied.

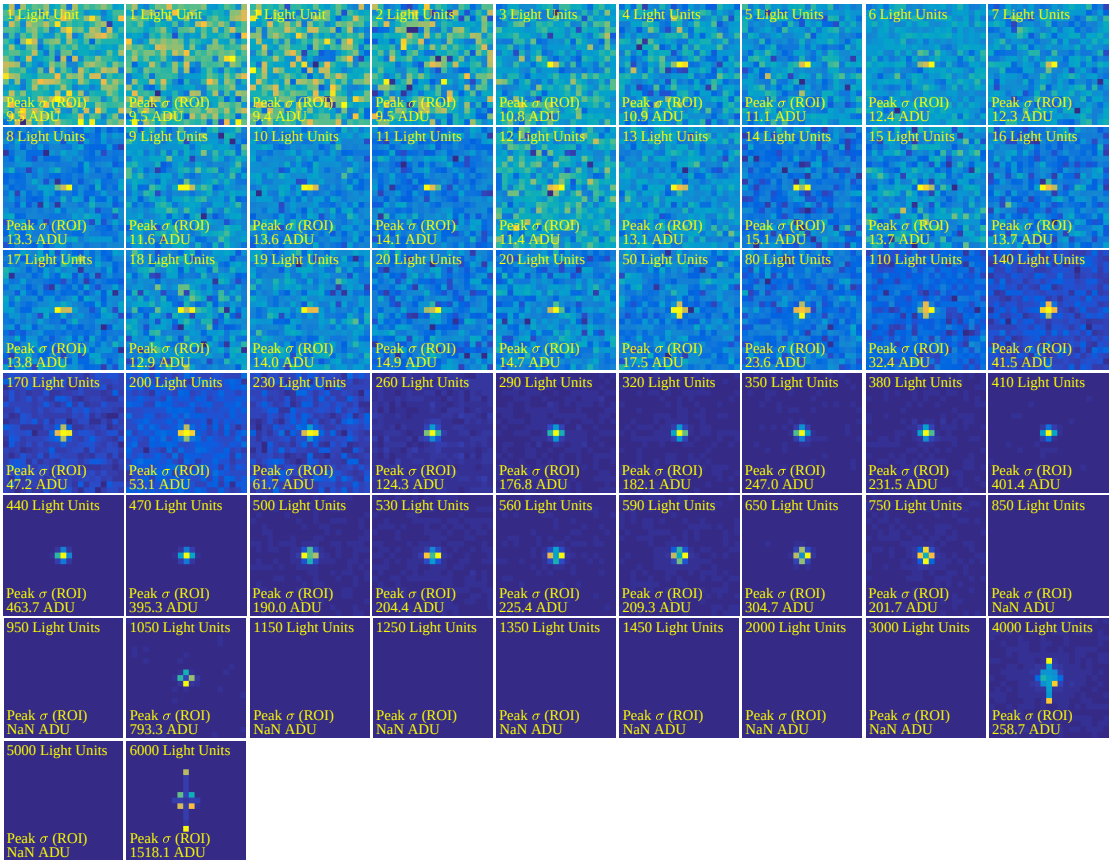

FIGURE 5.11: SP-PTC tiles illustrating the pixel-by-pixel noise of the centre pixel and periphery with 2% centre of mass filter applied.

5.4.4 Neighbour Pixel Analysis: Filtered SP-PTC

In contrast to Figure 5.5, the neighbour pixel analysis of Figure 5.12 shows a good agreement between orthogonal neighbours in the small-signal to mid-signal illumination range. This figure further corroborates evidence indicating a near-isotropic spot response from the filtered data.

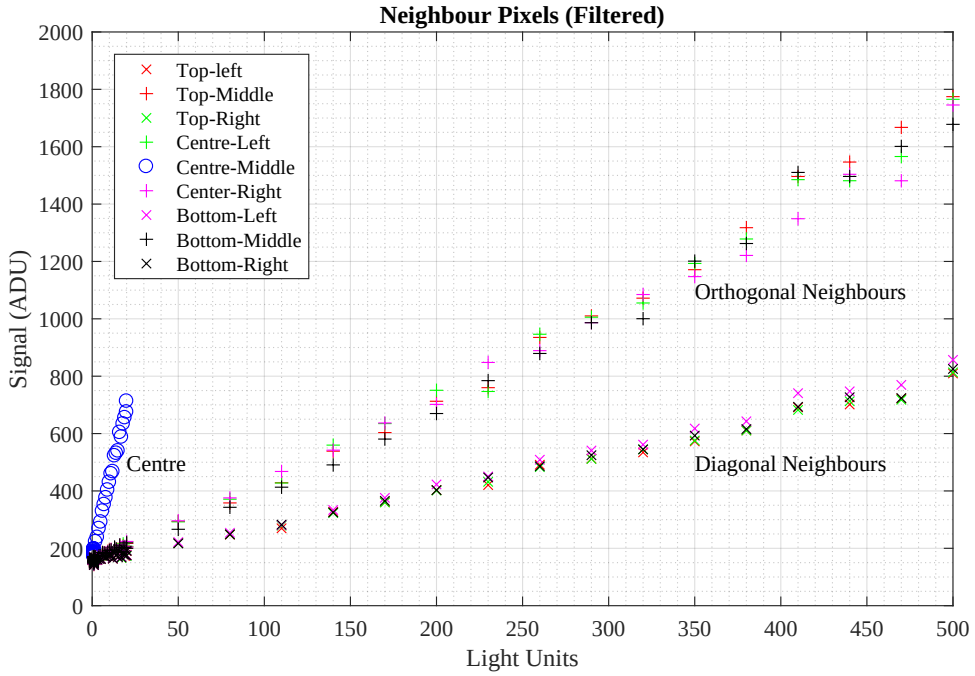

FIGURE 5.12: Spot filtering example showing improvement of aspect ratio at a high signal.

5.5 Aspect Ratio Analysis

The purpose of this section is in order to investigate the spot behaviour in the column and row direction by developing a system to compare the charge population in each direction around the spot.

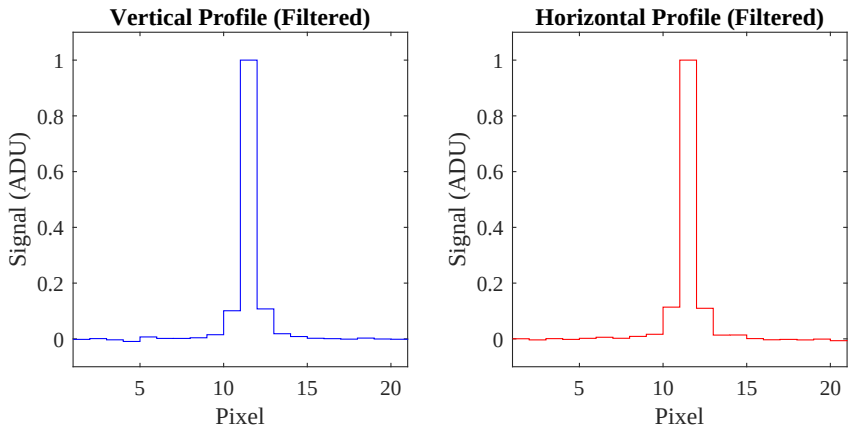

FIGURE 5.13: Vertical and horizontal slices through the spot response ROI, post 2% centre of mass filtering.

5.5.1 Definition of Aspect Ratio

Aspect Ratio (AR) is the quotient of the horizontal and vertical dimensions of a rectangular surface or grid, such as a 16:9 television set, however; in the context of this study the term has been borrowed as a dimensionless figure of merit when considering the spreading direction of charge in a spot illumination response. In a CCD the charge collection behaviour is generally believed to be without horizontal or vertical preference, with the exception of the response close to or beyond the blooming threshold. The AR in the context of this study is the ratio of charge in the spot ROI horizontal direction divided by the charge in the spot ROI vertical direction, with the omission of the centre pixel charge. For use as an example, Figure 5.13 illustrates vertical and horizontal slices through a normalised background-subtracted SP-PTC tile for a mid-range illumination. The AR in this case is a ratio of the sum of each element of the two line profiles.

5.5.2 Aspect Ratio Measurement

Figure 5.14 shows the spot AR with respect to both illumination level and centre-pixel signal. This plot is of value in the respect that it confirms that there is an isotropic

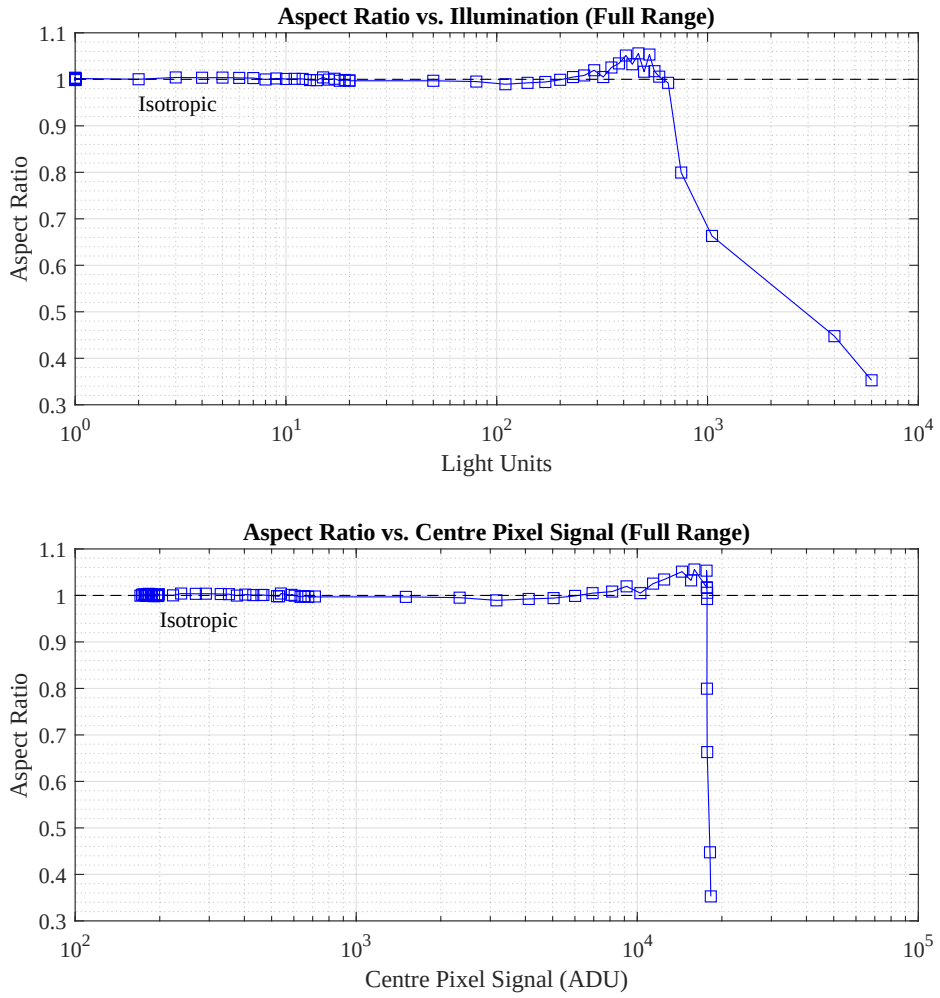

FIGURE 5.14: Plot of spot aspect ratio versus signal and illumination level. Light Units are relative units of integration time.

charge collection behaviour for the majority of the signal range, prior to the blooming threshold. In the context of a CCD, the blooming threshold is the point at which the potential well can no longer contain the charge accumulated as it has become too high. The charge exceeds the "barrier" potential presented by the inactive electrode phases and spills into adjacent pixels up and down the column. This behaviour and the effect of image clock voltage level is investigated during optimisation in Chapter 7.

When the blooming threshold is exceeded the centre pixel signal cannot increase beyond

full-well capacity, thus the lower of the two figures features a steep fall-off. In the upper plot there is different behaviour with respect to illumination level as the x-axis is not constrained by full-well capacity in this case. The two sub-figures are presented together with the purpose of illustrating the disconnect between illumination level and reported signal, at higher signal levels.

The excursion into positive aspect ratio, prior to vertical blooming is likely to be an artefact of increased exposure times allowing horizontal smearing which results in an AR > 1. The points shown in the flat isotropic regime covering low-mid signal range show that the aspect ratio percentage change does not exceed the 2% centre of mass criterion enforced by the spot filtering, further confirming the suitability of the dataset for making PSF measurements with respect to signal. With symmetry established in the signal range of interest, it is possible to progress to characterising the spot Full-Width at Half-Maximum (FHWM) as in Section 5.6.

5.6 Signal Dependent Spot FWHM

5.6.1 Definition

With visual inspection of the pictorial SP-PTCs of Section 5.3 it was suspected that the spot response becomes wider with signal. Having ascertained that the PSF ROI row vs. column aspect ratio remains approximately unity for the majority of the signal range in Section 5.5, the same dataset is utilised in addition to the Gaussian fit procedure of Section 4.2.3 in order to investigate the signal-dependent spot FWHM.

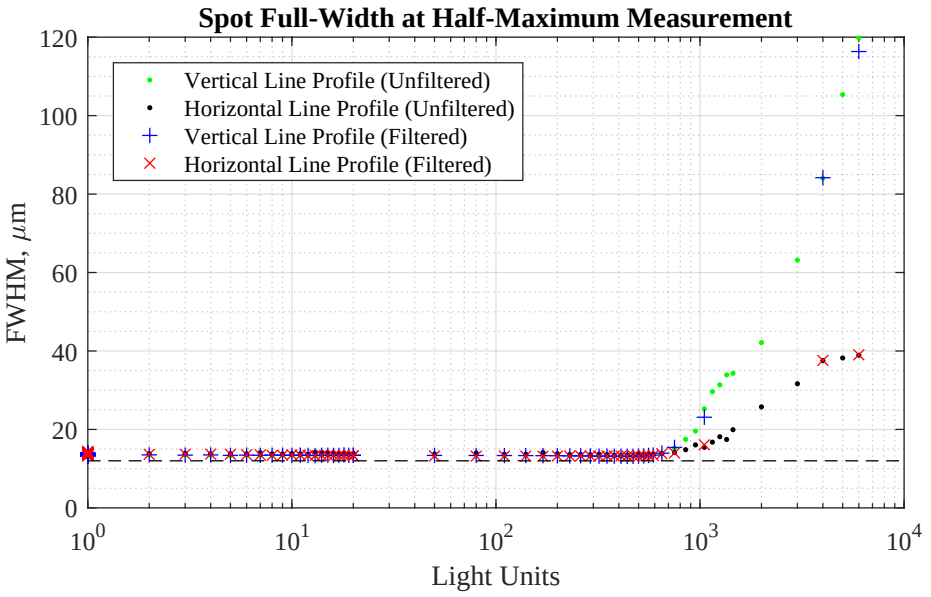

FIGURE 5.15: Full-width at half-maximum values of the spot for both filtered and un-filtered cases over a range of integration times. The dashed line represents the 12 µm pixel pitch.

5.6.2 FWHM Analysis

Figure 5.15 illustrates the stability of the FWHM in the vertical and horizontal directions for conditions with or without the centre of mass filtering of Section 5.4. The onset of blooming is noticeable from around 1000 Light Units with horizontal charge spilling mitigated to a FWHM of approximately 40 µm, while the vertical blooming continues with the increase in exposure as charge spills in the column direction.

Taking the same dataset and plotting the horizontal FWHM vs the vertical FWHM yields a spatial spot aspect ratio measurement (instead of a ratio of ROI signal in the horizontal and vertical direction, as before in Figure 5.14). Figure 5.16 illustrates the FWHM aspect ratio versus signal in electrons. Values in electrons were generated by multiplying data with the conversion gain (13.1 e/ADU) obtained using the photon transfer curve technique of Section 3.4. The low-signal range of the figure exhibits a fair amount of noise, while the mid-range shows a clear change in the FWHM aspect ratio

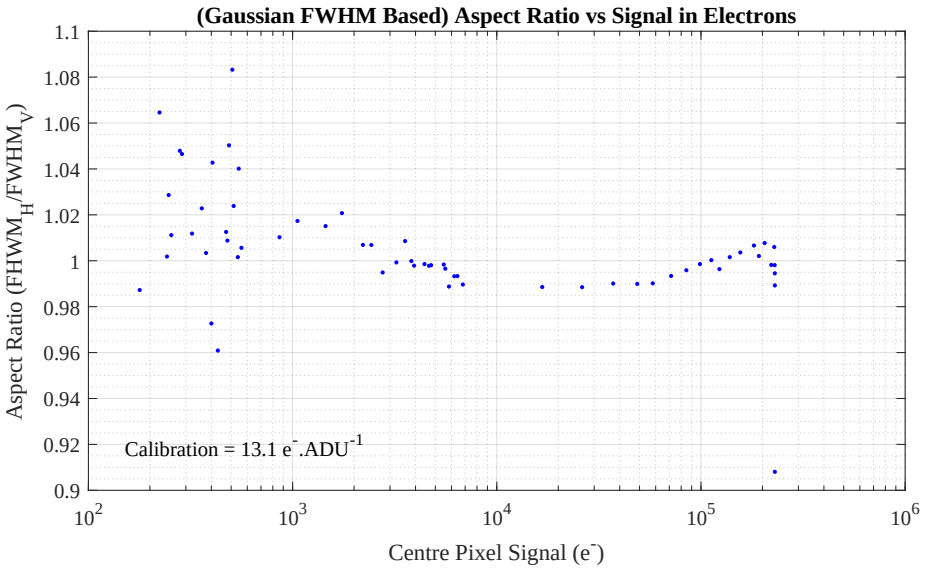

FIGURE 5.16: From the data in Figure 5.15, the FWHM-based aspect ratio is plotted versus signal converted to electrons using the conversion gain. Here the blooming threshold is approximated to be 2.3×10^5 electrons.

until the system reaches full well capacity and the spot blooms up the column. What is remarkable in this case is that it appears that the spot changes shape with respect to signal level - a phenomenon which is properly named and investigated in the next chapter.

5.7 Summary

In this chapter a novel analytical technique is introduced - the Single-Pixel Photon Transfer Curve. In the presence of vibration, a filtering technique was designed and implemented in order to mitigate the blurring of the spot image. In the process of analysing spot images versus signal, it became apparent that by fitting a Gaussian FWHM to each filtered signal level, there is a change in the ratio of the spot FWHM in the column and the row direction. This implies a signal-dependent PSF response of the detector and it is of a magnitude (2% full swing over the 1 ke to 200 ke signal range of

Figure 5.16), such that it is highly relevant to the optimisation of the Euclid telescope conducting a weak gravitational lensing survey.

The Aspect Ratio (AR) measurement of Section 5.5 has since been utilised in the study *"Comparison of Point Spread Function in p- and n-Channel CCDs"* by Murray. N. J. and Allanwood. E. A. H. et. al [40]. In the Murray paper, the AR is used as a figure of merit in investigating the PSF-specific spatial performance of the p-channel and n-channel variants of the CCD204 - a structurally identical test device to the CCD273 under investigation in this thesis.

Chapter 6

Investigating the Brighter-Fatter Effect

6.1 Introduction

The initial results of this chapter are published in the SPIE paper *"Point-spread function and photon transfer of a CCD for space-based astronomy"* (Allanwood et. al., 2013) [41]. In the paper the SP-PTC method is discussed alongside laboratory methods used in order to try to detect a phenomenon which as of 2014 was coined: *The Brighter-Fatter Effect* (BFE) [37].

In this chapter there is firstly a review of pertinent background information, followed by a selection of experiments aimed at investigating the BFE, or in lay terms - observing the signal-dependent widening of spot images and examining the probable cause.

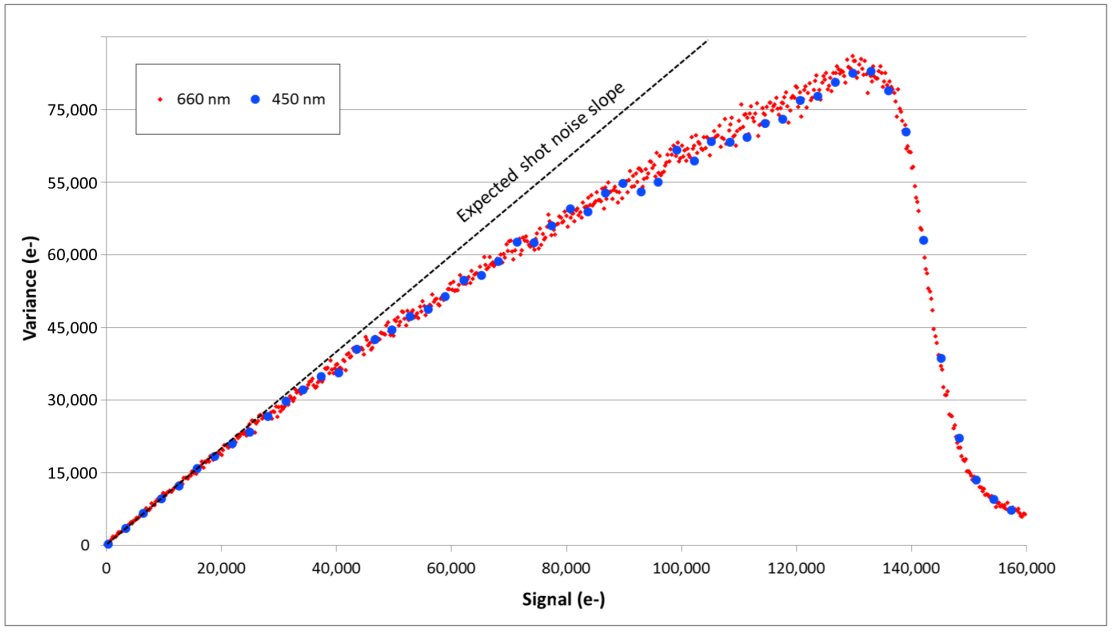

FIGURE 6.1: A mean-variance curve acquired with a back-illuminated CCD204 where as signal increases, the variance "flattens out". Extract from Murray, N. J., Allanwood, E. A. H., et. al. [40]

6.2 The Brighter-Fatter Effect

Recall Section 3.4.4 in which the slope of a Mean-Variance (MV) curve is observed in order to corroborate the calibration obtained by a Photon Transfer Curve (PTC). In some cases the MV curve prematurely rolls over with increased signal as in Figure 6.1, indicating that the process becomes sub-Poissonian [42], and the slope of the MV is not a reliable indication of conversion gain. Downing et. al. [36] explore this phenomenon in their 2006 paper appropriately titled *"CCD riddle: a) signal vs time: linear; b) signal vs variance: non-linear"*. They conclude that while signal is proportional to illumination time, shot noise does not increase linearly with signal and that the mechanism behind the non-linear noise performance is possibly due to charge *sharing* between adjacent pixels. The claim of a charge sharing mechanism is supported by their experiment in which the correlation between neighbouring pixels is measured under flat-field illuminated conditions. In their 2013 follow-up paper *"The CCD riddle revisited: Signal versus Time*

- *Linear, Signal versus Variance - Non-linear"* [43], Downing et. al. publish their conclusion that existing charge in one pixel reduces its competitiveness with its neighbours for charge collection, hence the widening of a spot image with greater signal.

A method to derive an accurate device-wide conversion gain in the presence of MV PTC non-linearity is commonly referred to as the Pain-Hancock technique [44]. While the Pain-Hancock method is useful for correcting for an apparent signal-dependent conversion gain, it is no remedy for the spatial effects of pixels affecting their neighbours. This was addressed by Antilogous et. al. [37], where they relate the inter-pixel flat-field spatial correlation work of Downing et. al. to the ability to predict the extent of the spot widening with respect to illumination level. The desired end-game of such studies is that the signal processing pipelines of telescopes such as Euclid and LSST can be improved so as to better conform with their strict galaxy shape measurement requirements of 1% and 0.1% accuracy, respectively [4, 45].

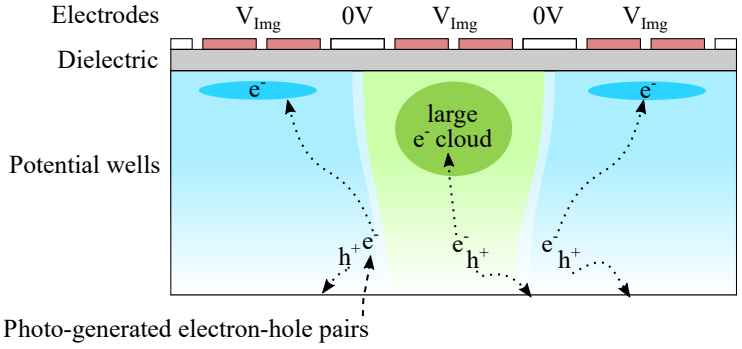

FIGURE 6.2: A cartoon representation of the Brighter-Fatter Effect based on the simulation work by Weatherill and Downing [43, 46], illustrating the diminished influence of the electric field of the pixel occupied by the highest charge. The boundaries shown are not to be considered as an illustration of the electric field, but as a shift in pixel boundary caused by the reduced centre-pixel electric field.

At the time of writing, the BFE is characterised and widely understood for the issues that it presents by the astronomical imaging community, however; at the time of experimentation the mechanism by which spot images become broader with signal was subject to speculation. Within the Centre for Electronic Imaging there were multiple theories

regarding the charge-collection behaviour with suggestions such as charge migration between pixels, however these never gained traction. The most cogent idea was that of a variation in electric field caused by photo-generated charge occupancy. For example: in a pixel with high signal, the electric field strength is weaker than neighbouring pixels with lower signal, therefore e-h pairs generated near pixel boundaries are likely to drift into neighbours, as demonstrated by an artistic drawing in Figure 6.2. In 2016 Weatherill [46] presented a Ph.D. thesis based on the modelling and experimental verification of the shift in pixel boundaries relating to charge collection behaviour.

6.3 Multiple Illumination Experiment

In this section a new method is described for observing the mechanism of the Brighter-Fatter Effect. The concept is described in Section 6.3.1, followed by the methodology and experimental analysis in Sections 6.3.2 and 6.3.3, respectively.

6.3.1 Concept

In order to introduce the concept of the *Multiple Illumination Experiment*, first consider a thought experiment where two images are acquired by a CCD. In the first image there is a lone spot projection, while in the second image there is a spot projection, immediately followed by a flat field illumination prior to readout. In an ideal CCD with perfect linearity you would expect the difference between the second image and the first image to render a flat field, however; in the instance where the BFE occurs - the reduced influence of the centre pixel electric field caused by the spot signal could allow some of the flat field signal to be collected in the spot periphery. The ideal and BFE-affected CCD responses to this experiment are illustrated in the cartoons of Figure 6.3 and Figure 6.4, respectively.

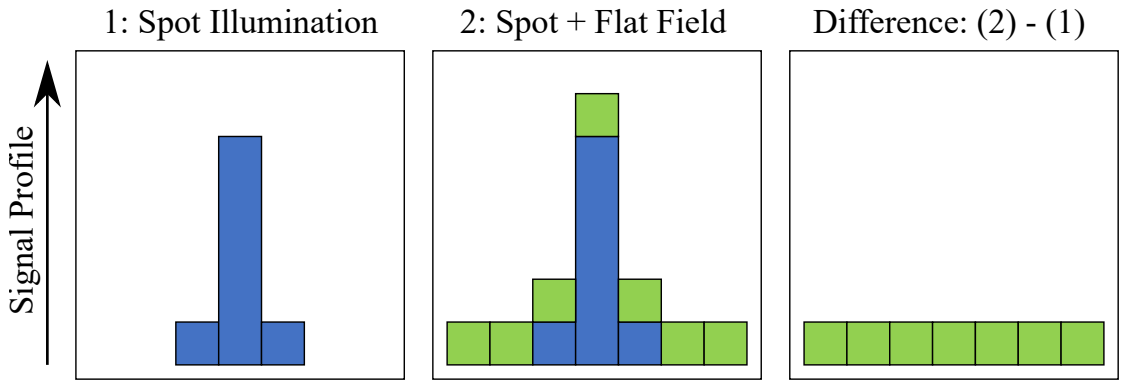

FIGURE 6.3: Line profile of frames with multiple illuminations and an ideal difference between the signal in the two.

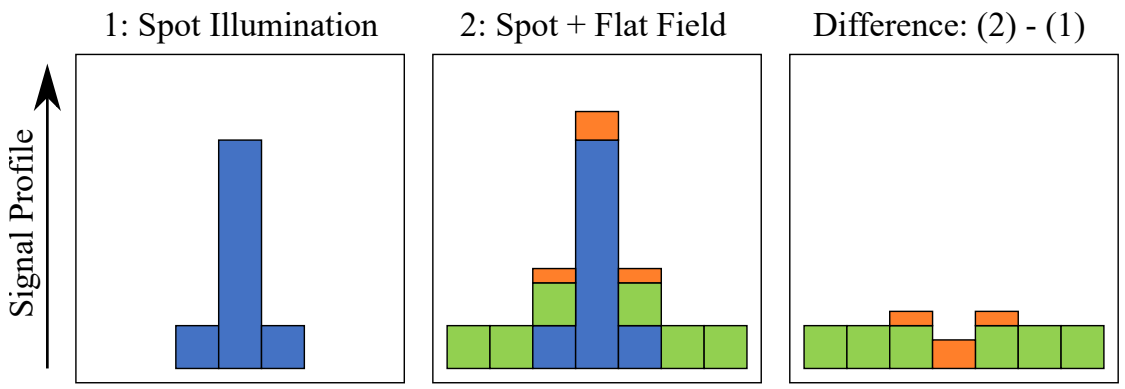

FIGURE 6.4: Line profiles as in Figure 6.3, however; the BFE has caused a different distribution of photo-generated charge in (2), resulting in a distorted difference image.

6.3.2 Methodology

Figure 6.5 illustrates images taken in sequence, with dark buffer frames in between to reduce the possibility of any persistence between frames. The first image features only a spot illumination (Frame 1), followed by an image featuring only a flat-field illumination (Frame 2), followed by a final image (Frame 3) featuring a spot illumination, shortly followed by a flat-field, prior to image readout. In this experiment the effect of dark current is considered to be negligible as it was conducted at -110°C, with sub 1 second frame integration times.

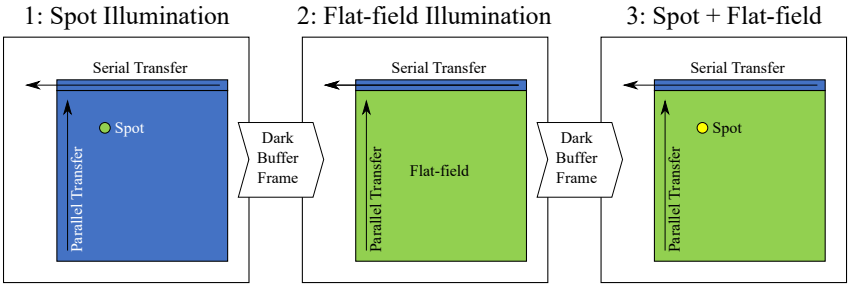

FIGURE 6.5: CCD readout scheme for multiple illuminations, including buffer frames to mitigate any persistence between frames.

A requirement of this experiment is that the output of the CCD has to be assumed to be perfectly linear to allow subtraction and analysis of image components and this is never the case. The output amplifier non-linearity is measured and a transfer function for

linearising data is generated in Section 7.5, *Systematic Non-linearity*, within the chapter *Optimising the CCD273*. To summarise, the transfer function works in such a way that for each value in ADC counts, an array or look-up table of 2^{16} values is available by which to output a corrected response.

The exposure times were adjusted such that the summation of peak spot signal and peak flat-field signal would be comfortably below full-well capacity. Figure 6.6 plots flat-field signal versus peak spot signal for each of the permutations recorded by the experiment.

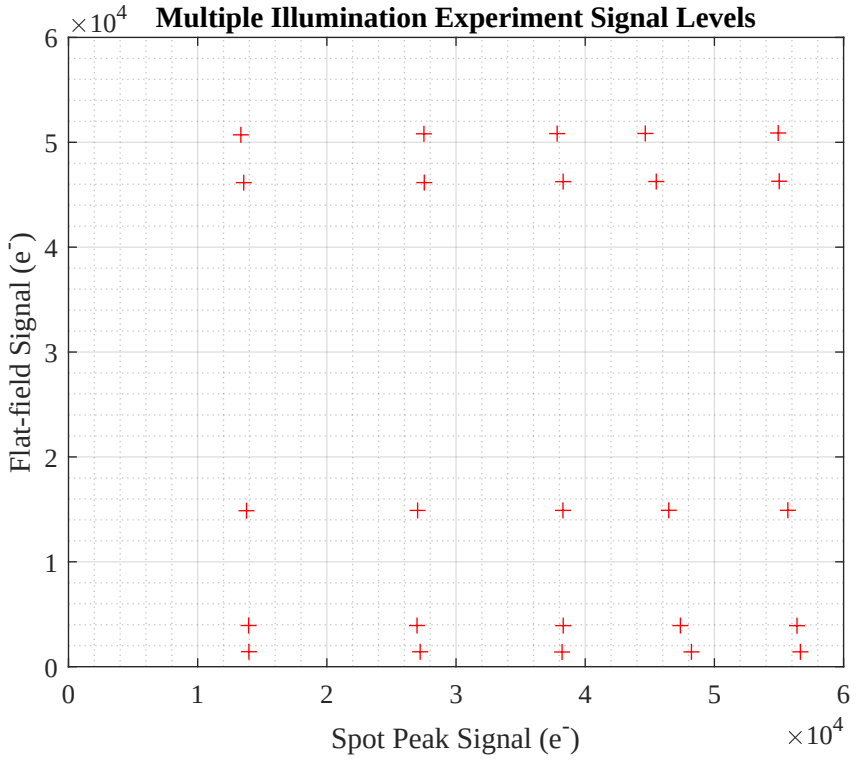

FIGURE 6.6: The peak spot and flat field signal levels utilised for the *Multiple Illumination Experiment*.

6.3.3 Experimental Analysis

To analyse the spot shape with and without an additional flat-field illumination applied, the flat-level offset was subtracted by finding the minima of the flat-field free line profile signal in each ROI. Figure 6.7 plots the vertical and horizontal line profiles for the spot

image for the spot only and the spot, followed by a flat-field. Error shown accounts for the noise on 100 source frames in each case. Recalling the BFE theory of 6.3.1, it is hypothesised that in the presence of an existing centre pixel charge population, an increase in the 8-pixel spot periphery signal is expected, due to the decreased electric field influence of the centre pixel.

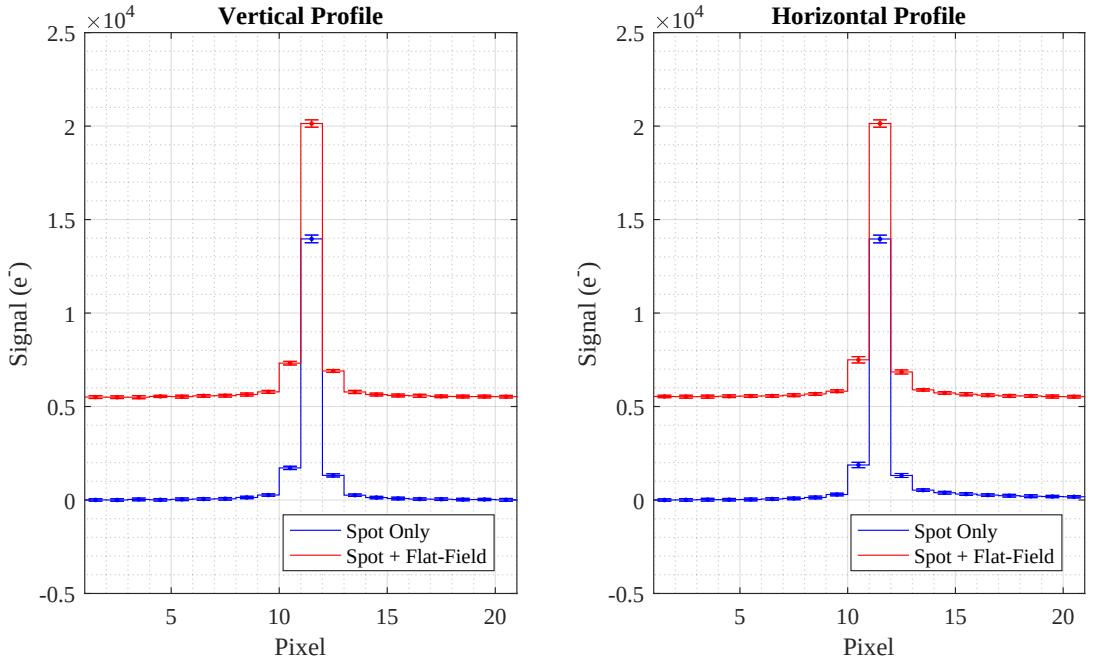

FIGURE 6.7: Mean vertical and horizontal line profiles through the spot for the spot and spot with flat field images for the case study.

In order to determine if this is the case and the BFE is in action, the centre pixel signal and the periphery signal will be examined for each level of spot signal and applied flat-field signal. Figure 6.8 illustrates the same data as Figure 6.7, with the flat-field level offset subtracted from the spot plus flat field profile: this allows a juxtaposition of profiles, illustrating that in the case of a 14 ke^- spot with a 1.3 ke^- flat field, any increase in the peripheral two pixels in the vertical and horizontal is obscured by noise, and the centre-pixel increase in signal accounts for the 1.3 ke^- increase. Therefore it is shown that a spot of approximately 10% of full-well capacity behaves ideally when

exposed to a small 1.3 ke^- flat-field.

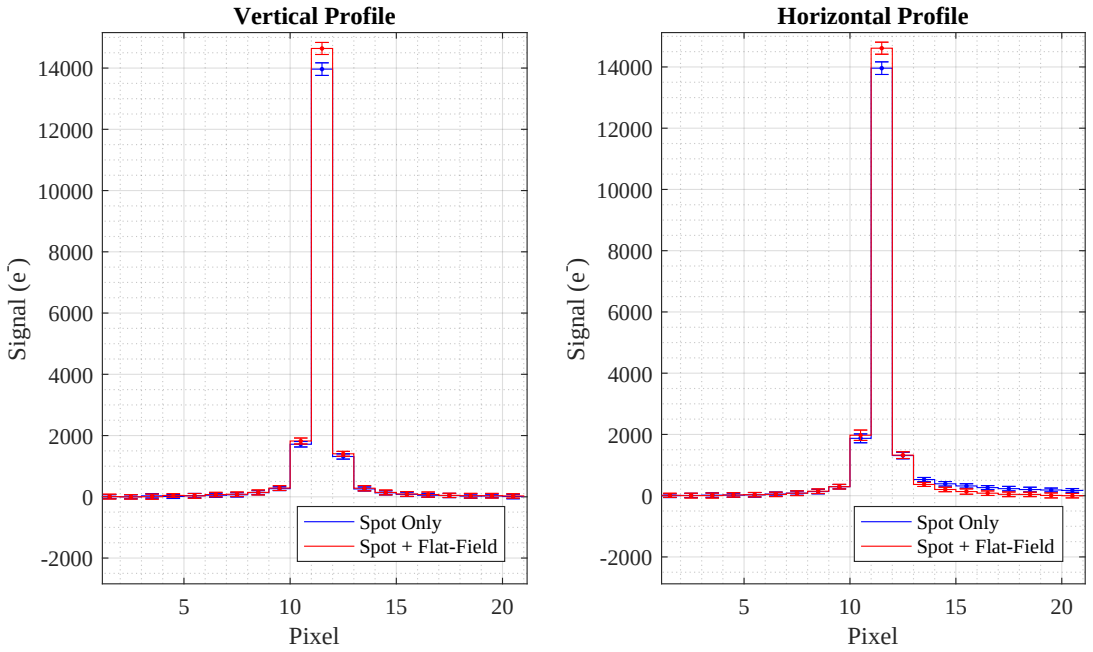

FIGURE 6.8: Mean vertical and horizontal line profiles through the spot for the spot and spot with flat field images for the case study. Offset adjusted for flat-field illumination increase.

Figure 6.9 illustrates an example with a 55 ke^- spot and 46 ke^- flat-field, where the flat-field offset-adjusted spot image is lower in centre pixel signal than the spot only image, with a discernible increase shown in the peripheral pixels. This agrees with the hypothesis and accounts for an approximate 3% redistribution as an effect of the charge collection behaviour. By differencing the mean spot-only and spot plus flat-field images for each spot and flat-field signal measured, Figure 6.10 is generated.

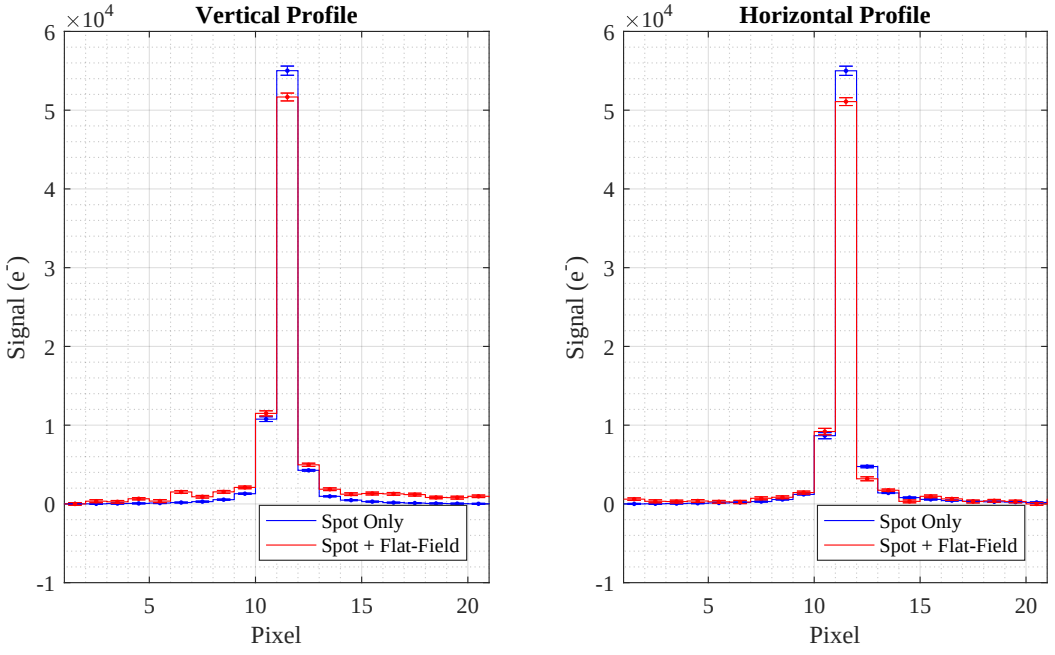

FIGURE 6.9: In the above example, the offset-adjusted centre pixel signal has decreased, while in the vertical profile the peripheral pixels have increased - and the increase is discernible from noise.

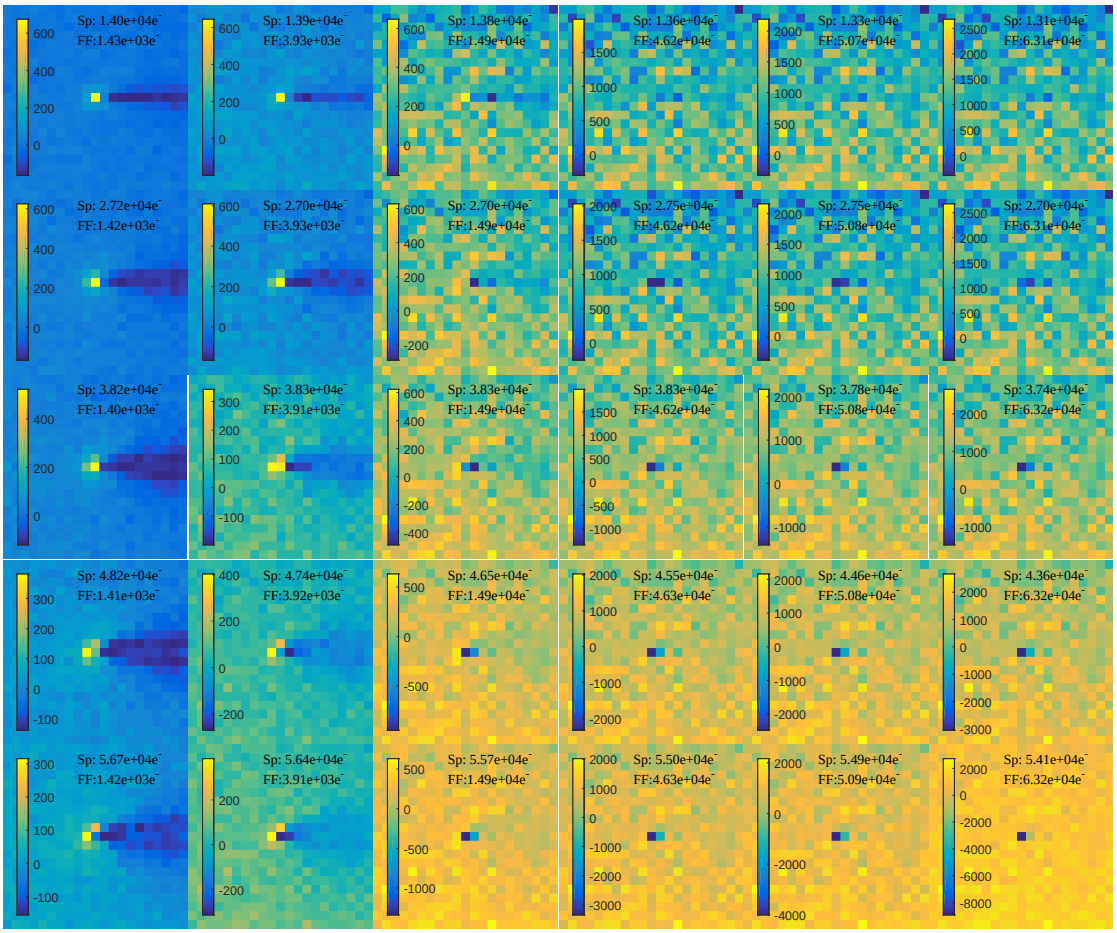

FIGURE 6.10: Difference images for each combination of spot and flat field signal level. The spot (Sp) and flat-field (FF) recorded signal levels are indicated for each tile. Spot signal increases between tiles from top to bottom, while flat-field signal increase between tiles from left to right. Different colour axes with values in electrons are used for each tile in order to ensure interesting features are not obscured.

From visual inspection it is clear that there is some interesting artefacting in some cases regarding the negative swing of pixels following the spot in the serial (horizontal) direction, which may be attributed to an uncharacterised systematic error or transient behaviour of the output circuitry. As the flat-field illumination is increased the difference of the centre pixel becomes more prominent, especially so when there is a large pre-existing charge within the centre pixel.

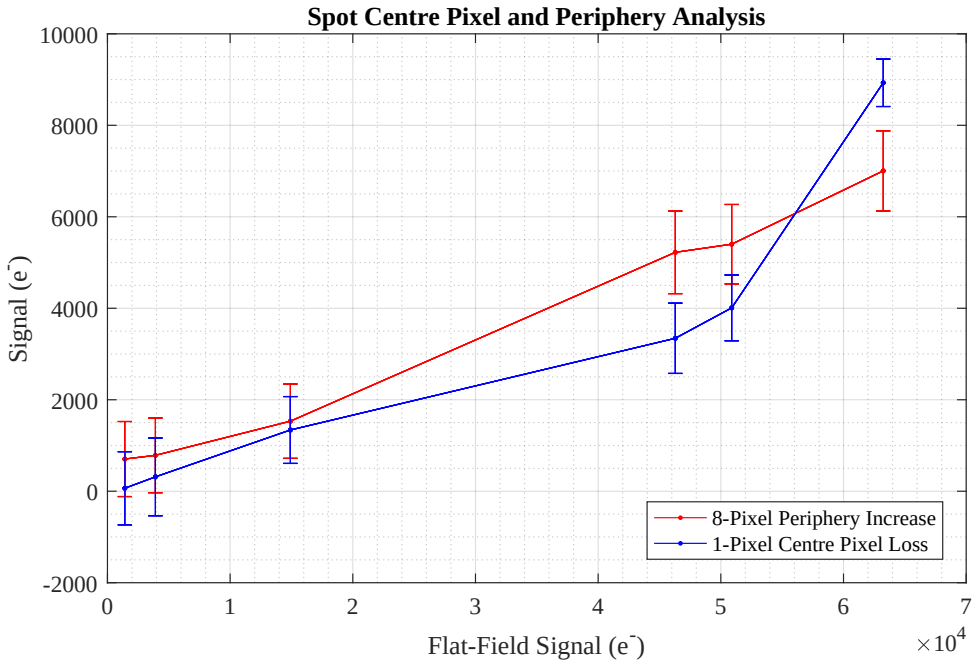

FIGURE 6.11: A side-by-side comparison of signal gained in the periphery compared to lack of signal attracted to the centre pixel.

Now focusing on the particular case study of Figure 6.9, we look at the brightest spot projected at 55 ke^- and the centre pixel signal *loss* with flat-field exposure is compared to the signal *increase* of the peripheral eight pixels in Figure 6.11. The side-by-side comparison shows a convincing relationship between flat-field signal and the shift of charge collection in the centre pixel, to the 8-pixel periphery. The use of the eight peripheral pixels as a region of interest for tracking charge increase outside the central pixel may be limited at higher signals. From observation of Figures 6.10 and 6.11, a disagreement occurs at a flat-field signal level of 4.6 ke (Periphery increase, greater than loss) , and much more noticeably at 6.3ke (loss much greater than periphery increase). These behaviours may be attributed to wider redistribution of collected charge than is monitored by the peripheral region of interest, or perhaps undiagnosed systematic error.

6.4 Electrostatic Influence

6.4.1 Concept

In order to investigate the role of electrostatics the spot behaviour is characterised here in relation to the applied electrode biases, or image clock voltages in imaging nomenclature. The image clock voltage was varied in one volt steps from 7V to 11V, values which are around the CCD273 default of 8V. A spot of high, but comfortably sub-blooming level signal was focused onto a region of interest and a hundred images were recorded for each image clock voltage setting. The spot was not re-focused between steps and images were recorded using a windowed sequencer: two measures taken to minimise the acquisition time and potential for any electrical, thermal or mechanical drift which could adversely affect the validity of measurements. A wider spot than usual (¡ 30 µm) was used in order for there to be a higher signal level in the centre periphery for the purpose of Gaussian fits.

Due to the windowed sequencer approach, there was an absence of an over-scan region by which to subtract an image offset. Offset subtraction is the process in which the zero-signal output by the ADC is removed, in this case in the order of 3000 ADU is subtracted, leaving the signal only. This process is usually conducted by subtracting the over-scan region: an area of the image readout formed when a number of serial transfers greater than the length of the serial register is performed. Note that this process is usually just subtracting a single integer from the entire image readout, which is applicable for many applications. In the interest of this application, the variation column-by-column dark response was particularly evident after offset subtractions due to a phenomenon known as “CDS ripple” where the serial register has a slight oscillation in offset level across the columns.

In order to correct for columnar fluctuations, ten rows succeeding the spot image toward to the bottom of the ROI in the column direction were used to correct the image zero level. Figure 6.12 details this process and the perceived accuracy of the generated offset image as a percentage of the acquired raw ROI image. The mean of a ROI of columns beyond the spot image is utilised because the variation in electrical offset across the ROI is column-dominated and not row dominated. This "ripple" effect occurs on every row and is thought to be an artefact of the proximity of the ROI to the output node in relation to the transient behaviour of the external camera electronics ADC when a new row readout is started.

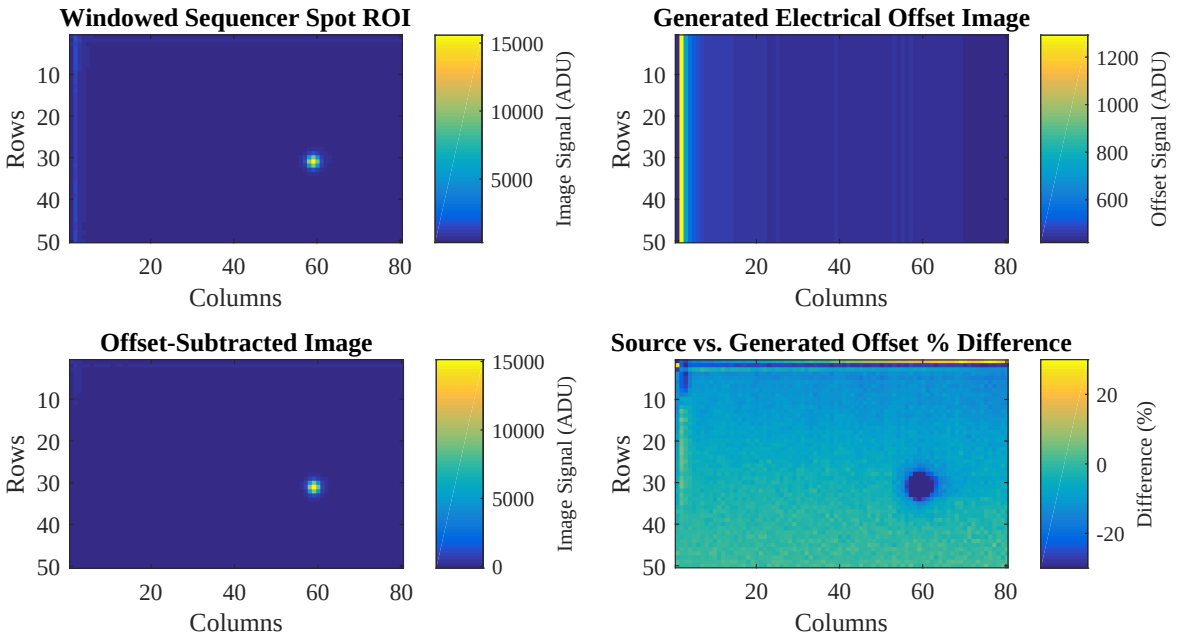

FIGURE 6.12: The electrical offset is generated using an approximation gathered from analysing other areas of the ROI, with the accuracy shown in the bottom right.

6.4.2 Methodology

With a population of 100 images per voltage, each set was averaged and measured for noise on a 100-sample per-pixel basis. The horizontal and vertical line profiles were

analysed as in Section 5.6.2, by applying a Gaussian fit and evaluating the half-maximum values for each slope to generate a value of FWHM in microns. Figures 6.13 and 6.14 demonstrate the line profiles at the two image clock voltage extremes, in which the centre pixel appears to have accumulated more charge at higher image clock voltage. The FWHM of the horizontal and vertical line voltages with respect to image clock voltage is investigated in Section 6.4.3.

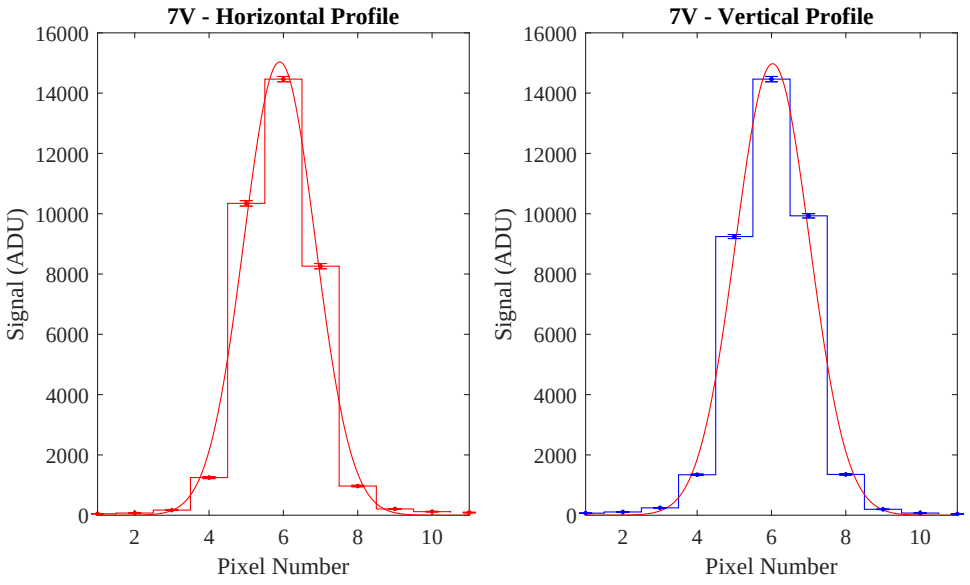

FIGURE 6.13: Gaussian fit for horizontal and vertical spot profile of an example spot integrated using 7V image clocks.

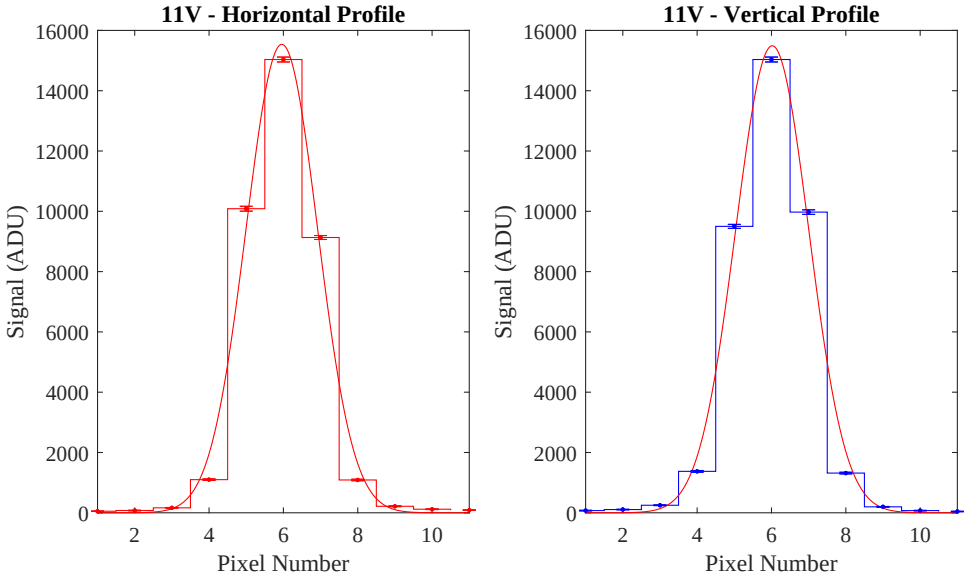

FIGURE 6.14: Gaussian fit for horizontal and vertical spot profile of an example spot integrated using 11V image clocks.

6.4.3 Experimental Analysis

Plotting the calculated FWHM as in Figure 6.15 yields an interesting observation: The image clock voltage has a noticeable effect on the FWHM in the vertical (column) direction and a similar but smaller effect in the horizontal (row) direction, which corroborates the theory that the Brighter-Fatter Effect (BFE) is indeed due to some change in electrostatic potential. This experiment has been carried out since by Antilogous et. al. [37] on a CCD250 device destined for the ground-based Large Synoptic Survey Telescope and their results share similarity with the data seen here for the CCD273. It is important to remember that the PSF presented here is the *relative* total system PSF, affected by the imaging area electrode voltages, and not the deconvolved detector PSF which would instead describe a detector-isolated spatial impulse response. Figure 6.16 gives the data of Figure 6.15 in percentage form, as a percentage of the smallest FWHM recorded.

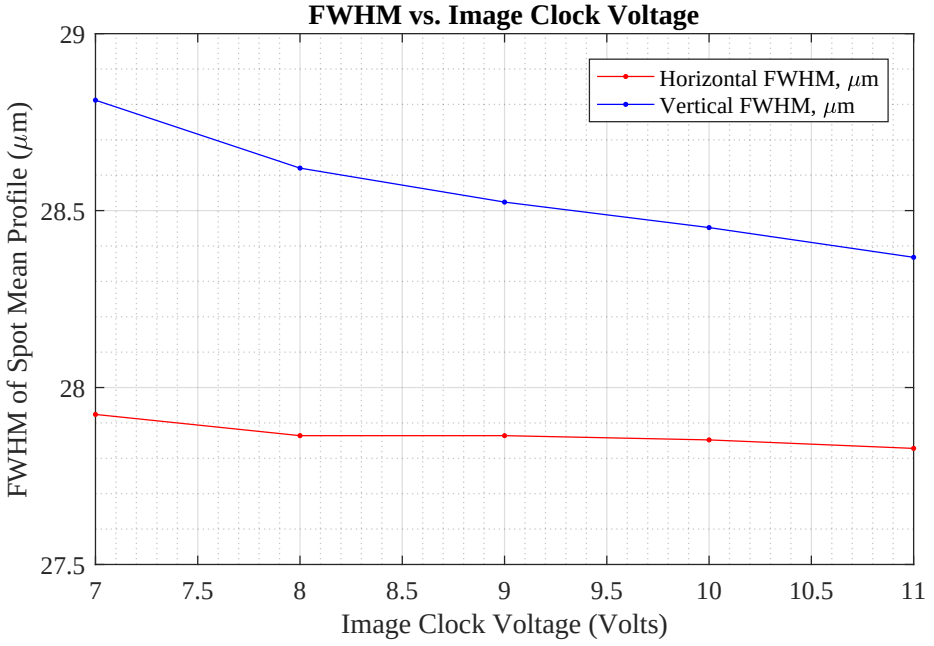

FIGURE 6.15: Vertical and horizontal FWHM measured from the same spot integrated under a range of image clock voltages.

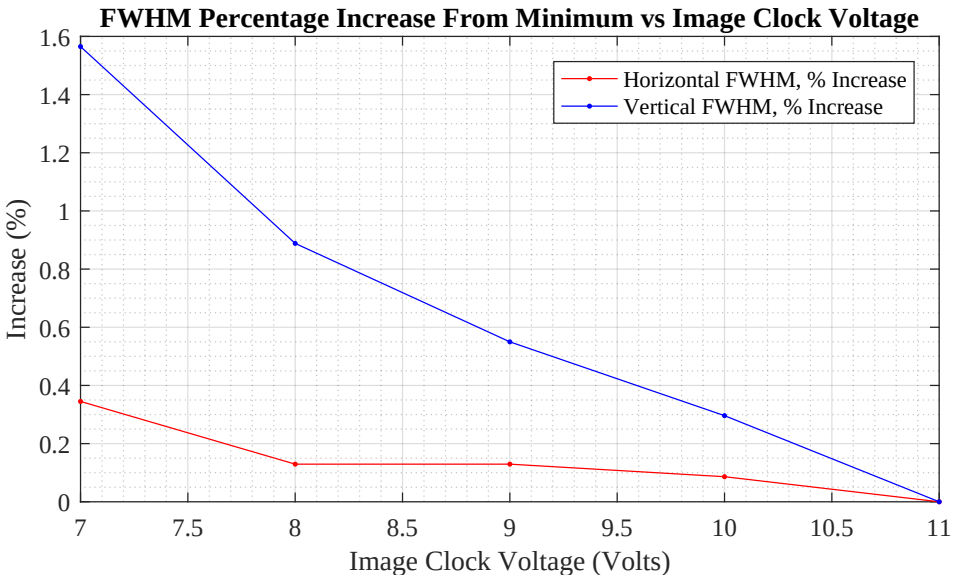

FIGURE 6.16: The vertical and horizontal percentage departure from the optimally measured FWHM at 11V.

6.5 Summary

Using the optical testing system and analysis algorithms developed as part of the wider project, the work within this chapter uses spot projections in order to investigate the Brighter-Fatter Effect in the Teledyne-e2v CCD273. Previously it was clear that spot images widen with signal, while the mechanism by which this occurs was unknown. The Multiple Illumination Experiment provided a dataset by which to look for preferential collection in the periphery, a "doughnut" of redistributed signal, to confirm the pixel electric field influence theory later to be confirmed in the literature. The effect of the electric field on the BFE was corroborated by gathering spot images with varied image clock (integrating electrode phase) voltages.

This experiment was partially published in *"Point-spread function and photon transfer of a CCD for space-based astronomy"* (Allanwood et. al., 2013) [41] and is cited in the Gaia DPAC tech note *Investigations into a Signal Level Dependency of the Gaia*

LSF [47], and thus has had an impact on the operation of Gaia and the perception of signal-dependent processing of spot images.

Chapter 7

Optimising the CCD273

7.1 Introduction

Scientific imaging devices require performance tuning in order to reveal their strengths and weaknesses with respect to the available operating parameters such as bias voltages and clocking schemes. There are a large number of adjustable variables affecting operation at any one time. This section illustrates the results of a slew of diagnostic tests which were carried out in order to imply the optimum configuration for the Teledyne-e2v CCD273, particularly with respect to the ongoing theme of point-source illuminations. Firstly, the response of the detector to a bright point-source illumination is investigated in Section 7.2, followed by an investigation into the benefits of back-surface pinning in Section 7.3: a measure taken in order to mitigate persistence between frames after a bright illumination. For the purposes of pixel capacity and point-source containment, the Full-Well Capacity (FWC) of the detector is characterised respect to which combination of the four pixel electrodes is utilised in Section 7.4. Finally, the detector integral

non-linearity is observed and optimised for supporting the experiments in the previous chapters, in Section 7.5.

7.2 Bright Spot Response

7.2.1 Motivation

Following previous characterisation work utilising LED flat-fields and X-rays on the structurally similar Teledyne-e2v CCD204 [18], a particular area of interest was how the CCD273 would perform given an unusually bright point source illumination. In real-life telescope operations this test would be analogous to an event where a bright object has the undesirable effect of dominating the field of view due to columnar charge blooming. As part of determining the suitability of an instrument such as the Euclid VIS camera system, potential problems such as high signal blooming behaviour are measured such that mitigation techniques can be considered.

7.2.2 Methodology

Data was gathered by projecting an arbitrarily very high signal laser spot for a long (400 seconds) integration time and varying the image clock voltage to observe any changes in the blooming behaviour. The specified integration time of Euclid VIS is 565 seconds [48]. The 400 seconds limit was a limitation imposed by the laboratory camera electronics hardware, although it is appropriately large enough to analyse the large signal blooming behaviour over a comparably long integration time.

Table 7.1 details the Interface Control Document (ICD) [49] values for CCD clocking and bias voltages used for this experiment, with the experimental variable parallel area image

clock voltage emboldened. These values represent defaults provided by the manufacturer, Teledyne-e2v, in a format pertinent to the XCAM Camera Utility (XCU).

Variable	Value (V)	Description
IG/DG/F3	10.0	Injection Gate, Dump Gate and Serial Register F Phase 3
Image	**8.0**	**Parallel Area Image Clock**
Serial	10.0	Serial Register Clock
Vig1	0.0	Central Charge Injection Structure Electrode 1
Vig2	0.0	Central Charge Injection Structure Electrode 2
Reset	11.0	Output Amplifier Reset Clock
Vrd	17.2	Output Amplifier Reset Drain (Vref)
Vdd	25.4	Output Common Drain
Vog	2.0	Output Gate
VodEF	27.3	Output Amplifier Output Drain (Quadrants E and F)
VodGH	27.3	Output Amplifier Output Drain (Quadrants G and H)
Vspr	0.2	(Spare)
Vspr	0.0	(Spare)
Vss	0.0	Substrate Node Voltage

TABLE 7.1: The Interface Control Document (ICD) voltages used in this experiment.

7.2.3 Potential Profiles

The CCD273 does not feature an anti-blooming drain, however; theoretically, by virtue of the horizontal and vertical potential profiles in the CCD, the direction of the charge spill from pixel to pixel can be manipulated by adjusting the image clock voltage, V_{Image}. Figure 7.1 examines the electric field potential in one dimension: from the perspective of looking down through the gate oxide, followed by the buried n-channel and finally the p-substrate. V_1 (shown in blue) represents a standard (e.g. 8 V) V_{Image}, while V_2 (shown in orange) represents an exaggerated increase (e.g. 11 V). Both profiles are shown with charge populations at Full Well Capacity (FWC), except V_1 is at Blooming Full Well (BFW), while V_2 is at Surface Full Well (SFW). $V_{P-Barrier}$ represents the parallel barrier phase potential which is zero volts at the gate oxide but boosted at depth by the in-built n-channel potential. The distinction between V_1 and V_2 is illustrated by their colour-corresponding charge clouds. Metaphorically, the cloud for V_1 is shown to

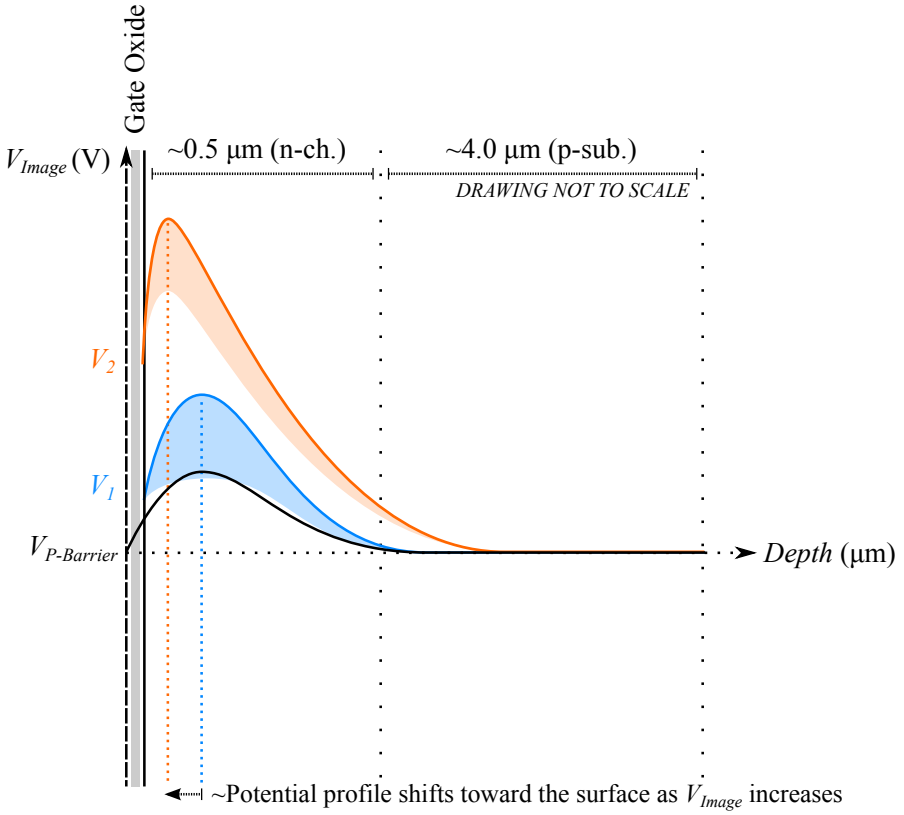

FIGURE 7.1: The potential profile shift as V_{Image} is increased from V_1 to V_2. The influence of the charge cloud are represented here by the shaded area under each potential profile curve. This is an abstract way of representing the decrease in the potential profile as the occupying charge increases.

overlap the barrier phase potential, thus as the amount of stored charge increases, the potential line decreases encroaching on that of $V_{P-Barrier}$. This causes charge to spill in the column direction (Vertical blooming). The charge cloud for V_2 is populated with the same amount of charge, however due to the increased electric field the charge cannot spill vertically - it has to go somewhere else i.e. *lateral blooming*.

Figure 7.2 visualises the top-down electric field distribution in a small number of pixels, with a cross section slice taken in the row direction. The two theoretical states rendered by different values of V_{Image} are shown side by side in order to compare the electric potential and charge volume distribution in the row direction. As V_{Image} is increased, the barrier phase $V_{P-Barrier}$ is constant, however; the potential profile of the active image

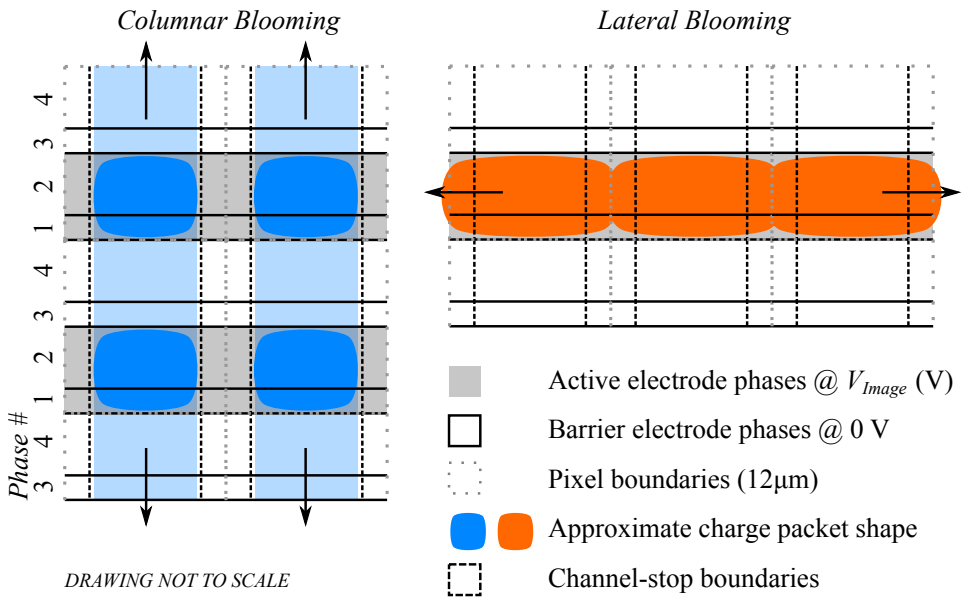

FIGURE 7.2: A top-down view of vertical and lateral blooming, affected by V_{Image}.

phase increases, thus the ability for the gathered charge to bloom vertically requires a higher charge volume. As shown in Figure 7.1, the charge packet is drawn closer to the surface and due to the increased barrier potential the charge cannot move vertically, therefore it moves laterally instead as shown in Figure 7.2.

7.2.4 Acquired Blooming Distributions

Figure 7.3 shows a 400 column by 2200 row ROI around the spot projection location for voltage step increments in V_{Image} between 9 V and 11 V. In each image the parallel overscan is visible between rows 2066 and 2200, thus the vertical blooming does not encroach upon these regions.

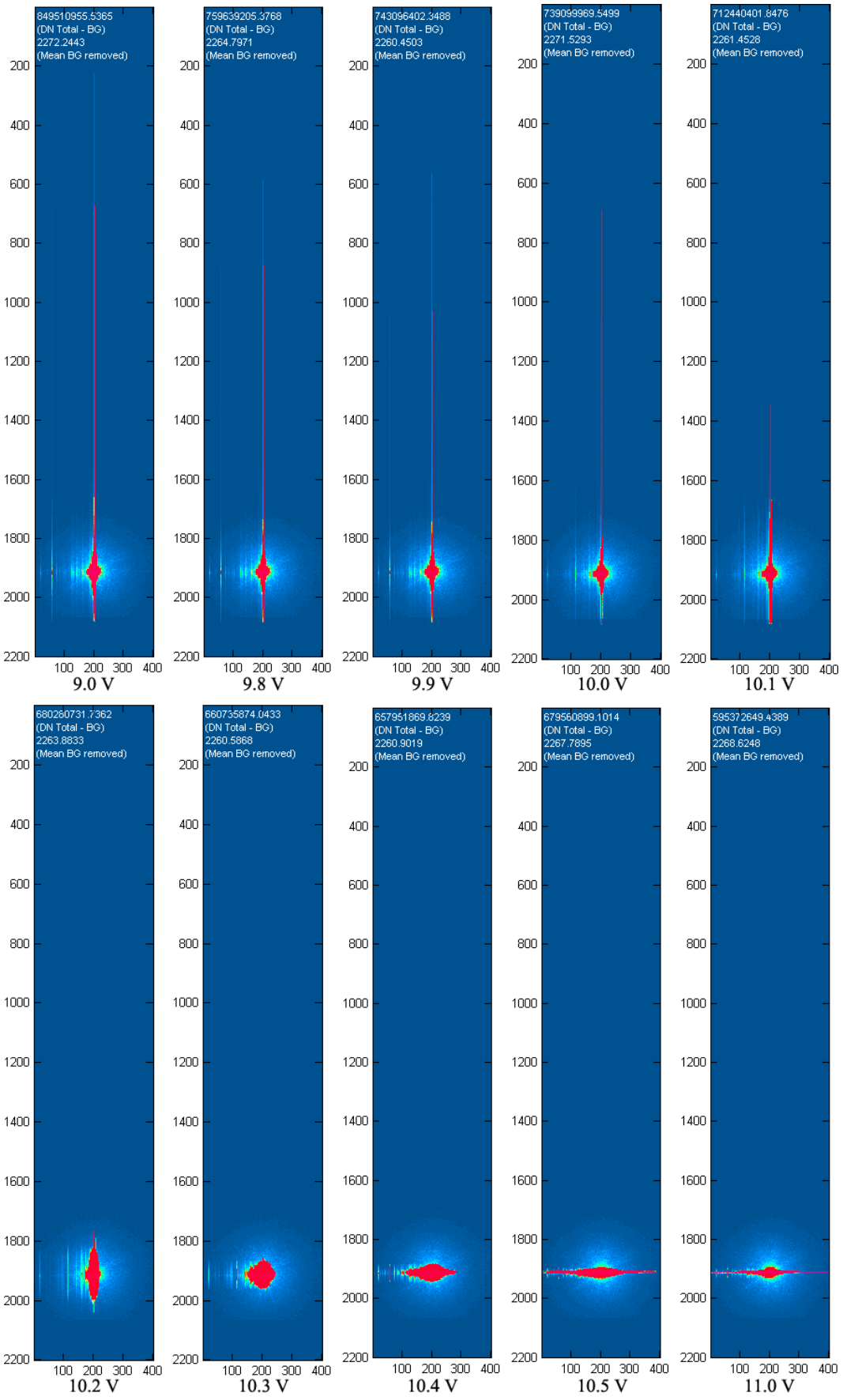

FIGURE 7.3: Blooming behaviour as a function of V_{Image} over a 400 s integration time.

7.2.5 Analysis

In Figure 7.3, note the change in blooming direction, starting at 10.2 V and terminating at 10.5 V. At 10.3 V there appears to be a point at which the charge appears to bloom almost isotropically. The dominance of objects causing blooming in images is undesirable therefore a V_{Image} setting of 10.3 V could seem appealing, however: increasing V_{Image} is subject to a cost-benefit analysis.

Recall the three potential profiles of Figure 7.1. At a standard V_{Image} the stored charge is held at an appropriate distance from the gate oxide *surface states*, in the n-type buried channel. As V_{Image} is increased the potential profile peaks closer to the surface and at a certain level, surface interaction occurs prior to vertical blooming (SFW). This is undesirable as interaction of the charge packet with dangling bonds of the SiO_2 interface allows charge traps to be filled, causing considerable Charge Transfer Inefficiency (CTI). The purpose of the doped buried channel is to draw charge away from the surface to improve Charge Transfer Efficiency (CTE) and a higher V_{Image} negates that effect. A desirable feature of an increased V_{Image} is that the area of the image dominated by the vertically blooming charge is reduced (as shown in Figure 7.3). This represents a trade-off between full well capacity below SFW and optimisation for minimal imaging area disruption during vertical blooming. It was observed during gathering the data for this experiment that significant charge persistence occurs at high signal levels. In effect there is a "ghost" signal at the spot projection site in subsequent dark frames, as charge is released from slow traps which are activated by the large charge volume from the previous frame. This behaviour is investigated experimentally and optimised in Section 7.3. Figure 7.4 illustrates the relationship between FWC and applied image clock voltage, V_{Image}: When V_{Image} is equal to the channel parameter value Φ_{Ch-0},

the amount of charge that can be stored before interaction with charge-trapping surface states decreases, hence there is a cusp at $V_{Image} = \Phi_{Ch-0}$. This concept is discussed in the 2013 SPIE paper *"Multi-level parallel clocking of CCDs for: improving charge transfer efficiency, clearing persistence, clocked anti-blooming and generating low noise backgrounds for pumping"* by Murray. N. J., Allanwood E. A. H., et. al. [50].

7.3 Pinning the Surface

7.3.1 Definition

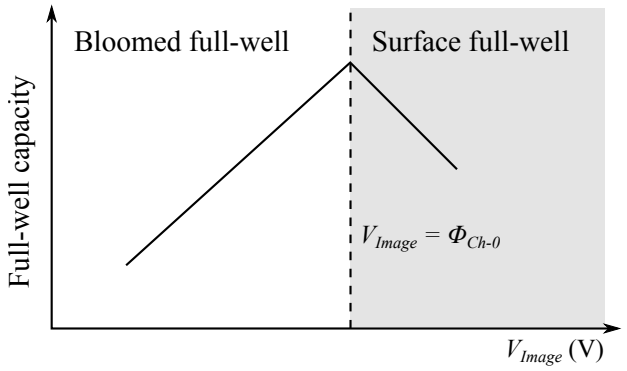

FIGURE 7.4: Cartoon showing the field applied by the image clock electrodes reaching the channel potential and the potential consequences of surface interaction, courtesy of Neil Murray [50]

Janesick [39] states pinning as:

"A bias condition that occurs when the signal channel is driven into inversion and pins the Si-SiO_2 surface potential to substrate potential."

Figure 7.4 illustrates the hypothesised full-well capacity trend as the bias applied to the image phase electrodes, V_{Image} is increased. Note that as V_{Image} exceeds the buried channel parameter Φ_{Ch-0}, the stored charge interacts with the surface. For the CCD273

Φ_{Ch-0} is approximately 10 V. Murray [50] introduces a technique for temporarily flooding the surface with holes, thus aiding the recombination of trapped electrons in surface states. Pinning involves causing inversion at the surface by some means - either by applying a positive voltage to the substrate (V_{SS}) or a negative voltage to the image phase electrodes (V_{Image}). The latter was not possible with the camera electronics available due to a lack of a negative supply, yet the former was configurable and tested in the course of this work.

7.3.2 Methodology

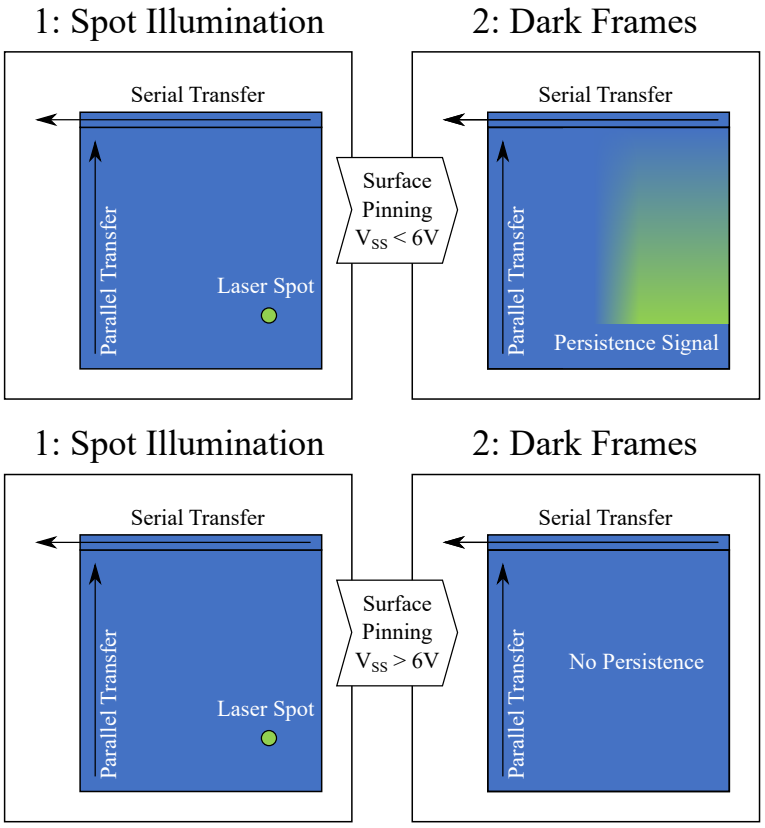

FIGURE 7.5: Diagram illustrating the pinning process and the consequences of the value of V_{SS}. The laser spot was projected with an integration time of 3 seconds, with subsequent dark frames of 300 seconds.

In order to investigate the signal persistence behaviour of the CCD273 with substrate pinning, voltages from 1V to 11V were applied to the substrate pin, V_{SS} and a ROI

established in order to measure the mean persistence. Prior to characterisation, several dark frames were averaged to subtract from frames following the laser illumination. Figure 7.5 illustrates the experimental process while Figure 7.6 shows raw full-image data. Full-frames are shown, with the bright laser illumination in the bottom right. The other frames represent the image following the illumination for varying values of V_{SS} and the time for which V_{SS} is pulsed high. The top-left frame represents the following image with no pinning and signal released from surface state traps is clearly visible.

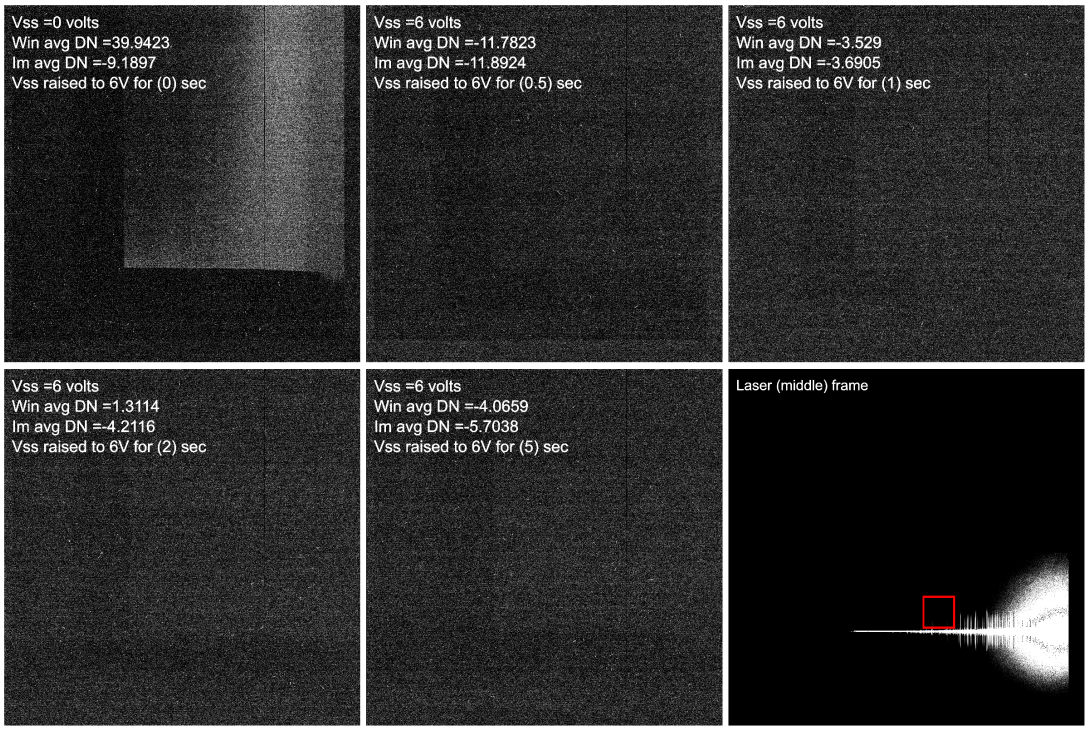

FIGURE 7.6: Frames showing the illumination and image persistence depending on the level and duration of V_{SS}.

Figure 7.7 illustrates the data from Figure 7.6 in the order that it was taken, with colour axes such as to represent the persistence below and above the critical value of V_{SS} required to clear the surface states.

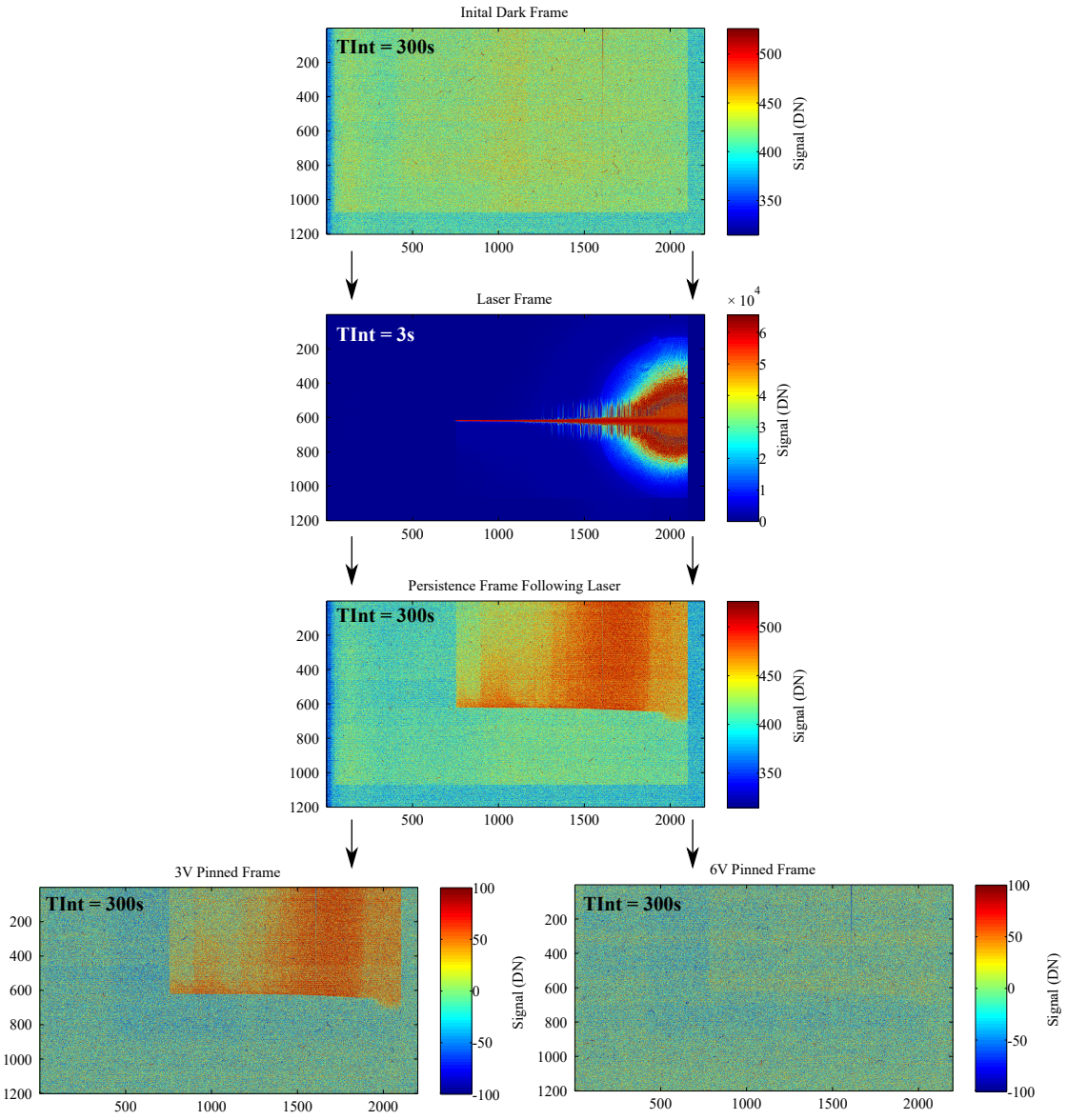

FIGURE 7.7: Process used to generate data for analysis of persistence based on pinning voltage.

7.3.3 Experimental Analysis

The mean persistent signal was measured versus V_{SS} and is plotted in Figure 7.8. In this context, *mean persistent signal* represents the mean signal remaining in the illumination area (top right of image), when the pre-illumination background level has been subtracted. This persistent signal is what remains when the pinning level is too low and cannot clear out the surface states. Figure 7.8 shows a step at approximately between

4V and 5V in sampled data, where this signal is removed: therefore the $V_{SS(Critical)}$ for the CCD273 should be above $V_{SS} = 5V$.

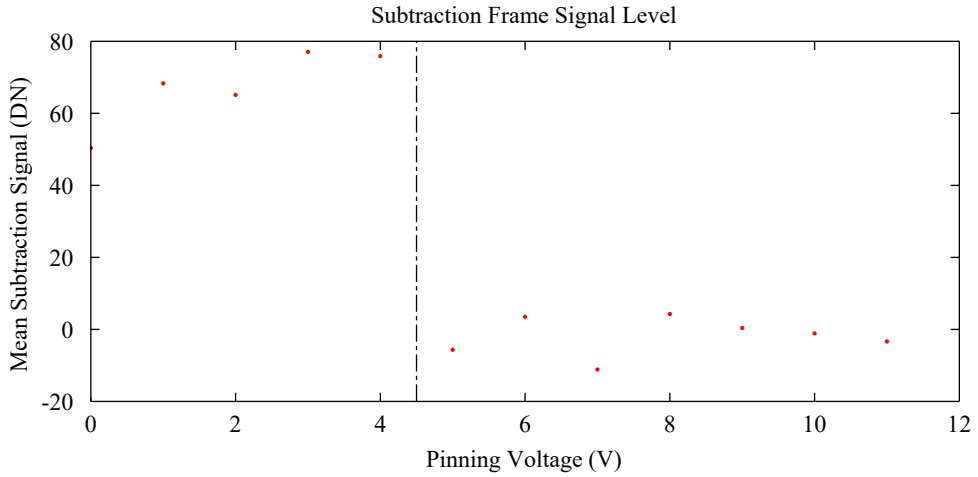

FIGURE 7.8: Graph showing the mean persistent signal from the previous frame versus the pinning voltage used to empty the traps in the surface states.

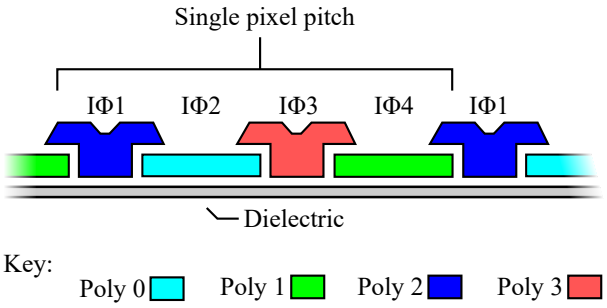

FIGURE 7.9: Electrode arrangement of a single pixel and numbering, featuring corresponding polysilicon layers.

7.4 Integrating Phase Optimisation

7.4.1 Motivation

Recall the influence of the potential well available for accumulating charge and how it is determined by the electric field of the overlying electrodes: In the CCD273 the electrode structure is four phase with two large phases and two smaller phases in a large-small-large-small arrangement, as in Figure 7.9. The electrodes are labelled as $I\phi[n]$ where n enumerates the electrode from one to four. Nominally, each electrode has widths of 3.5 µm or 2.5 µm , however, manufacturing tolerances may vary on an area, node, device and wafer basis. Clarke et. al. [51] demonstrates a destructive method for measuring electrode arrangement and geometric variations using Focused Ion Beam Scanning Electron Microscope (FIBSEM) images. This section presents data which evaluates different electrode configurations, utilising a spot illumination with the goal of optimising Full-Well Capacity (FWC), while investigating the spatial implications of each configuration.

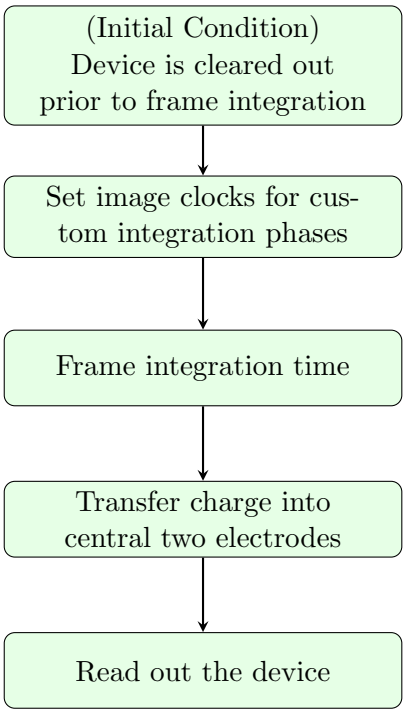

FIGURE 7.10: Sequence for custom electrode collection, with transport into standard central phases before normal parallel readout.

7.4.2 Methodology

In order to evaluate charge collection performance, electrodes were operated as individual charge collecting phases. To achieve this a range of clock sequencers were written in which the phase under test was turned on during collection, followed by the necessary clock sequence to transfer the charge into the pixel centre for a standard CCD273 readout sequence. The testing procedures for setting integrating clock sequences and readout are detailed in Figure 7.10. A fixed-focus 12 µm FWHM spot image was projected, with the image re-centred in the X and Y direction using the integrating phase under test prior to each experimental run. The preferential charge spreading direction, previously defined in Section 5.5 as Aspect Ratio (AR), was recorded relative to signal, which ranged from approximately 1000 electrons to beyond Full-Well Capacity (FWC).

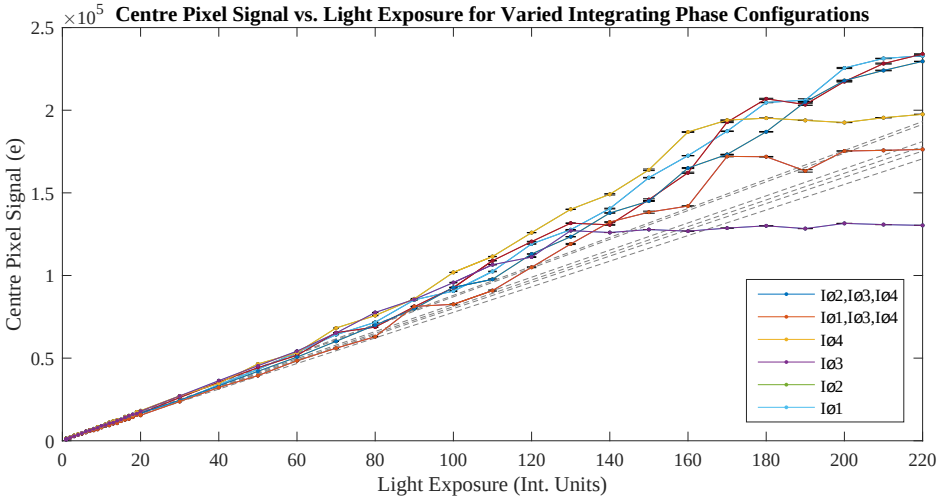

FIGURE 7.11: Accumulated centre pixel signal with respect to light exposure level and utilised integrating phases.

7.4.3 Experimental Analysis

Figure 7.11 plots the centre pixel response of a spot, optimally focused and centred over different groups of integrating phases. The x-axis represents a sweep of integration time units, where one unit is approximately equal to 0.1 seconds of clock sequencer delay during frame exposure. A linear fit to the small signal range of each series is illustrated behind, with the residuals in electrons shown in 7.12. In Figure 7.12, the integral non-linearity evident in the centre pixel optical response is not an artefact of collecting phase or pixel, but of the output amplifier as discussed in Section 7.5.

Figure 7.13 illustrates the change in AR with respect to applied signal for a range of integrating phases. The legend of Figure 7.13 denotes which phases are enabled during collection for each data series. In CCD clocking nomenclature, the inactive phase is often referred to as the barrier phase, thus the omitted phases in each entry serve the purpose of charge barrier in the column direction.

Note that $I\phi 1$ appears to be the least capacious of the collecting phases with respect to FWC while $I\phi 4$ appears as if it has the collecting capacity comparable to several other

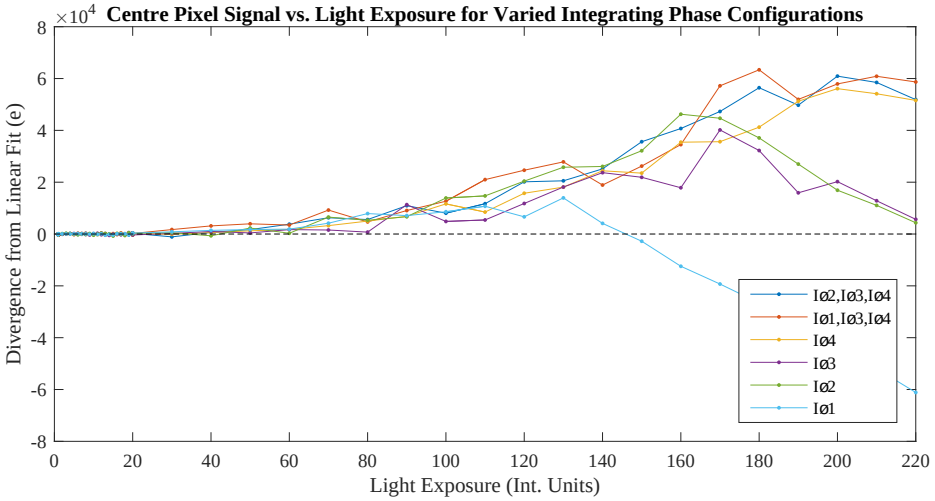

FIGURE 7.12: Divergence from small-signal linear fit with respect to light exposure level and utilised integrating phases.

collecting phases combined. While the full-well capacity of $I\phi1$ appears to be low, the AR is approximately isotropic in nature until the roll-off, a feature which identifies it as one of the two smaller phases. $I\phi3$ is similar in nature to $I\phi1$ with a consistent AR and low FWC. The most capacious single collecting phase is $I\phi4$, however $I\phi4$ exhibits over 5% anisotropy at 20 ke, as illustrated with the axes constrained to small signals in Figure 7.14.

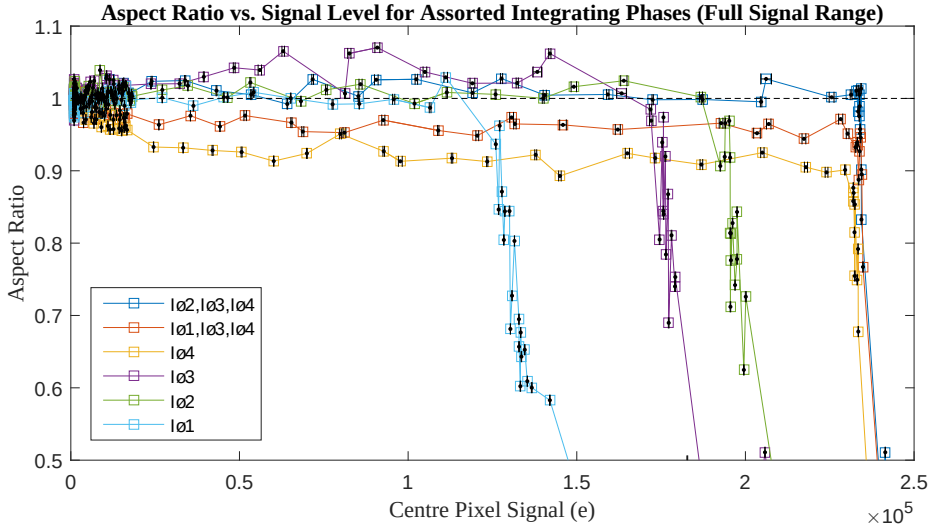

FIGURE 7.13: Spot anisotropy versus integrating phase (Full signal range).

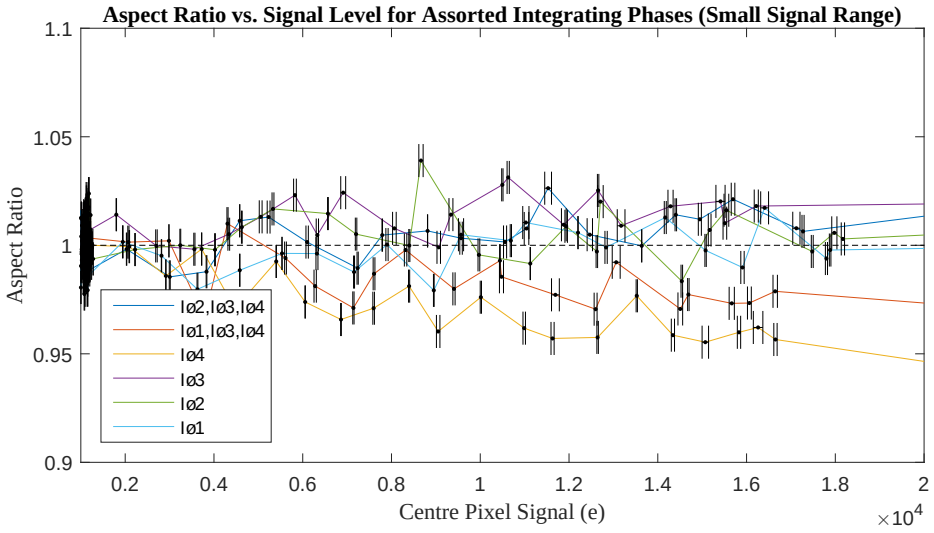

FIGURE 7.14: Spot anisotropy versus. integrating phase (Small signal range)

This phenomenon of collecting phase anisotropy does not apply to all the image phases tested. In the context of the Euclid mission where weak lens detection of slight shape perturbations is paramount, the most isotropic collecting phase scheme must be used. From the data presented it appears that using $I\phi1$ as a barrier phase, with $I\phi2$, $I\phi3$ and $I\phi4$ used as collecting phases gives the optimal performance in terms of sub-blooming isotropy, for this particular device.

Figure 7.15, obtained by Clarke [51] features an image on an unused CCD273 wafer taken by a Focused Ion Beam Scanning Electron Microscope (FIBSEM), which confirms that there should be slight differences between the capacity of the phases tested.

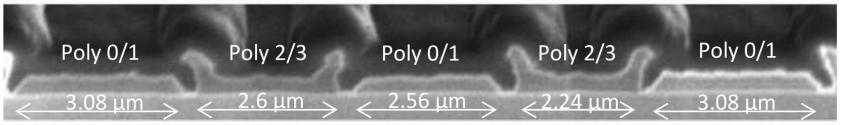

FIGURE 7.15: FIBSEM cross section courtesy of Andrew Clarke, revealing the electrode widths of an unused CCD273 wafer.

7.5 Integral Non-linearity

7.5.1 Review of Observed Non-linearity

Figure 7.16 illustrates the CCD273 response to the SP-PTC method, with a fit to the small-signal range of the device. Over 30% non-linearity is demonstrated at the saturation point of the detector, which proved problematic when attempting to execute the Multiple Illumination Experiment of Section 6.3.1 as it was dependent on frame differencing of different signal levels. Following an internal discussion with Teledyne-e2v it was recommended that the output drain voltage, V_{OD} be tuned so as to operate with better linearity, the results of which are shown in Figure 7.17.

7.5.2 Characterisation and Software Correction

While the data of Figure 7.17 shows improved linearity for a higher output drain voltage, the data saturates at 2^{16} ADU, effectively the ADC saturation point. A larger ADC input range or alternatively, attenuation and recalibration was required to see the CCD FWC, currently obscured by the ADC saturation point. Therefore it was not possible to make an assertion on the linearity optimisation of this particular CCD273. All experiments in this thesis were conducted with the values in Table 7.1 unless otherwise stated. In order to account for artificial "excess" charge granted by the +30% non-linearity in the data a software transfer function was generated in order to linearise data. The transfer characteristic is shown in Figure 7.18.

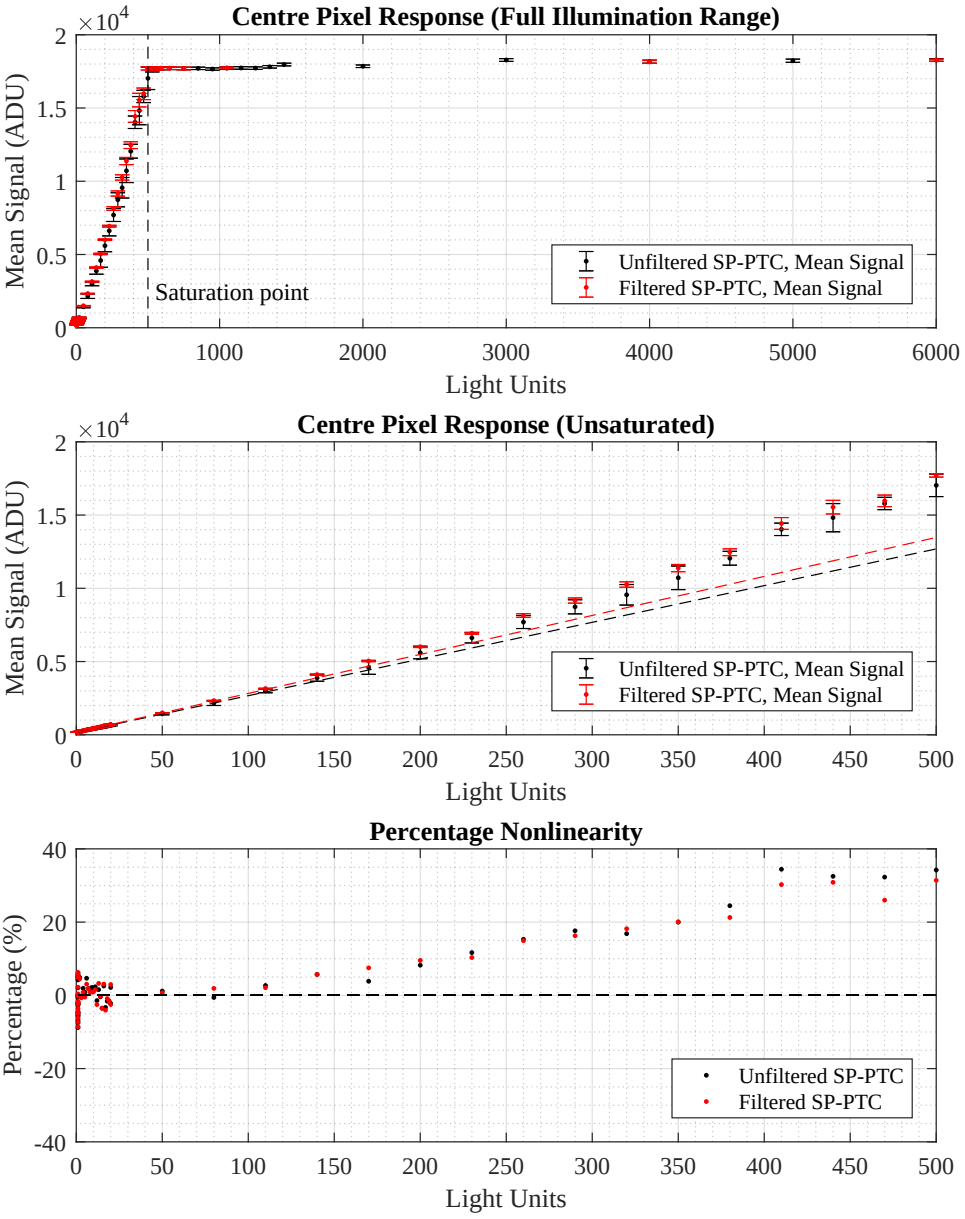

FIGURE 7.16: Data from the SP-PTC acquisition of 5.3, illustrating the signal and linearity versus integration time with a stable illumination.

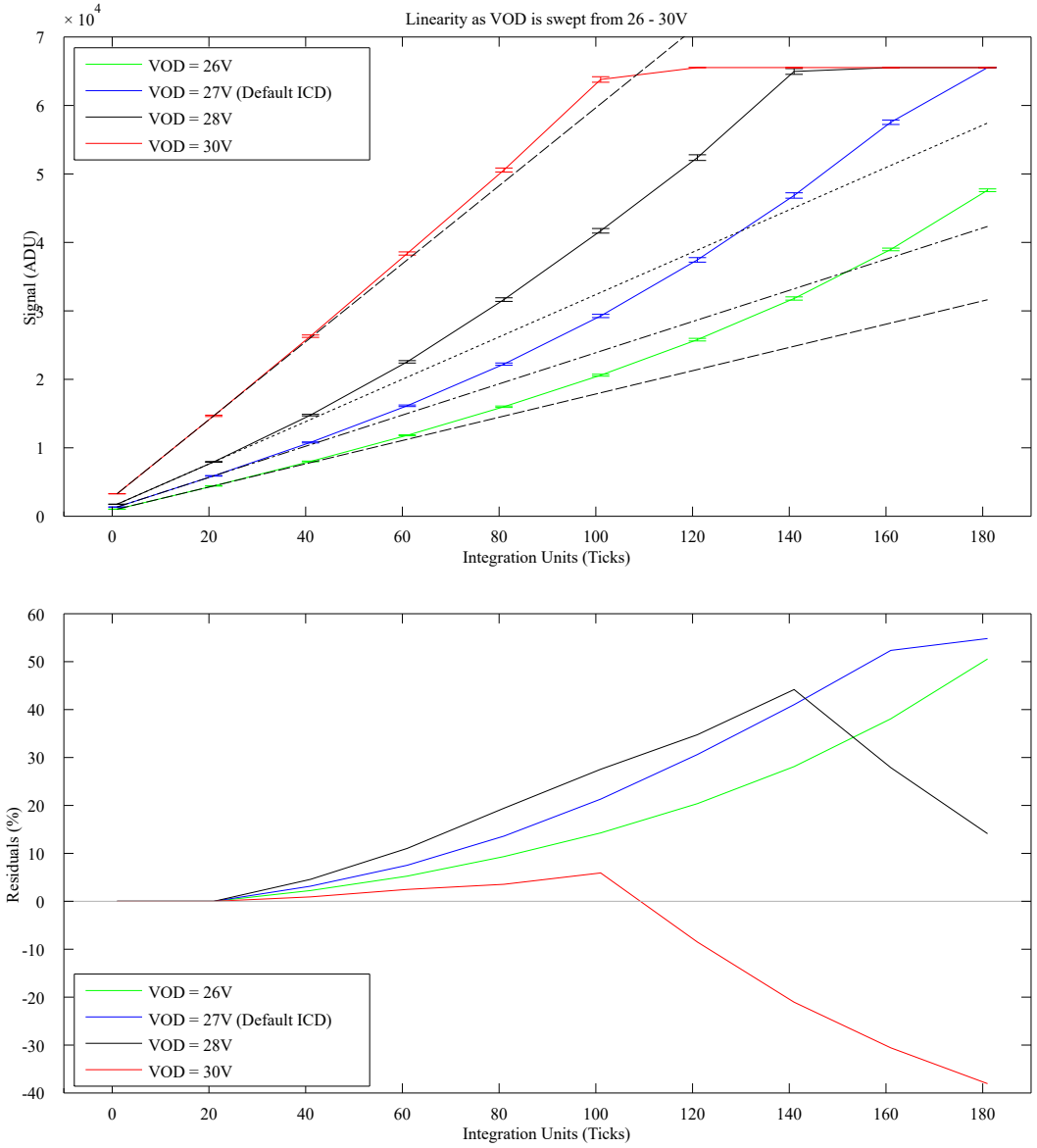

FIGURE 7.17: Graph illustrating the the linearity of the CCD273 as VOD is raised between 26 V and 30 V.

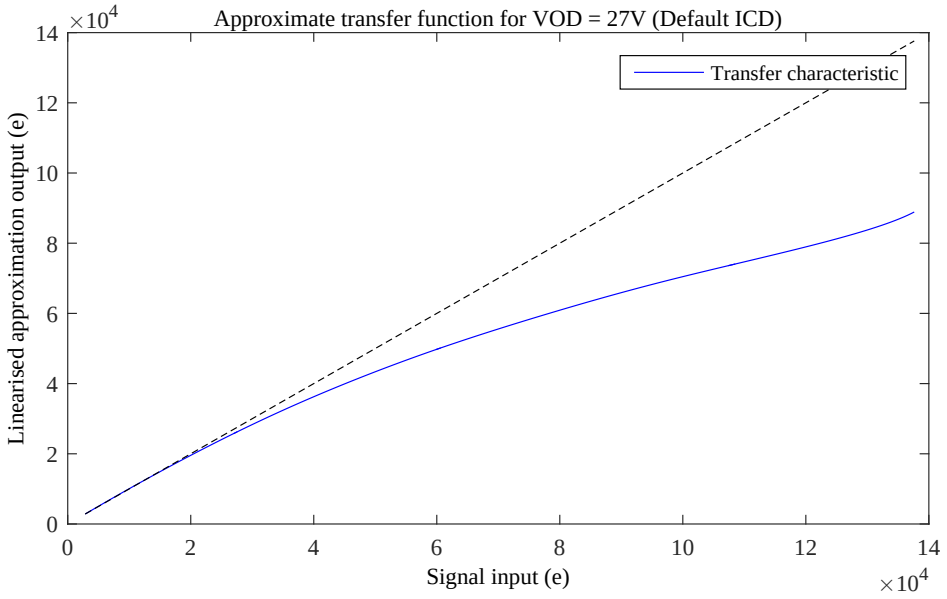

FIGURE 7.18: A transfer function generated in order to linearise ADC values in order to support differencing in the Multiple Illumination Experiment of Section 6.3.3

7.6 Summary

This chapter parameterises operating voltages of the CCD273 in order to judge relative performance and make recommendations for the Euclid VIS camera. Of particular interest are the image clock voltage, substrate surface pinning voltage and output drain voltage, which are V_{Image}, V_{SS} and V_{OD}, respectively.

The bright spot response was addressed through perturbation of the image clock voltages, V_{Image} in the presence of a controlled bright laser illumination. For $V_{Image} > \phi_{Ch-0}$, where ϕ_{Ch-0} is the channel potential 10V, it was discovered that considerable image persistence occurs as the charge volume interacts with the surface states or "dangling bonds". A scheme by which the substrate voltage V_{SS}, could be raised to 6 V to temporarily flood the surface with holes was shown to eliminate persistence in subsequent frames.

The configuration of integrating electrodes was varied in order to investigate if spot anisotropy is a product of any one of the four integrating phases. It was discovered that the integrating phases represent varied levels of full well capacity and become anisotropic with variable degrees, prior to blooming, however, the most interesting assertion to be made is over the choice of barrier phase. The phase $I\phi 2$ was shown to be an inferior barrier phase to $I\phi 1$, in the small signal range. $I\phi 3$ and $I\phi 4$ were not tested as barrier phases which could represent further work. In future this method could be used to validate the electrode performance in several areas of a device.

For laboratory optimisation a scheme was developed for linearising the CCD273 output, although in absence of compatible ADC hardware the full output swing at higher levels of output drain voltage, V_{OD}, was not measured. A higher V_{DS} (Drain-source voltage: the voltage between source follower drain and source, associated with running in saturation

mode) is desirable in terms of linearity when large signals are being measured [39] but this may not be desirable in terms of power consumption.

Chapter 8

Conclusions and Further Work

This study represents one of many complementary studies at the Centre for Electronic Imaging in the context of electro-optical characterisation of the Teledyne-e2v CCD273 and the structurally similar CCD204 [52]. In addition to the existing studies of charge transfer inefficiency [18, 53–55], charge trapping behaviour [56, 57], trap mitigation techniques [50] and validated pixel modelling [46, 51, 58], an empirical observation of charge collection behaviour is presented.

An optical test bench was designed, constructed and characterised in order to deliver repeatable spot projections by which to make assertions regarding the relative point spread function response of a front-illuminated Teledyne-e2v CCD273 test device. A focusing and spot-centring algorithm was developed such that the spot images for each testing run could be suitably repeatable. It was hypothesised that spot images were subject to sub- 100 Hz mechanical vibration in the horizontal (CCD row) direction due to horizontal smearing in mean spot images. Spot smearing was mitigated by the use of millisecond-scale integration and illumination times and a centre of mass based dataset filtering technique inspired by the concept of lucky imaging astronomy. The

filtered dataset showed that spots positionally in-phase with the pixel centre could be recovered. The Single-Pixel Photon Transfer Curve technique was created in order to characterise spot images with respect to signal and it has since been utilised in at least one other Euclid-oriented study [59].

Measurements are presented in terms of the relative system PSF, rather than the isolated detector-only PSF. The development of a system where the optical contribution to the PSF is known, such that the detector PSF can be deconvolved, is material for further work. Prompted by the stringent 0.1% shape measurement requirements of Euclid VIS, a system point spread function response was measured and confirmed to vary in Full-Width at Half-Maximum (FWHM) with respect to signal, later corroborated by the contemporary publication of the Brighter-Fatter Effect [37]. At the time of experimentation the cause for the BFE was speculation, thus an experiment was devised using a combination of spot and flat-field projections with the purpose of manipulating the BFE and observing the amount of redistributed charge. The hypothesis was such that an existing population of charge in a pixel makes it less attractive for charge collection compared to pixels in the immediate periphery, due to a reduced electric field. This was shown to be a convincing hypothesis upon comparison of the spot centre pixel charge with that of the periphery, for a range of spot and flat-field combinations in the Multiple Illumination Experiment.

Further to the Multiple Illumination Experiment, the spot FWHM was characterised with respect to the parallel image clock voltage, V_{Image}. It was hypothesised that with a deeper depletion depth afforded by a higher V_{Image}, the effect of the BFE would be mitigated. Both columnar-direction and row-direction FWHM are shown to decrease with increased V_{Image}, with the columnar FWHM decreasing by a factor of nearly 1% between the Euclid mission operating V_{Image} of 8 V and the increased experimental

V_{Image} of 11 V. From the FWHM versus V_{Image} data it would seem prudent to recommend that the mission operating V_{Image} be increased in order to improve horizontal and vertical spatial resolution. In the analysis of bright spot response it was shown that values of V_{Image} greater than the channel parameter ϕ_{CH0}, approximately equal to 10 V, allows interaction of the charge volume with the dangling bonds, filling the surface states. For the purposes of Euclid in which the quadrants are a sizeable 2k $\times$ 2k pixels, reduction of charge transfer inefficiency is paramount and it is ill-advised to allow charge to access the surface states. A higher V_{Image} also presents a higher power demand to the flight electronics, where voltage, capacitance of clock electrodes and clock frequency are relative factors determining dynamic power consumption.

Substrate or V_{SS} pinning was utilised as an experimental variable in order to experiment in clearing out occupied surface states by quenching them with a flood of holes. A V_{SS} of 6 V was found to be adequate in clearing out any persistence from a bright laser illumination and could be useful in the operation of Euclid VIS. V_{OD}, the output amplifier drain bias was characterised in order to improve signal linearity, and a higher V_{OD} was found to exhibit less than five percent non-linearity across the observable signal range. The full well capacity of the CCD273 was not observed across this range due to ADC saturation, therefore other experimentation was conducted using the default interface control document value of $V_{OD} = 27$ V. The 30% non-linearity at high signal levels was deemed to be an effect limited to the output amplifier and camera electronics, therefore a transfer function was utilised to linearise images on a pixel-by-pixel basis. This transfer function allowed the charge contributions of multiple illuminations to be successfully added and subtracted from one another proportionally which was a critical element of the Multiple Illumination Experiment of Chapter 6.

Since the conclusion of experimentation on the front-illuminated CCD273, the optical test bench development and documented practices have contributed to the design and operation of optical test benches for the ESA p-channel study and JUICE JANUS study. The JANUS instrument, the Teledyne-e2v CIS115 CMOS image sensor is the geomorphological camera on the JUpiter ICy moon Explorer (JUICE) and is currently under characterisation by the Centre for Electronic Imaging. The optical test system is constructed from many of the same hardware and software components, with improved optics based on a tube lens and super-achromatic microscope objective, as opposed to the spherical aberration limited achromatic doublets utilised here. In this case the spatial contribution of the system optics can be modelled and toleranced by Zemax Opticstudio in order to isolate the detector spatial performance, a desirable data sheet figure of merit. Currently, work continues on expanding into measurement of quantum efficiency and modulation transfer function to build a complete optical characterisation test facility, based on the legacy of the system presented here.

Bibliography

[1] Saul Perlmutter et al. Supernovae, dark energy, and the accelerating universe. *Physics today*, 56(4):53–62, 2003.

[2] Richard Massey, Jason Rhodes, Richard Ellis, Nick Scoville, Alexie Leauthaud, Alexis Finoguenov, Peter Capak, David Bacon, Hervé Aussel, Jean-Paul Kneib, et al. Dark matter maps reveal cosmic scaffolding. *Nature*, 445(7125):286–290, 2007.

[3] Richard Massey, Thomas Kitching, and Johan Richard. The dark matter of gravitational lensing. *Reports on Progress in Physics*, 73(8):086901, 2010.

[4] Alexandre Refregier, Adam Amara, TD Kitching, Anaıs Rassat, Roberto Scaramella, Jochen Weller, et al. Euclid imaging consortium science book. *arXiv preprint arXiv:1001.0061*, 2010.

[5] ADT Short, D Barry, M Berthe, N Boudin, O Boulade, R Cole, M Cropper, L Duvet, J Endicott, L Gaspar Venancio, et al. The euclid vis ccd detector design development and programme status. In *Proc. SPIE*, volume 9154, page 91540R, 2014.

[6] Giuseppe D Racca, René Laureijs, Luca Stagnaro, Jean Christophe Salvignol, Jose Lorenzo Alvarez, Gonzalo Saavedra Criado, Luis Gaspar Venancio, Alex Short,

Paolo Strada, Tobias Boenke, et al. The euclid mission design. *arXiv preprint arXiv:1610.05508*, 2016.

[7] Mark Cropper, Henk Hoekstra, Thomas Kitching, Richard Massey, Jérôme Amiaux, Lance Miller, Yannick Mellier, Jason Rhodes, Barnaby Rowe, Sandrine Pires, et al. Defining a weak lensing experiment in space. *Monthly Notices of the Royal Astronomical Society*, 431(4):3103–3126, 2013.

[8] Kurt Rossmann. Point spread-function, line spread-function, and modulation transfer function: tools for the study of imaging systems. *Radiology*, 93(2):257–272, 1969.

[9] WS Boyle and GE Smith. Charge-coupled devices-a new approach to mis device structures. *Spectrum, IEEE*, 8(7):18–27, 1971.

[10] JP Eckert Jr. A survey of digital computer memory systems. *Annals of the History of Computing, IEEE*, 20(4):15–28, 1998.

[11] Willard S Boyle and George E Smith. The inception of charge-coupled devices. *Electron Devices, IEEE Transactions on*, 23(7):661–663, 1976.

[12] M Fo Tompsett, GF Amelio, and GE Smith. Charge coupled 8-bit shift register. *Applied Physics Letters*, 17(3):111–115, 1970.

[13] Helmuth Spieler. *Semiconductor detector systems*, volume 12. Oxford university press, 2005.

[14] Jason PD Gow, Daniel Wood, Neil J Murray, David Burt, David J Hall, Ben Dryer, and Andrew D Holland. Postirradiation behavior of p-channel charge-coupled devices irradiated at 153 k. *Journal of Astronomical Telescopes, Instruments, and Systems*, 2(2):026001–026001, 2016.

[15] Willard Sterling Boyle. Buried channel charge coupled devices, October 24 1974. US Patent 3,792,322.

[16] W. R. Buried channel charge coupled apparatus, December 3 1974. URL `http://www.google.com/patents/US3852799`. US Patent 3,852,799.

[17] Open Univeristy. Centre for Electronic Imaging. `http://www.open.ac.uk/science/research/cei/`, 2018. [Online; accessed 11-August-2018].

[18] JPD Gow, NJ Murray, AD Holland, DJ Hall, M Cropper, D Burt, G Hopkinson, and L Duvet. Assessment of space proton radiation-induced charge transfer inefficiency in the ccd204 for the euclid space observatory. *Journal of Instrumentation*, 7(01): C01030, 2012.

[19] Jason Gow, Neil Murray, Andrew Holland, and Simeon Barber. Euclid p-channel and n-channel comparison: Post-irradiation characterisation.

[20] Inc Brooks Automation. PCC Compact Coolers - Next Generation CryoTiger. `http://www.brooks.com/products/cryopumps-cryochillers/cryochillers/pcc-compact-coolers`, 2015. [Online; accessed 25-February-2015].

[21] e2v Technologies Plc. CCD273 Device Layout, 2011. [Internal communication with James Endicott (e2v), 13-February-2014].

[22] James Endicott, S Darby, S Bowring, D Burt, T Eaton, A Grey, I Swindells, R Wheeler, L Duvet, M Cropper, et al. Charge-coupled devices for the esa euclid m-class mission. In *SPIE Astronomical Telescopes+ Instrumentation*, pages 845304–845304. International Society for Optics and Photonics, 2012.

[23] D Burt, J Endicott, P Jerram, P Pool, D Morris, A Hussain, and P Ezra. Improving radiation tolerance in e2v ccd sensors. In *Proc. SPIE*, volume 7439, page 743902, 2009.

[24] XCAM Ltd. XCAM USB2REM Camera Electronics. `http://www.xcam.co.uk/products/electronics.html`, 2012. [Online; accessed 24-February-2015].

[25] Fischer Connectors SA. Fischer Core Series Connector. `http://www.fischerconnectors.com/global/en/products/fischer-core-series`, 2015. [Online; accessed 24-February-2015].

[26] James R Janesick. *Photon Transfer*. SPIE press Bellingham, WA, 2007.

[27] Inc ThorLabs. LED630E Spec-Sheet. `http://www.thorlabs.com/thorcat/16600/LED630E-SpecSheet.pdf`, 2007. [Online; accessed 03-March-2015].

[28] Benjamin J Dryer. *Characterisation of CMOS APS technologies for space applications*. PhD thesis, The Open University, 2013.

[29] Inc ThorLabs. ED1-S50 Product Listing. `http://www.thorlabs.de/thorproduct.cfm?partnumber=ED1-S50`, 2015. [Online; accessed 11-March-2015].

[30] Newport Corporation. High-Performance Mid-Range Travel Linear Stages: ILS Series, 2017. [Online; accessed 26-September-2017].

[31] Newport Corporation. Precision Long-Travel and High-Speed Motorized Actuators: User's Manual, 2017. [Online; accessed 26-September-2017].

[32] Bruce H Walker. *Optical engineering fundamentals*, volume 82. Spie Press, 2008.

[33] Lord Rayleigh. Xxxi. investigations in optics, with special reference to the spectroscope. *The London, Edinburgh, and Dublin Philosophical Magazine and Journal of Science*, 8(49):261–274, 1879.

[34] M Downing, D Baade, S Deiries, and P Jorden. Bulk silicon ccds, point spread function and photon transfer curves: Ccd testing activities at eso. In *DfA Garching http://www. eso. org/sci/meetings/dfa2009*, 2009.

[35] Elisa H Barney Smith. Psf estimation by gradient descent fit to the esf. In *SPIE—Image Quality and System Performance III (Vol. 6059).*, page 60590E. International Society for Optics and Photonics, 2006.

[36] Mark Downing, Dietrich Baade, Peter Sinclaire, Sebastian Deiries, and Fabrice Christen. Ccd riddle: a) signal vs time: linear; b) signal vs variance: non-linear. In *Astronomical Telescopes and Instrumentation*, pages 627609–627609. International Society for Optics and Photonics, 2006.

[37] P. Antilogus, P. Astier, P. Doherty, A. Guyonnet, and N. Regnault. The brighter-fatter effect and pixel correlations in CCD sensors. *Journal of Instrumentation*, 9: C03048, March 2014. doi: 10.1088/1748-0221/9/03/C03048.

[38] Craig Mackay. High-efficiency lucky imaging. *Monthly Notices of the Royal Astronomical Society*, 432(1):702–710, 2013.

[39] James R Janesick. *Scientific charge-coupled devices*, volume 117. SPIE press Bellingham, WA, 2001.

[40] NJ Murray, EAH Allanwood, BJ Dryer, DP Weatherill, KD Stefanov, AD Holland, and DJ Burt. Comparison of point spread function in p-and n-channel ccds. *Journal of Instrumentation*, 10(08):C08007, 2015.

[41] Edgar AH Allanwood, Neil J Murray, Konstantin D Stefanov, David J Burt, and Andrew D Holland. Point-spread function and photon transfer of a ccd for space-based astronomy. In *SPIE Optical Engineering+ Applications*, pages 88600I–88600I.

International Society for Optics and Photonics, 2013.

[42] Robert K Reich. Sub-poisson statistics observed in an electronically shuttered and back-illuminated ccd pixel. *IEEE Transactions on Electron Devices*, 44(1):69–73, 1997.

[43] M Downing and Sinclaire P. The ccd riddle revisited: Signal vs. time – linear; signal vs. variance – non-linear. In *Proceedings of Scientific Detector Workshop, 2013*, 2013.

[44] Bedabrata Pain and BR Hancock. Accurate estimation of conversion gain and quantum efficiency in cmos imagers. In *Proc. of SPIE Vol*, volume 5017, page 95, 2003.

[45] Paul A Abell, Julius Allison, Scott F Anderson, John R Andrew, J Roger P Angel, Lee Armus, David Arnett, SJ Asztalos, Tim S Axelrod, Stephen Bailey, et al. Lsst science book, version 2.0. *arXiv preprint arXiv:0912.0201*, 2009.

[46] Daniel Philip Weatherill. *Charge collection in silicon imaging sensors*. PhD thesis, Open University, 2016.

[47] Crowley and Kohley. Investigations into a signal level dependency of the gaia lsf. *GAIA-CH-TN-ESAC-CMC-009-1*, 2013.

[48] Mark Cropper, R Cole, A James, Y Mellier, J Martignac, A-M Di Giorgio, S Paltani, L Genolet, J-J Fourmond, C Cara, et al. Vis: the visible imager for euclid. In *SPIE Astronomical Telescopes+ Instrumentation*, pages 84420V–84420V. International Society for Optics and Photonics, 2012.

[49] Teledyne e2v. Teledyne e2v ccd273 interface control document. 2010.

[50] Neil J Murray, David J Burt, Andrew D Holland, Konstantin D Stefanov, Jason PD Gow, Calum MacCormick, Ben J Dryer, and Edgar AH Allanwood. Multi-level parallel clocking of ccds for: improving charge transfer efficiency, clearing persistence, clocked anti-blooming, and generating low-noise backgrounds for pumping. In *SPIE Optical Engineering+ Applications*, pages 88600K–88600K. International Society for Optics and Photonics, 2013.

[51] Andrew Clarke. *Modelling and Verification for Euclid CCDs.* PhD thesis, The Open University, 2014.

[52] JPD Gow, NJ Murray, AD Holland, and David Burt. Proton damage comparison of an e2v technologies n-channel and p-channel ccd204. *IEEE Transactions on Nuclear Science*, 61(4):1843–1848, 2014.

[53] David J Hall, Andrew Holland, Neil Murray, Jason Gow, and Andrew Clarke. Modelling charge transfer in a radiation damaged charge coupled device for euclid. 2012.

[54] David Hall, Nathan Bush, Daniel Wood, Neil J Murray, Jason Gow, Jesper Skottfelt, and Andrew Holland. Mapping radiation-induced defects in ccds through space and time. In *SPIE Astronomical Telescopes+ Instrumentation*, pages 99150I–99150I. International Society for Optics and Photonics, 2016.

[55] Daniel Wood, David J Hall, Jason Gow, Jesper Skottfelt, Neil J Murray, Konstantin Stefanov, and Andrew D Holland. Evolution and impact of defects in a p-channel ccd after cryogenic proton-irradiation. *IEEE Transactions on Nuclear Science*, 2017.

[56] Neil J Murray, David J Burt, David Hall, and Andrew D Holland. The relationship between pumped traps and signal loss in buried channel ccds. SPIE, 2013.

[57] Jesper Skottfelt, David Hall, Jason Gow, Neil Murray, Andrew Holland, and Thibaut Prod'homme. Comparing simulations and test data of a radiation damaged ccd for the euclid mission. In *SPIE Astronomical Telescopes+ Instrumentation*, pages 991529–991529. International Society for Optics and Photonics, 2016.

[58] A Clarke, D Hall, N Murray, J Gow, A Holland, and D Burt. Pixel-level modelling and verification for the euclid vis ccd. SPIE, 2013.

[59] Sami-Matias Niemi, Mark Cropper, Magdalena Szafraniec, and Thomas Kitching. Measuring a charge-coupled device point spread function. *Experimental Astronomy*, 39(2):207–231, 2015.